Fundamentals, advances and perspectives of piezocatalysis: A marriage of solid-state physics and catalytic chemistry

Nan Meng [a], Wei Liu [a], Ruyu Jiang [a], Yu Zhang [a], Steve Dunn [b], Jiyue Wu [c,*], Haixue Yan [d,*]

[a] *State Key Laboratory for Modification of Chemical Fibers and Polymer Materials, College of Materials Science and Engineering, Donghua University, Shanghai 201620, China*
[b] *School of Engineering, London South Bank University, London SE1 0AA, UK*
[c] *Key Laboratory of Inorganic Functional Materials and Devices, Shanghai Institute of Ceramics, Chinese Academy of Sciences, Shanghai 200050, China*
[d] *School of Engineering & Materials Science, Queen Mary University of London, London E1 4NS, UK*

ARTICLE INFO

ABSTRACT

Piezocatalysis, an evolving catalytic technology built on the piezoelectric properties of catalysts, breaks down the barrier between mechanical energy and chemical energy. The potential difference that arises from the mechanical deformation of a piezoelectric material is commonly termed 'piezopotential'. Piezopotential has been demonstrated to facilitate the manipulation of band structure and/or charge carrier separation. Despite significant efforts to design materials and understand the mechanism of piezoelectrically enhanced chemistry through semiconductor physics, there remains an opportunity to review the relationships between catalytic performance and piezo/ferroelectric properties. Herein, we provide a comprehensive summary of the catalytic mechanisms and correlated piezo/ferroelectric physical mechanism in the field of piezocatalysis. A fundamental understanding of piezo/ferroelectric structural design based on solid-state physics can be used to shed light on the future development of piezocatalysis. In addition, the types of piezoelectric materials, the design strategies for catalysis efficiency enhancement, and the up-to-date applications in environment remediation, renewable energy conversion, biomedicine and biotechnology are discussed. Finally, future perspectives for designing and developing highly active piezocatalysts using the guidelines of physicochemical relationships are proposed.

1. Introduction

The development of modern society is producing increasingly serious issues of environmental pollution and energy resource management. The need to make use of renewable energy resources without sacrificing environment is important to scientists in the fields covering chemistry, environmental and materials science. Mechanical energy, the energy of motion, is one of the most versatile forms of renewable energy, which can be derived from wind, ocean streams and heat flow causing gases to rise and fall. With the proposal of piezotronic effect and the development of nanogenerators, the collection and conversion of mechanical energy has gained increasing attention in the field of energy harvesting, as well as process chemistry.[1] Based on the integration of piezoelectric effect

and electrochemical effect, piezocatalysis is a brand-new way to utilize piezo-induced charges in assisting typical chemical processes by harvesting various forms of mechanical energy.

The piezocatalytic effect uses electric charges generated by piezoelectric effect in chemical reactions. As a result of the non-centrosymmetric crystal structure of piezoelectric materials, the centers of positive and negative charges in the unit cell do not coincide under external mechanical force or strain, with the formation of a net dipole moment. Following the ordered alignment of dipole moments, a macroscopic built-in electric field, historically known as the depolarization field, will be established. Free charge carriers within the material and charged species outside the material immigrate to the surfaces of different polarities to screen the depolarization field. The movement of screening species that during a chemical reaction have been termed the piezopotential. To sum up, the piezopotential acts as a driving force in regulating the separation and transportation of charge carriers.

In recent years, the application areas of piezocatalysis have expanded from the degradation of organic dyes and H_2 evolution, to the elimination of greenhouse gases and the inhibition of tumor cells. The fields of interest now cover environmental remediation [2], exploitation of renewable energy resources [3,4] and biotechnologies [5,6]. The performance of piezocatalysis is predominantly governed by the piezoelectric properties of materials and the interface between catalysts and reactive species. Materials with finely tuned composition and morphology have been designed for piezocatalysis. For example, $R3c$ ferroelectric $LiNbO_3$-type $ZnSnO_3$ nanowires exhibited a pronounced performance of piezocatalytic water splitting with a hydrogen production rate of 3453.1 μmol g^{-1} h^{-1}, superior to most photocatalysts. [7] Single- and few-layered MoS_2 nanoflowers showed ultra-fast degradation of Rhodamine B (RhB) with a degradation rate of 40336 ppm L/mol s^{-1}.[8] A higher degradation rate (69889 ppm L/mol s^{-1}) was observed in $MoSe_2$ nanoflowers by the same research group.[9] Other materials have also been designed to realize piezocatalytic applications such as $Bi_4O_5X_2$ (X = Br, I) nanosheets [10], Sr, Zr-doped $BaTiO_3$ nanoparticles [11,12], $Bi_2VO_{5.5}$ plates [13], $LiNbO_3$ nanoparticles [14], hydrogen-bonded $SnO(OH)_2$ particles [15], $Sr_{1-x}Fe_xTiO_3$ [16], glass/ceramics composites [17–19], $rGO/BiVO_4$ composites [20], piezoelectric polymer-based composites [21–23], piezoelectric textiles coated with MoS_2 [24], etc. Researchers have been endeavouring to acquire a comprehensive understanding of the dominant factors that influence piezocatalytic reactions, with the ultimate aim of addressing current socio-economic challenges such as the ageing population and climate change.

Piezoelectricity coupling with photocatalytic semiconductors (termed as piezo-photocatalysis) has been extensively studied to tune and/or enhance their optoelectronic activities. The coupling effect among piezoelectric properties, semiconductor physics and photocatalysis process has been subcategorized from piezotronics, termed piezo-phototronics. In piezo-phototronics, the piezoelectric polarization charges and the induced piezopotential enable the migration of photoinduced charges (i.e., electrons and holes) towards
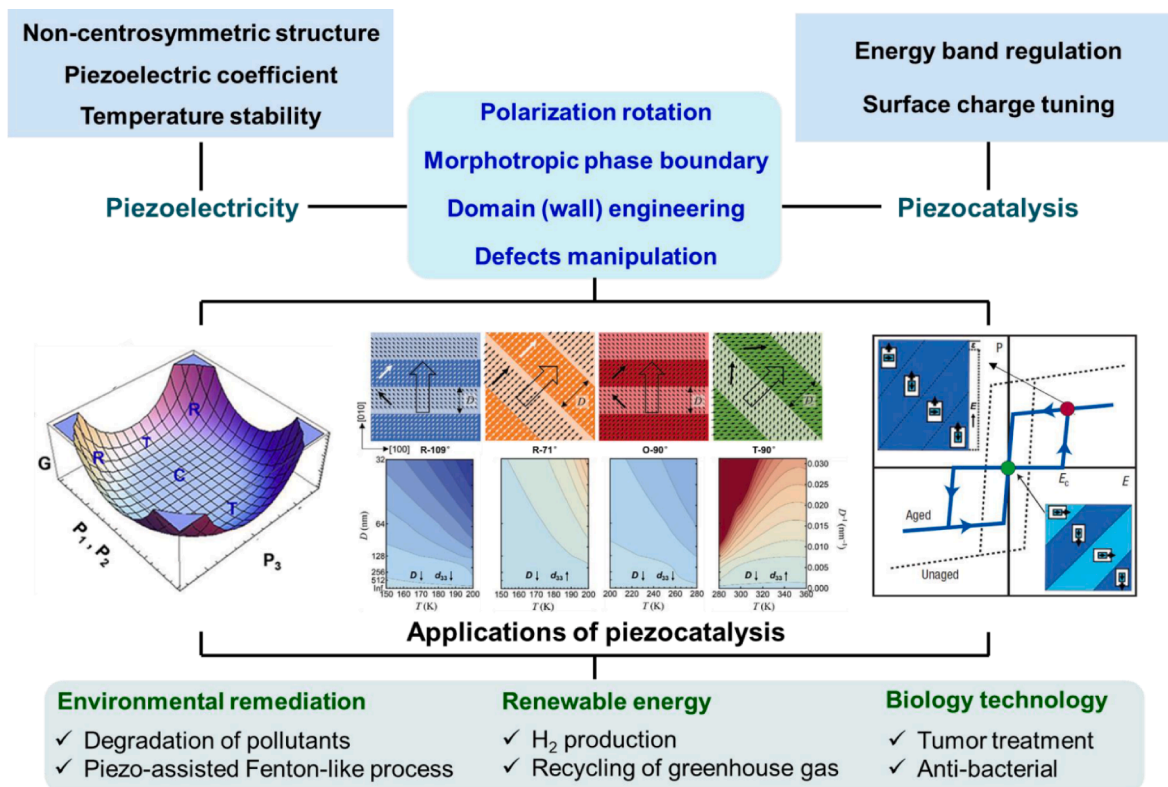

Fig. 1. Schematic illustration of the key features of piezoelectricity, the mechanism and enhancing strategies of piezocatalysis from the perspective of piezoelectric physics, and the applications of piezocatalysis. Reproduced from [46–48], with the permission from Elsevier, Wiley and Springer Nature.

specific directions, promoting their separation and diminishing their recombination. In view of the semiconductor and piezoelectric physics, researchers have developed diverse piezo-photocatalytic configurations such as metal/semiconductor contacts (i.e., Pt/ZnO contact [25], Au/BaTiO$_3$ nanoparticles [26], *etc.*) and heterojunctions (i.e., ZnO-WO$_{3-x}$ nanorod arrays [27], NaNbO$_3$/ITO [28], BiFeO$_3$/TiO$_2$ core–shell nanocomposites [29,30]). These advances provide a fundamental guideline for regulating the coupling effect between piezopotential and semiconductor characteristics. This aims to relate electronic states and the abundance of free charges to induce the rearrangement of energy band structures under the impact of piezopotential. Piezo-photocatalysis has been well documented [31–38]. We will focus on piezocatalysis in this review to understand the role of solid-state physics in piezocatalysis.

A number of high-quality reviews have introduced different aspects of piezocatalysis. With respect to mechanism elucidation, Liu *et al.* comprehensively summarized two theories for illustrating piezocatalysis, the theory of energy band and effect of screening charge. [39] Tudela *et al.* summarized the key fundamentals from the perspective of piezoelectricity, electrochemistry and sono-chemistry. [40] Qian *et al.* mainly discussed the coupling piezo-electro-chemical mechanism of piezoelectric materials. [41] Ma *et al.* highlighted the reinforcing role of polarization including macroscopic, piezoelectric and ferroelectric polarization as well as the surface polarization in photocatalysis. From the perspective of applications, Yang *et al.* provided an overview of piezocatalytic environmental remediation. [2] Ali *et al.* focused on the piezocatalytic inhibition of water bacteria and degradation of organic pollutants. [42] Huang *et al.* summarized the piezoelectricity enhanced photocatalytic environmental applications. [43] Bandara *et al.* introduced the piezocatalytic/piezo-photocatalytic removal of pollutants. [44] Rtimi *et al.* reviewed the heterogenous advanced oxidation processes using stoichiometric ABO$_3$ nano-structured perovskites. [45] In addition, Shi *et al.* summarized the advances of piezocatalytic medicine used in tissue repair and regeneration, tumor treatment, biosensing *etc.* [5] Despite this progress, a comprehensive understanding of the role classic piezo/ferroelectric physics plays in influencing piezocatalytic performance is missing. Therefore, it is believed that a deep investigation into the relationship between piezocatalytic mechanisms and correlated piezo/ferroelectric physics in the field of piezocatalysis is of great value at this time point and may enlighten the future development of this field.

The structure of this review is shown in Fig. 1. To begin, the fundamentals of the piezoelectric effect and the key features of mainstream piezoelectric materials are described. This is followed by the interpretation of the proposed mechanisms of piezocatalysis from the perspective of energy band theory and screening charge effect. Then, an in-depth overview of essential aspects of physical mechanism behind the optimization of piezoelectric properties is provided. This involves the rotation of polarization, the construction of morphotropic phase boundary, the engineering of domain or domain walls and the manipulation of defects. These physical interactions play a crucial role in regulating the reaction process of piezocatalysis. After that, a summary of the enhancing strategies and applications of piezocatalysis is presented. Finally, the challenges and perspectives in boosting piezocatalytic performance out of physicochemical relationship are outlooked, which aims to inspire researchers to develop novel and efficient piezocatalysts.

2. Piezoelectric materials

2.1. Basics of piezoelectric effect

Piezoelectric materials convert mechanical to electrical or electrical to mechanical energy, as described in Equation 1–2. Equation (1) and Equation (2) describe the direct and converse piezoelectric effect, respectively.

$$D_k = d_{kij}T_{ij} \tag{1}$$

$$S_{ij} = d^*_{kij}E_k \tag{2}$$

The electric displacement (D, C m^{-2}) induced *via* the direct piezoelectric effect shows a linear relation with the applied mechanical stress (T, N m^{-2}). Analogously, the strain (S) induced *via* the converse piezoelectric effect is linearly dependent of applied electric field (E, V m^{-1}). The proportional constants d_{ijk} (unit: pC N^{-1}) and d^*_{kij} (unit: pm V^{-1}) are piezoelectric charge and strain coefficients, respectively, where the Einstein notation represents the axial direction. All piezoelectric materials show the anisotropy of piezoelectric coefficients. Stress and strain tensor are principally rank-2 tensor, but they are all symmetry tensors, and can be re-identified as $T_{11} = T_1$, $T_{22} = T_2$, $T_{33} = T_3$, $T_{23} = T_4$, $T_{13} = T_5$, $T_{12} = T_6$. Therefore, the piezoelectric coefficients d_{ijk} and d^*_{kij} can be relabeled as d_{km} based on the reduced Voigt matrix (Equation 3), where the subscript k refers to the constituent of electric displacement D or field E (E_1, E_2, E_3), and the subscript m demonstrates the mechanical strain or stress, m = 1, 2, 3, 5 and 6, as defined above. It is generally recognized that $d_{km} = d^*_{km}$, specifically, the coefficients associating the electric field with strain are equivalent to those linking the stress to the electric polarization from the thermodynamic perspective.

$$\begin{pmatrix} d_{11} & d_{12} & d_{13} & d_{14} & d_{15} & d_{16} \\ d_{21} & d_{22} & d_{23} & d_{24} & d_{25} & d_{26} \\ d_{31} & d_{32} & d_{33} & d_{34} & d_{35} & d_{36} \end{pmatrix} = \begin{pmatrix} d_{111} & d_{122} & d_{132} & d_{123} & d_{113} & d_{112} \\ d_{211} & d_{222} & d_{233} & d_{223} & d_{213} & d_{212} \\ d_{311} & d_{322} & d_{333} & d_{323} & d_{313} & d_{312} \end{pmatrix} \tag{3}$$

Piezoelectric coupled equations in the form of strain-charge built on the basics of $\{S\} = [s^E]\{T\} + [d^t]\{E\}$ and $\{D\} = [d]\{T\} + [\varepsilon^T]\{E\}$ are listed in Equation 4–5, where s^E and ε^T are elastic compliance and dielectric permittivity, respectively. Specifically, for poled piezoelectric ceramic materials with 4 *mm* crystal class (e.g., lead zirconate titanate PZT, barium titanate BaTiO$_3$), the piezoelectric strain-charge equations can be simplified as Equation 6–7.

$$
\begin{bmatrix} S_1 \\ S_2 \\ S_3 \\ S_4 \\ S_5 \\ S_6 \end{bmatrix} = \begin{bmatrix} s_{11}^E & s_{12}^E & s_{13}^E & s_{14}^E & s_{15}^E & s_{16}^E \\ s_{12}^E & s_{22}^E & s_{23}^E & s_{24}^E & s_{25}^E & s_{26}^E \\ s_{13}^E & s_{23}^E & s_{33}^E & s_{34}^E & s_{35}^E & s_{36}^E \\ s_{14}^E & s_{24}^E & s_{34}^E & s_{44}^E & s_{45}^E & s_{46}^E \\ s_{15}^E & s_{25}^E & s_{35}^E & s_{45}^E & s_{55}^E & s_{56}^E \\ s_{16}^E & s_{26}^E & s_{36}^E & s_{46}^E & s_{56}^E & s_{66}^E \end{bmatrix} \bullet \begin{bmatrix} T_1 \\ T_2 \\ T_3 \\ T_4 \\ T_5 \\ T_6 \end{bmatrix} + \begin{bmatrix} d_{11} & d_{21} & d_{31} \\ d_{12} & d_{22} & d_{32} \\ d_{13} & d_{23} & d_{33} \\ d_{14} & d_{24} & d_{34} \\ d_{15} & d_{25} & d_{35} \\ d_{16} & d_{26} & d_{36} \end{bmatrix} \bullet \begin{bmatrix} E_1 \\ E_2 \\ E_3 \end{bmatrix} \tag{4}
$$

$$
\begin{bmatrix} D_1 \\ D_2 \\ D_3 \end{bmatrix} = \begin{bmatrix} d_{11} & d_{12} & d_{13} & d_{14} & d_{15} & d_{16} \\ d_{21} & d_{22} & d_{23} & d_{24} & d_{25} & d_{26} \\ d_{31} & d_{32} & d_{33} & d_{34} & d_{35} & d_{36} \end{bmatrix} \bullet \begin{bmatrix} T_1 \\ T_2 \\ T_3 \\ T_4 \\ T_5 \\ T_6 \end{bmatrix} + \begin{bmatrix} \varepsilon_{11}^X & \varepsilon_{12}^X & \varepsilon_{13}^X \\ \varepsilon_{12}^X & \varepsilon_{22}^X & \varepsilon_{23}^X \\ \varepsilon_{13}^X & \varepsilon_{23}^X & \varepsilon_{33}^X \end{bmatrix} \bullet \begin{bmatrix} E_1 \\ E_2 \\ E_3 \end{bmatrix} \tag{5}
$$

$$
\begin{bmatrix} S_1 \\ S_2 \\ S_3 \\ S_4 \\ S_5 \\ S_6 \end{bmatrix} = \begin{bmatrix} s_{11}^E & s_{12}^E & s_{13}^E & & & \\ s_{12}^E & s_{11}^E & s_{13}^E & & 0 & \\ s_{13}^E & s_{13}^E & s_{33}^E & & & \\ & & & s_{44}^E & 0 & 0 \\ & 0 & & 0 & s_{44}^E & 0 \\ & & & 0 & 0 & 2 \bullet (s_{11}^E - s_{12}^E) \end{bmatrix} \bullet \begin{bmatrix} T_1 \\ T_2 \\ T_3 \\ T_4 \\ T_5 \\ T_6 \end{bmatrix} + \begin{bmatrix} 0 & 0 & d_{31} \\ 0 & 0 & d_{31} \\ 0 & 0 & d_{33} \\ 0 & d_{15} & 0 \\ d_{15} & 0 & 0 \\ 0 & 0 & 0 \end{bmatrix} \bullet \begin{bmatrix} E_1 \\ E_2 \\ E_3 \end{bmatrix} \tag{6}
$$

$$
\begin{bmatrix} D_1 \\ D_2 \\ D_3 \end{bmatrix} = \begin{bmatrix} 0 & 0 & 0 & 0 & d_{15} & 0 \\ 0 & 0 & 0 & d_{15} & 0 & 0 \\ d_{31} & d_{31} & d_{33} & 0 & 0 & 0 \end{bmatrix} \bullet \begin{bmatrix} T_1 \\ T_2 \\ T_3 \\ T_4 \\ T_5 \\ T_6 \end{bmatrix} + \begin{bmatrix} \varepsilon_{11}^X & 0 & 0 \\ 0 & \varepsilon_{11}^X & 0 \\ 0 & 0 & \varepsilon_{33}^X \end{bmatrix} \bullet \begin{bmatrix} E_1 \\ E_2 \\ E_3 \end{bmatrix} \tag{7}
$$

Apart from the piezoelectric charge and strain coefficients, practical applications require other forms of piezoelectric coefficients. Table 1 lists four forms of piezoelectric coefficients 'piezoelectric charge (strain) coefficient (d)', 'piezoelectric voltage coefficient (g)', 'piezoelectric stress coefficient (e)' and 'piezoelectric stiffness coefficient (h)', which corresponds to different specific conditions of 'short circuit and mechanically free', 'open circuit and mechanically free', 'mechanically clamped and short circuit' and 'open circuit and mechanically clamped', respectively. The first and second set of the equations of four forms of piezoelectric coefficients represent the direct and converse piezoelectric effect, respectively.

The capability of materials' function *via* piezoelectricity can be evaluated by the piezoelectric coupling coefficient (k), also known as electromechanical coupling factor (Equation (8)), which defines as the non-dimensional ratio between the converted ($U_{\text{converted}}$) and input energy (U_{input}).

$$
k = \sqrt{\frac{U_{\text{converted}}}{U_{\text{input}}}} \tag{8}
$$

Table 1
Description and definition of piezoelectric coefficients.

Abbreviation	Definition	Equation
d	Piezoelectric charge (strain) coefficient	$d_{ij} = (\frac{\partial D_i}{\partial T_j})_E = (\frac{\partial S_j}{\partial E_i})_T$
g	Piezoelectric voltage coefficient	$g_{ij} = -(\frac{\partial E_i}{\partial T_j})_D = (\frac{\partial S_j}{\partial D_i})_T$
e	Piezoelectric stress coefficient	$e_{ij} = (\frac{\partial D_i}{\partial S_j})_E = -(\frac{\partial T_j}{\partial E_i})_S$
h	Piezoelectric stiffness coefficient	$h_{ij} = -(\frac{\partial E_i}{\partial S_j})_D = -(\frac{\partial T_j}{\partial D_i})_S$

For specific geometry, *k* can be determined using the piezoelectric charge coefficient, dielectric permittivity and elastic compliance. Equation (9) (using k_{31} as an example) has been widely utilized to predict the potential functionality of one specific piezoelectric material.

$$k_{31} = \frac{d_{31}}{\sqrt{s_{11}^E \varepsilon_{33}^X}} \tag{9}$$

where ε_{33}^X represents the permittivity of the material, which is defined as the relative permittivity of the material multiplied by vacuum permittivity.

2.2. Piezoelectric materials

Single crystals, ceramics and poly(vinylidene fluoride)-based polymers are three mainly investigated piezoelectric materials. Fig. 2 presents the evolution of piezoelectric materials.

Piezoelectric effect was firstly observed in α-Quartz [54] (d_{33}: 2 pC N^{-1}) in 1882. Despite the successful synthesis as early as 1655, Rochelle salt ($NaKC_4H_4O_6 \cdot 4H_2O$) was demonstrated to exhibit piezoelectricity in 1921.[55] Potassium dihydrogen phosphate (KH_2PO_4, KDP) and ammonium dihydrogen phosphate ((NH_4)H_2PO_4, ADP) crystals were latterly discovered piezoelectric materials with piezoelectric coefficient of about 20 and 50 pC N^{-1}, respectively.[56]

The important milestone, $BaTiO_3$, was achieved in 1946, which revolutionizes the field of piezoelectric materials, and still attracts continuous interest in terms of both scientific research and practical applications. $BaTiO_3$ has a perovskite structure (ABO_3) that is composed of corner-sharing BO_6 octahedra linked in a cubic or non-cubic (orthorhombic or tetragonal) with B sites of smaller cations positioning the center of BO_6 octahedra and A sites of large cations occupying the interstices between octahedra (inset in Fig. 2). $BaTiO_3$ exhibits piezoelectric properties (k_{33}: about 0.5; d_{33}: about 190 pC N^{-1}) which can be further enhanced *via* proper element doping such as Na or K. $BaTiO_3$ shows a relatively low Curie point (about 120 °C), limiting its applications at elevated temperatures. Pb or Ca doping have been reported to stabilize the tetragonal phase of $BaTiO_3$ over higher temperature, therefore broadening the working temperature of $BaTiO_3$-based ceramics.

$PbZr_{1-x}Ti_xO_3$ (PZT) was developed in the 1950s, with the main research interest in engineering compositions close to the morphotropic phase boundary (MPB). MPB separates two polar phases with different crystal symmetries, and PZT with compositions close to MPB show enhanced piezoelectric properties (d_{33}: 300–1000 pC N^{-1}) due to the enhanced polarizability arising from the ease of rotation between different symmetries. PZT shows a high Curie point (about 400 °C) and is widely used in actuators and transducers especially for high temperature applications. The piezoelectricity of PZT can be classified into 'hard' and 'soft' characteristics *via* appropriate doping.[57] 'Hard' and 'soft' describe the mobility of domains, domain walls or dipoles, as well as the behavior of polarization and depolarization. Hard PZT ceramics are doped with acceptor ions (e.g., site A: K^+ or Na^+; site B: Fe^{3+}, Al^{3+} or Mn^{3+}) to build oxygen vacancies to hinder the motion of domain walls. As a result, hard PZT materials exhibit low dielectric loss and strong stability when subjected to electric field or mechanical stress, which makes them suitable in applications of high-power devices such as sonar technologies, ultrasonic processors and ultrasonic transducer. Soft PZT ceramics are doped with donor ions (e.g., site A: La^{3+} or W^{6+}; site B: Nb^{5+} or Sb^{5+}) to create the vacancies of A sites with improved mobility of domain walls. Soft PZT materials are easy to be poled and show a high piezoelectric charge coefficient and electromechanical coupling factor, which makes them attractive in applications such as loudspeakers, microphones and sound transducers. There is a strand of research focusing on developing materials
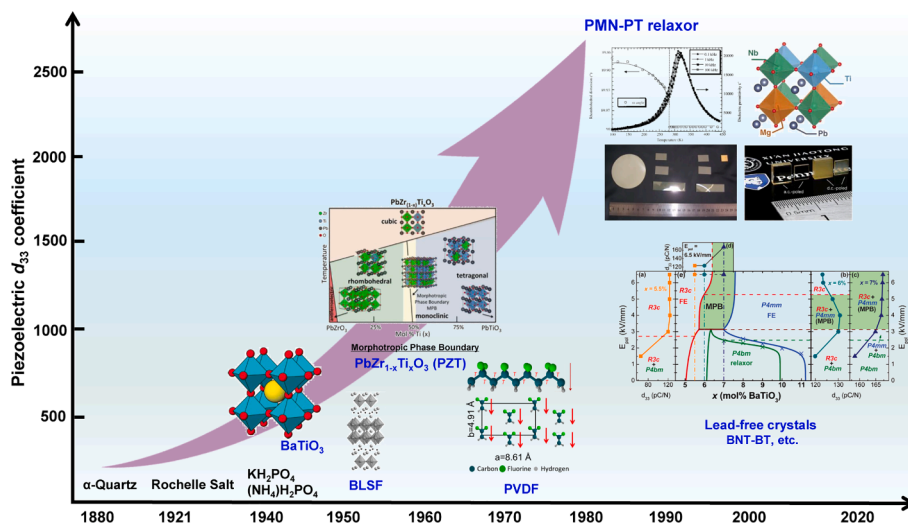

Fig. 2. The evolution of piezoelectric materials (reproduced from [45,49–53], with the permission of Elsevier, Wiley, Nature Portfolio, Multidisciplinary Digital Publishing Institute, American Chemical Society, American Physical Society, and Innovia Materials (Shanghai) Co., Ltd).

with combined merits of soft and hard PZT ceramics. [58,59]

Bismuth layered-structure ferroelectrics (BLSF) have been developed for high temperature applications owing to their high Curie point and large anisotropy in piezoelectric coupling coefficient. Lead-free perovskite materials such as $K_{0.5}Na_{0.5}NbO_3$ (KNN), $Bi_{0.5}Na_{0.5}TiO_3$ (BNT) and $BiFeO_3$ (BFO), have experienced significant progress in the last 20 years. BNT is one of the most important lead-free piezoelectric ceramics. [60,61] Pure BNT shows a depolarization temperature (T_d: about 190 °C), moderate piezoelectric coefficients (d_{33}: about 55–65 pC N^{-1}) and large ferroelectric remnant polarization (about 30 μC cm^{-2}). However, BNT requires high processing temperatures, and is difficult to be poled due to the high electric conductivity.[62] MPB engineering and other materials' doping have been utilized to manipulate the piezoelectric properties and Curie point of BNT-based ceramics. For example, BNT doped with $BaTiO_3$ and KNN (91BNT-6BT-3KNN) in the MPB region of rhombohedral/tetragonal phase exhibited a d_{33} of 181 pC N^{-1}.[63]

Compared to ceramic materials, single crystals in the absence of grain boundary can exhibit more pronounced piezoelectric properties. Relaxor-based ferroelectric single crystals with polar nano regions (PNRs) and a partially disordered structure, are important piezoelectric single crystal materials. Lead magnesium niobate (PMN), firstly developed in 1961, is one typical relaxor-based ferroelectric material. PMN shows a high dielectric constant and diffuse phase transition with a broad peak of maximum dielectric constant at Curie point. Similar to PZT-based system, MPB can also be engineered in relaxor-based ferroelectrics to enhance piezoelectricity. Combined MPB engineering and the exceptional performance of single crystals, relaxor-PT-based crystals such as $Pb(Mg_{1/3}Nb_{2/3})O_3–PbTiO_3$ (PMN–PT) and $Pb(Zn_{1/3}Nb_{2/3})O_3$–PT (PZN–PT), have reported a piezoelectric coefficient d_{33} of 1000–3000 pC N^{-1} [64,65], high electric field induced strain (about 1.7) and electromechanical coupling factor (k_{33}: > 0.9) [64]. Table 2 summarizes the key piezoelectric parameters of typical single crystal materials. The main research areas involve enhancing the piezoelectric coefficient, electromechanical coupling factor as well as increasing Curie transition (T_c) temperature to fulfill high-temperature applications.

Apart from classic perovskite- and bismuth layer-structured piezoelectric material, a limited number of 2D materials with layered structure have been reported to exhibit piezoelectricity. As such they are emerged as promising candidates in piezocatalysis.[71] The 2D piezoelectric materials can be categorized into homoatomic systems, e.g., graphene, phosphorene, and heteroatomic systems, e.g., hexagonal boron nitride (h-BN) and transition-metal dichalcogenides (TMDCs).[72] Due to the restrained in-plane polarization, these 2D-layered materials share the common characteristics of a small d_{33} (out-of-plane piezoelectricity) and a modest d_{31} (in-plane to out-of-plane). Recently, it has been found that both out-of-plane and in-plane piezoelectricity can be enhanced based on the construction of Janus 2D structures, e.g., MM'XX' (M, M' = Ga, In; X, X' = S, Se, Te).[73] Compared with bulk materials, most atoms belong to the surface for 2D materials, revealing the non-negligible impact of surface modifications on the physical properties, including piezo-electricity. Furthermore, the finite number of atoms in 2D-layered materials is conducive to theoretical simulations, which is critical for the predication of piezoelectricity of designated 2D materials.[74]

In addition to the progress achieved in inorganic oxides, polymer-based piezoelectric materials have also experienced significant advances since the pioneering work of demonstrating the piezoelectricity and ferroelectricity of poly(vinylidene fluoride) (PVDF) in 1969 and 1978, respectively. [75,76] The intrinsic flexibility and low density make piezoelectric polymers highly useful for applications in flexible electronic devices including sensors, biomedical and energy harvesting devices. Moreover, piezoelectric polymers display much higher piezoelectric voltage constant (e.g., g_{33} of PVDF: 286.7 $\times 10^{-3}$ Vm N^{-1}), which renders them suitable for sensing applications. [77] However, compared to inorganic oxides, piezoelectric polymers usually exhibit inferior piezoelectricity (d_{33}: usually below 30 pC N^{-1}) arising from their low degree of crystallization and low polarization.

From the perspective of crystallization, piezoelectric polymers can be simply divided into semicrystalline and non-crystalline polymers. Semicrystalline piezoelectric polymers include PVDF families, polyurea, odd-numbered nylons and biopolymers (collagen, polypeptides, polyglycolide, polylactide and so on). The most characteristic semi-crystalline piezoelectric polymers are undoubtedly PVDF-based families including PVDF, its copolymers with trifluoroethylene (P(VDF-TrFE)) or hexafluoropropylene (P(VDF-HFP)), PVDF-TrFE-based terpolymers with chlorofluoroethylene (P(VDF-TrFE-CFE)) or chlorotrifluoroethylene (P(VDF-TrFE-CTFE)), and PVDF-TrFE-CFE-based tetrapolymer with fluorinated alkyne (P(VDF-TrFE-CFE-FA)) (Fig. 3a). PVDF homopolymer has four main phases, α-, β-, γ- and δ-phase, which arises from different chain conformation of *trans*-gauche (TGTG'), all-trans (TTT) with parallel adjacent chain packing, a mixture of *trans*-gauche and all-trans (TTTGTTTG') and TTT with anti-parallel adjacent chain packing. Fig. 3b shows the crystal structure and dipole moment of different phases of PVDF. The crystallization of PVDF is strongly

Table 2
Key piezoelectric parameters of mainly used single crystals.

Materials	Compositions	Piezoelectric charge coefficient d_{33} (pC N^{-1})	Electromechanical coupling factor k_{33}	Dielectric constant ε_r	Curie transition temperature (°C)	Ref
α-Quartz	SiO_2	2	–	4.5	–	[54]
LN	$LiNbO_3$	49	0.47	39	1140	[66]
Rochelle salt	$NaKC_4H_4O_6$-$4H_2O$	100	–	30	20	[55]
PMN-PT	$Pb(Mg_{1/3}Nb_{2/3})O_3$-$PbTiO_3$	1780	0.94	6000	143	[67,68]
PMN-PZT	$Pb(Mg_{1/3}Nb_{2/3})O_3$-$PbZrO_3$-$PbTiO_3$	1530	0.93	5000	216	[69]
PZN-PT	$Pb(Zn_{1/3}Nb_{2/3})O_3$-$PbTiO_3$	2500	0.94	5000	170	[64,65]
PIN-PMN-PT	$Pb(In_{0.5}Nb_{0.5})O_3$-$Pb(Mg_{1/3}Nb_{2/3})O_3$-$PbTiO_3$	1000–3000	0.90	3000–5000	160–170	[70]

dependent on the processing condition (Fig. 3c). Cooled from melt or less polar solvent leads to the formation of α-phase which is non-polar and most thermodynamically favorable. β-phase with TTT chain conformation shows the highest polarity arising from a high dipole moment of 7.0×10^{-30} C • m (~2.1 Debye), and usually transformed from the as-crystallized α-phase *via* post treatment such as solid-state drawing at 50–100 °C with a draw ratio of 3–5 and poling at high electric field (~ 500 kV mm^{-1}). Poling at low electric field (~ 150 kV mm^{-1}) transforms α-phase to its polar version, δ-phase, which also shows chain conformation of *trans*-gauche but with parallel adjacent chain packing leading to a existence of dipole moment.[78] Another method, pressing-folding (P&F), has been reported to achieve almost pure β-phase (Fig. 3d). [53,79] Specifically, an original film was initially folded before pressed and annealed at high pressure (120 MPa) and temperatures around the melting point of PVDF (160–170 °C). The non-polar α-PVDF almost fully transformed to β-PVDF after only seven P&F cycles, which is highly effective compared to conventional solid-state drawing. β-PVDF shows an average $|d_{33}|$ of 20–30 pC N^{-1},[80] and the highest value (−62 pC N^{-1}) was reported in a fully polarized (650 kV mm^{-1} for 40 cycles) biaxially-oriented PVDF film.[81]
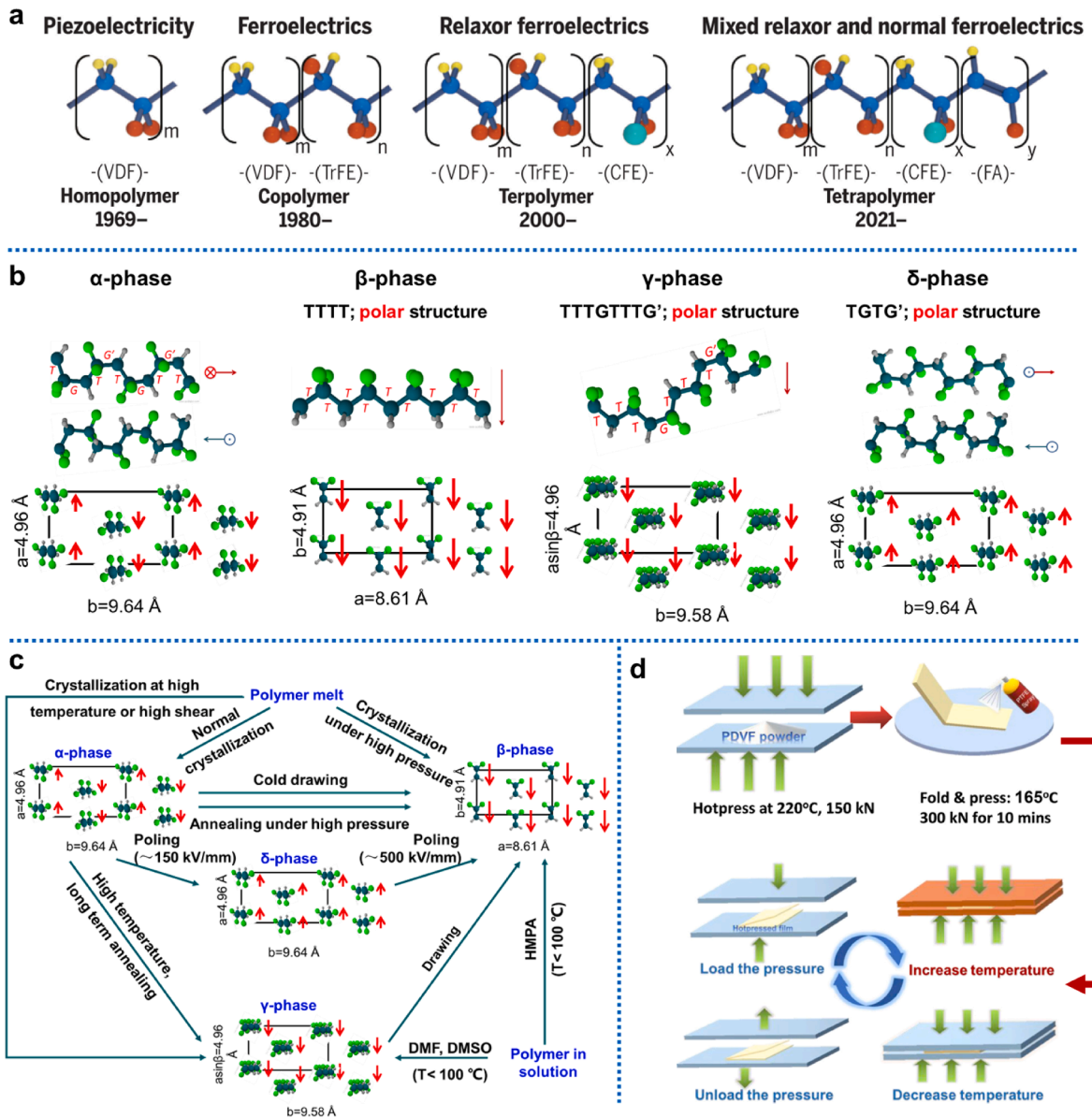

Fig. 3. (a) Polymer chains of PVDF homopolymer, P(VDF-TrFE) copolymer, P(VDF-TrFE-CFE) terpolymer and P(VDF-TrFE-CFE-FA) tetrapolymer (reproduced from [82], with the permission of American Association for the Advancement of Science). (b) The chain conformation and crystallographic structure of PVDF with different phases (reproduced from [53], with the permission of Nature Portfolio). (c) The processing routes and phase transitions of PVDF (reproduced from [75,83], with the permission of American Association for the Advancement of Science and Nature Portfolio). (d) The schematic description of pressing-folding (P&F) process (reproduced from [79], with the permission of Elsevier).

To perfectly tackle the indirect β-crystallization of PVDF homopolymer, P(VDF-TrFE) were designed and synthesized. Fig. 4a shows the phase diagram of P(VDF-TrFE),[84] where the incorporation of TrFE monomers (TrFE: < 40 mol%; VDF: > 60 mol%) restricts the formation of gauche bond and stabilizes the all-trans chain conformation regardless of processing conditions. P(VDF-TrFE) with VDF-rich compositions shows a higher degree of crystallinity and a slightly higher average value of $|d_{33}|$ (30–40 pC N^{-1}). [80,85] Liu *et al.* proposed the existence of similar MPB phenomena in P(VDF-TrFE) (Fig. 4b-i).[86] Compared to all-trans β-phase in VDF-rich copolymer, P(VDF-TrFE) with VDF content in the range of 49–55 mol% shows a mixture of all-trans and paraelectric-like disordered 3/1 helical phase with (TG)$_3$ conformation, which is mainly ascribed to the preferred isotactic instead of syndiotactic configuration of TrFE-TrFE segment. Correspondingly, P(VDF-TrFE) with VDF compositions of 49–55 mol% exhibit a high ε_r ($\sim$ 18 at 1 kHz), large d_{33} ($\sim$ −66 pC N^{-1}) and mixed behavior of normal ferroelectricity and relaxor-ferroelectricity compared to VDF-rich (normal ferroelectricity; ε_r: 10–12 at 1 kHz; d_{33}: $\sim$ −30 pC N^{-1}) and VDF-poor compositions (relaxor-ferroelectricity; ε_r: 14–16 at 1 kHz; d_{33}: $\sim$ −6 pC N^{-1}). This phenomenon is highly analogous to inorganic PMN-PT system. PMN-PT with PMN-rich compositions is rhombohedral with relaxor-ferroelectricity, whereas PT-rich compositions are tetragonal with normal ferroelectricity.[87]

P(VDF-HFP) is similar to PVDF in terms of structure and electromechanical properties, which also shows structural transformation from α- to β-phase under solid-state drawing or poling.[88] The introduction of large HFP monomer ($\sim$ 4–12 mol%) decreases the degree of crystallinity, which endows P(VDF-HFP) improved flexibility compared to PVDF. Moreover, P(VDF-HFP) exhibits remarkable processibility and is suitable to be processed using melt extrusion for large-scale commercial applications.[89]

As documented above, inorganic relaxor-ferroelectrics exhibit PNRs instead of large ferroelectric domains due to the nanoscale inhomogeneous polarization arising from chemical disorder. Analogously, adding another bulky monomer (about 9–10 mol%[90]) in PVDF-TrFE such as chlorofluoroethylene (CFE) or chlorotrifluoroethylene (CTFE) can induce relaxor behavior in terpolymers of P(VDF-TrFE-CFE) or P(VDF-TrFE-CTFE).[91] Fig. 5a and 5b show the ferroelectric polarization–electric field (*P-E*) hysteresis loops and current-electric field (*I-E*) loops of P(VDF-TrFE-CFE) 59/33/8, P(VDF-TrFE-CTFE) 64.2/27.1/8.7 and P(VDF-TrFE) 75/25.[92] P(VDF-TrFE) exhibits normal ferroelectricity with a high coercive field and large remnant polarization, whereas P(VDF-TrFE-CFE) shows complicated switching current loops arising from antiferroelectric like behavior (double hysteresis loop) and relaxor-ferroelectricity (coercive field close to zero). Terpolymers show much higher dielectric permittivity (ε_r: $\sim$ 50; loss tangent: $\sim$ 0.1 at 1 kHz) and lower remnant polarization ($\sim$ 0.01 C m^{-2}) compared to both PVDF and PVDF-TrFE (ε_r: $\sim$ 10–20; loss tangent: $\sim$ 0.02–0.05 at 1 kHz; remnant polarization: $\sim$ 0.06–0.10 C m^{-2}).[93] The relaxor behavior of terpolymers is interpreted as follows. Zhang *et al.* proposed that bulky monomers of CTFE and CFE can be seen as defects introduced in molecular structures, which breaks up the long-range order and is reminiscent of pinning effect observed in inorganic relaxors stabilizing *trans*-gauche conformation for non-polar phase (Fig. 5c). [91,94] Moreover, the energy barrier required for the transformation between non-polar and polar phases is diminished or even eliminated due to the pinning effect. The pinning effect in terpolymers such as P(VDF-TrFE-CFE) 59.2/33.6/7.2 is termed 'temporary physical pinning', which leads to complex switching current peaks and double hysteresis *P-E* loops (Fig. 5b). Dipoles switch at high electric field, and P(VDF-TrFE-CFE) exhibits reversible phase transition between paraelectric relaxor and polar phases upon
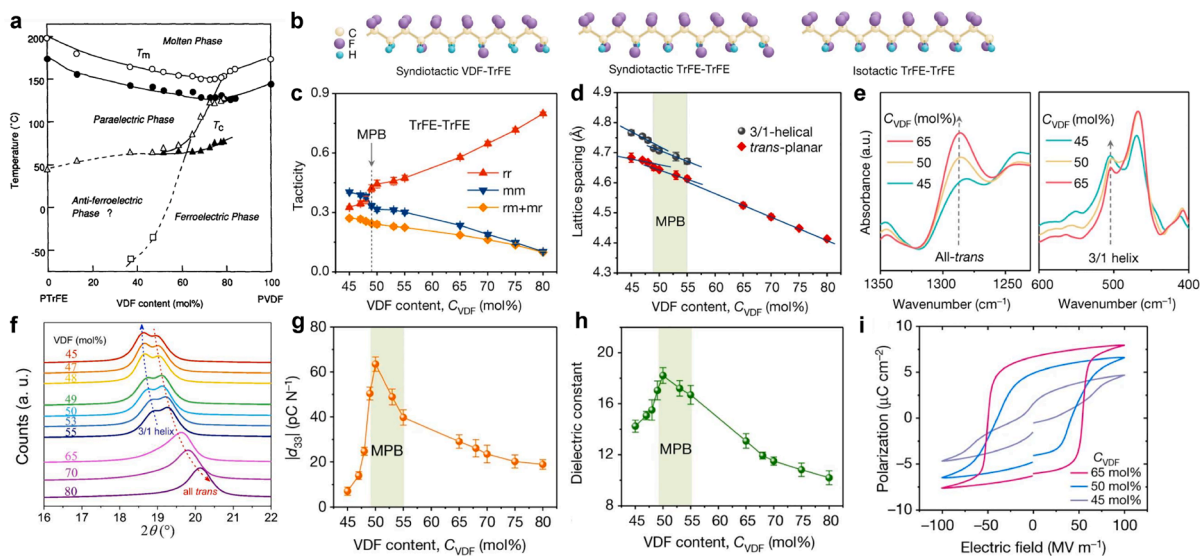

Fig. 4. (a) The phase diagram of P(VDF-TrFE) (reproduced from [84], with the permission of Elsevier). A similar behavior of MPB existed in P(VDF-TrFE) (reproduced from [86], with the permission of Springer Nature): (b) The chain tacticity in P(VDF-TrFE); (c) the tacticity of TrFE-TrFE as a function of VDF content, where rr, mm and rm + mr demonstrate syndiotactic, isotactic and heterotactic chain configurations, respectively; (d) the lattice spacing as a function of VDF content; (e) FTIR bands at 1290 cm^{-1} (all-trans conformation) and 507 cm^{-1} (3/1 helix conformation); (f) XRD patterns of P(VDF-TrFE) with different molar ratios; (g) the absolute values of d_{33} and (h) the dielectric constant (1 kHz, room temperature) as a function of VDF content; and (i) the ferroelectric hysteresis loops (triangular waveform, 1 Hz, room temperature) of P(VDF-TrFE) with molar contents of 65/35, 50/50 and 45/55, respectively.
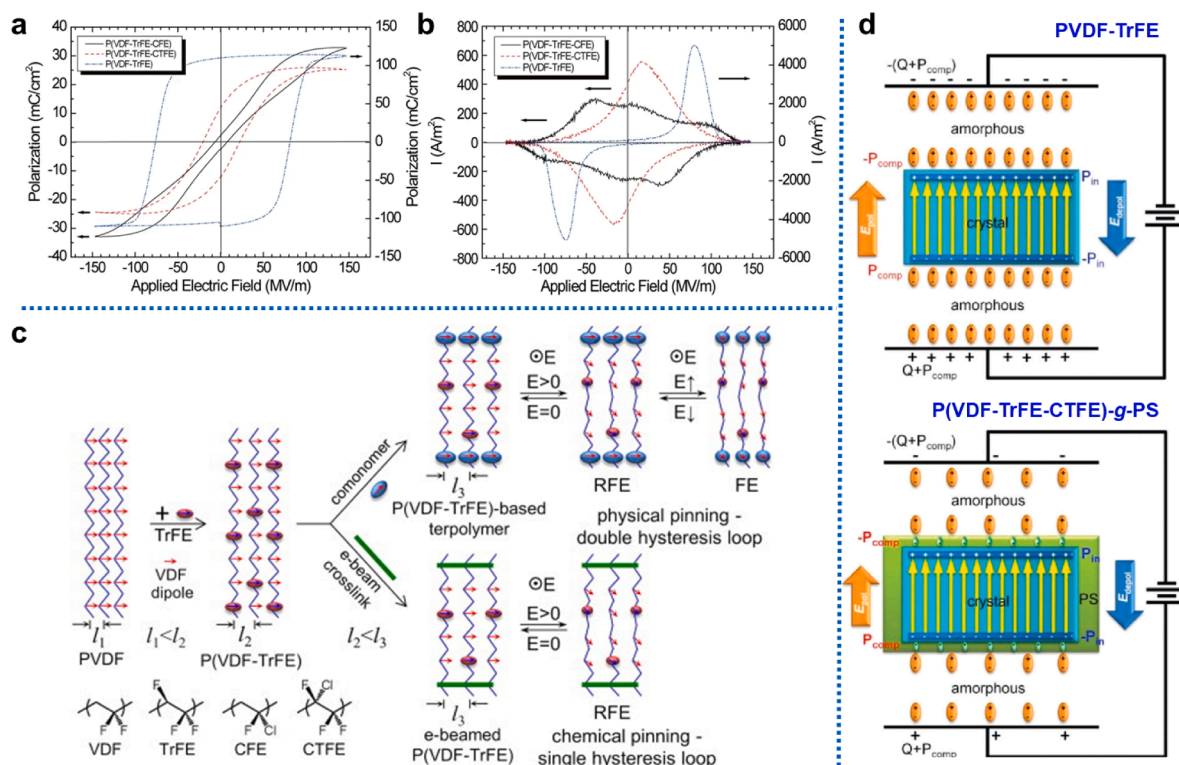
Fig. 5. (a) The ferroelectric *P-E* and (b) *I-E* loops of P(VDF-TrFE-CFE) 59/33/8, P(VDF-TrFE-CTFE) 64.2/27.1/8.7 and P(VDF-TrFE) 75/25 (reproduced from [92], with the permission of Nature Portfolio). (c) The schematic description of physical and chemical pinning in terpolymer P (VDF-TrFE-CFE) 59.2/33.6/7.2 and e-beam irradiated P(VDF-TrFE) 50/50, respectively, where *l*, red and blue ovals with arrows, and green bars represent the interchain distance, TrFE and CTFE monomers, and chemical cross-linking inside crystallites, respectively (reproduced from [94], with the permission of Elsevier). (d) The schematic diagram illustrating the interaction between crystalline and amorphous regions of P(VDF-TrFE) and P (VDF-TrFE-CTFE)-*g*-PS, where green rectangle represents the interfacial layer formed after PS grafting (reproduced from [95], with the permission of American Chemical Society). (For interpretation of the references to color in this figure legend, the reader is referred to the web version of this article.)

loading and unloading electric field. The pinning effect in *e*-beam irradiated P(VDF-TrFE) 50/50 is termed 'chemical pinning', which contributes to an expansion of interchain distance and permanently pins polymer chains due to internally crosslinked crystals. Zhu *et al.* determined that the nanoconfinement effect arising from the interaction between crystallites and amorphous region also contributes to relaxor behavior in terpolymers (Fig. 5d). [94,95] Wang *et al.* suggested that chain chirality owing to the local distortion of the torsional angles of gauche bonds generates conformation disorder, thereby relaxor behavior in polymers.[96]

An exciting breakthrough has been accomplished in tetrapolymer of PVDF-TrFE-CFE-FA (composition: 63/29.7/5.4/1.9), [93,97] which shows dramatically improved piezoelectric properties (k_{33}: 80%, d_{33}: −1050 pm V^{-1} at 40 kV mm^{-1}) that outperforms PZT ceramics. This exceptional electromechanical performance is attributed to the restricted energy barrier for the transformation between all-trans to 3/1 helical chain conformations due to the small size and less steric constraints of FA monomers (Fig. 6).

Other semicrystalline piezoelectric polymers include but not limited to odd-numbered nylons (polyamide), aliphatic and aromatic polyurea. Odd-numbered nylons are composed of even numbers of methylene groups (–CH$_2$-) connected by amide group (NH-CO) with a dipole moment of 3.7 Deybe, and are promising for high temperature applications (up to 200 °C). For example, nylon-11 shows a thermally stale d_{31} of 14 pC N^{-1}.[98] Polyurea is an important engineering thermoset elastomer due to excellent chemical, thermal and water resistance. Polyurea consists of urea linkages [-NH(C=O)NH], and is expected to show piezoelectricity and ferroelectricity due to the large dipole moment of urea bond (4.9 Deybe). Aliphatic polyurea-5 synthesized *via* vapor deposition polymerization exhibited a d_{31} and e_{31} of 4 pC N^{-1} and 10 mC m^{-2}, respectively.[99] Aromatic polyurea shows similar piezoelectric constant (*e*: 15 mC m^{-2}) with good thermal stability even up to 200 °C. [100]

Amorphous piezoelectric polymers have been less studied compared to semicrystalline ones due to their weak piezoelectric properties. The piezoelectricity of amorphous polymers is attributed to the partial retention of orientation polarization, which is achieved by initially poling (E_p) at high temperatures above glass transition temperature ($T_p > T_g$), then lowering T_p below T_g in the presence of E_p. Therefore, the induced polarization of amorphous piezoelectric polymers is in a quasi-stable state instead of thermal equilibrium due to the freezing-in molecular dipoles below T_g. The characteristic features of several amorphous piezoelectric polymers, poly acrylonitrile (PAN), poly(vinylidene cyanide-vinyl acetate) (PVDCN-VAc), poly(phenyl ether nitrile) (PPEN) and nitrile substituted (β-CN) 4,4′ oxydiphthalic anhydride (ODPA) dianhydride and bisaminophenoxybenzene (APB) diamine based polyimides
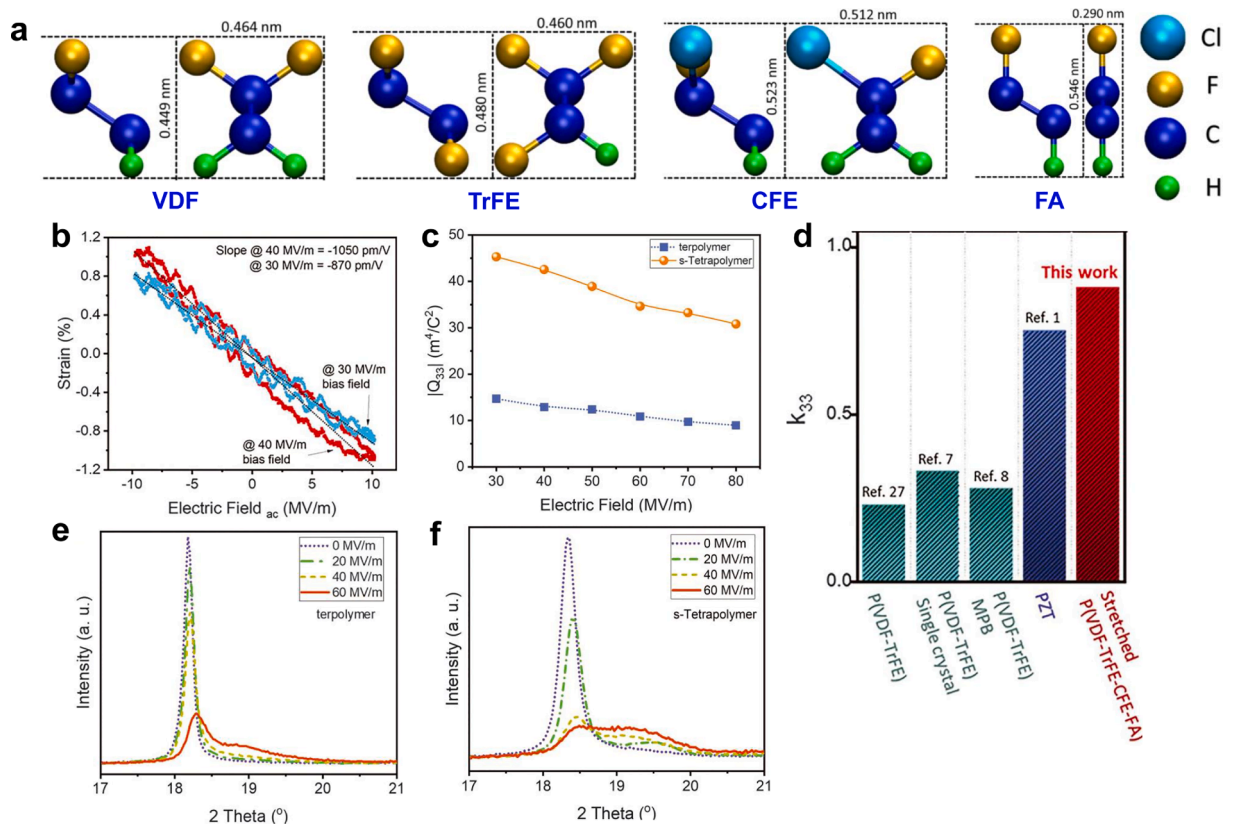
Fig. 6. (a) The schematic diagram of chemical structure of VDF, TrFE, CFE and FA monomers. (b) Strain at bias fields of 30 and 40 MV/m, and 1 Hz. (c) Electrostriction coefficient $|Q_{33}|$ as a function of applied electric field for terpolymer and stretched tetrapolymer. (d) A list of k_{33} for commercial P(VDF-TrFE) film, P(VDF-TrFE) single crystal, MPB engineered P(VDF-TrFE), PZT ceramics and stretched P(VDF-TrFE-CFE-FA) tetrapolymer at bias field of 40 MV/m. The dependence of electric fields on the XRD patterns of (e) terpolymer and (f) stretched tetrapolymer films (s-Tetrapolymer). Reproduced from [97], with the permission of American Association for the Advancement of Science.

Table 3
Characteristic features of typical amorphous piezoelectric polymers.

Polymer	Chemical structure	T_g (°C)	μ (Debye)	N (10^{28} m^{-3})	d_{31} (pC N^{-1})	k_{31}	ε	Ref
PAN		90	3.4	1.48	2	0.01	38	[101]
PVDCN-VAc		170	4.5	0.44	10	0.05	3	[102]
PPEN		145	4.2	0.37	–	–	5	[103]
(β-CN) APB/ODPA		220	8.8	0.14	–	–	4	[104]
PVDF comparison		−35	2.1	18.4	25–30	0.078	10	[105]

T_g: glass transition temperature; μ: dipole moment; N: dipole concentration (number of dipoles per unit volume); d_{31}: piezoelectric strain constant; k_{31}: electromechanical coupling coefficient; ε: measured at room temperature and 1 kHz.

((β-CN) APB/ODPA), are summarized in Table 3.

The dipoles in Table 3 of amorphous piezoelectric polymers are typically reliant on polymer backbones but can also be found in polymer mainchains such as the anhydride units in (β-CN) APB/ODPA. Both the dipole moment (μ) and dipole concentration (N) determine the polarization (P), $P = N\mu$. These amorphous piezoelectric polymers show higher μ, however, their much lower values of N result in smaller polarization compared to PVDF. A need of high temperature piezoelectric applications motivates the studies of amorphous piezoelectric polymers especially the ones with high T_g, for example, (β-CN) APB/ODPA can maintain its piezoelectricity at temperature even up to 150 °C.[104]

3. Mechanism

Currently, there are two mainstream theories to elaborate the mechanism of piezocatalysis: energy band theory and screening charge effect.[39] For energy band theory, the intrinsic energy band levels, namely conduction bands (CB) and valence bands (VB), determine the catalytic behavior of specific chemical reactions. Thus, the piezopotential acts as the driving force to tilt the band levels, endowing the energy of electrons/holes with the ability to participate in redox reactions. In comparison, screening charge effect points out the major role of external screening charges in the catalytic behavior. Here piezopotential directly determines the reactivity of materials, which should be equal to or greater than the Gibbs free energy change of the reaction. Despite the fact that both theories have been reasonable in explaining the piezocatalytic effect in classic reactions, such as water oxidation and dye degradation, different focuses have been addressed in regulating the reaction process or optimizing the catalytic efficiency. In the following section, we will explore the theory behind the two mechanisms and look into the difference between them.

3.1. Energy band theory

In energy band theory, the change of polarization state endows piezoelectric materials with the ability of band structure modulation, further enhancing the redox ability. As a result, a built-in electric field will be established when the piezopotential is generated under mechanic stimuli, changing the energy of charge carriers and further tilting the energy bands. In detail, electrons from the CB of the piezoelectric material will flow to participate the reduction reaction, while holes from the VB of the material will flow to the other end when the oxidation reaction takes place. Fig. 7 shows a schematic description of piezocatalytic formation of $\cdot O_2^-$ and $\cdot OH$ based on the theory of energy band. A piezoelectric material is initially thermodynamically unfavorable for the reduction of O_2 and the oxidation of H_2O due to the mismatch of energy band structure (E_{CB} is less negative compared to the redox potential of $O_2/\cdot O_2^-$, E_{VB} is less positive compared to the redox potential of $H_2O/\cdot OH$). However, the energy band is significantly titled due to the presence of piezopotential (φ_P) when the piezoelectric material is subjected to mechanical strain, which shifts the positions of energy band towards the potentials of redox reactions.

In terms of the free charge carriers involved in piezocatalysis, whether the source arises from the mechanical excitation or the intrinsic lattice structure is still in debate.[106] It has been proposed that the mechanical force, e.g. ultrasound, can directly excite the electrons from the VB to the CB based on the collapse of cavitation bubbles under ultrahigh pressure (up to 10^8 Pa) at the interface between the material and solution.[107] Apart from the direct approach, an indirect way to generate electron-hole pairs could take place as well, which results from the 'hot spot' (~5000 °C) introduced by the thermal disturbance of collapsed cavitation bubbles. [108] In addition to the possibility of electron-hole pairs generated during the process of piezocatalysis, the free charge carriers derived from defects are worthy of remark when investigating the origin of electrons and holes in piezocatalysis.[108] For instance, anion defects in the lattice of transitional-metal oxides, e.g. oxygen and sulfur vacancies, are commonly introduced to produce more electrons considering the internal charge balance. Hence, defect engineering has drawn increasing intention to enhance the piezo-catalytic performance.[109] In sum, in order to clarify the contribution of external/internal source of free charge carriers, the correlation between required mechanical energy to excite electrons and intrinsic band structure of the material should be determined both experimentally and theoretically in the future.

A simplified model has been established to demonstrate the piezocatalytic process. A strained piezoelectric material can be
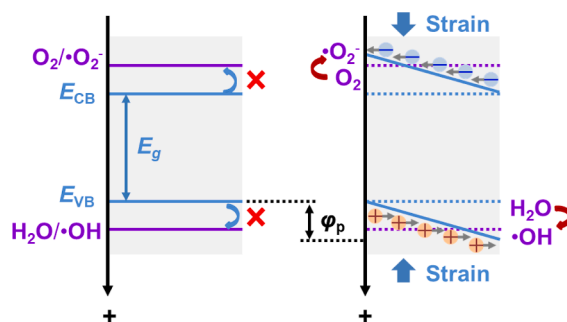

Fig. 7. A schematic illustration of the energy band theory of piezocatalytic mechanism using the redox reactions of $O_2 + e^- \rightarrow \cdot O_2^-$ and $H_2O + h^+ \rightarrow \cdot OH + H^+$, where E_{CB} and E_{VB} are the positions of CB and VB, respectively, E_g and φ_P are energy band gap and piezopotential, respectively.

considered as a charged capacitor. Supposing that a strained piezoelectric material is immersed in an aqueous solution with finite polarizability and conductivity, its piezopotential-induced surface charge (ΔQ_p) can be depleted through two pathways: Faradic (I_f) current and capacitive current ($I_c = dC_dV_d/dt$, in which C_d and V_d are capacitance and voltage drop across the double layer, respectively). As a result, ΔQ_p can be represented using the following formula:

$$\Delta Q_p = \int I_f dt + C_d V_d \tag{10}$$

Among the two pathways, the capacitive current is responsible for forming double layers in the vicinity of piezoelectric surfaces to screen surface charges, while the Faradic current is responsible for the transfer of charge from the piezoelectric surface to the solution and may initiate chemical reactions. It should be noted that this model shows the surface charge transfer dynamics in a single straining cycle and the piezopotential induced charges is immediately depleted by the capacitive and Faradic currents.

Considering that most piezoelectric materials are not perfect insulators, it should be noted that the built-in electric field can drive the mobile charges to accumulate in the opposite surfaces and screen the energy band tilting. Therefore, an alternating source of mechanical stimuli (e.g., ultrasound) is favorable to prevent the accumulation of mobile charges on the opposite sides. To date, the most common form of stimulation has been ultrasound. There is increasing evidence that there is a coupling of sonocatalysis associated with the enhancement of piezocatalysis. This explains why ultrasound remains the most commonly investigated external energy source to trigger the piezocatalytic process. There is a disadvantage with using ultrasound where recombination of mobile carriers limits the number of species able to perform chemistry, limiting piezocatalytic efficiency. Therefore, enough strain is essential to enable piezoelectric materials to drive a chemical transformation. Essentially, an optimal balance should be achieved between the frequency of ultrasound and the holding time of each strain cycle to drive the piezocatalytic process as efficiently as possible.

3.2. Screening charge effect

In contrast to the energy band theory, the mechanism of screening charge highlights the importance of surface screening charge in the participation of piezocatalytic process, rather than internal charge carriers. As mentioned above, the mechanically coupled piezo-induced internal electric field induces different electrical properties at surfaces. This is closely linked with the screening phenomenon of charges from any external system. The screening charge model of the piezocatalytic process was demonstrated based on the generation of reactive oxygen species (ROS) using BaTiO$_3$.[110] In the virgin state (Fig. 8a), surface bound charges are balanced by screening charges ensuring a neutral electrostatic state of the material. During the application of an external mechanical stress, the concentration of bound charge will change and there will be an associated movement of screening charges at the surface. Charges can
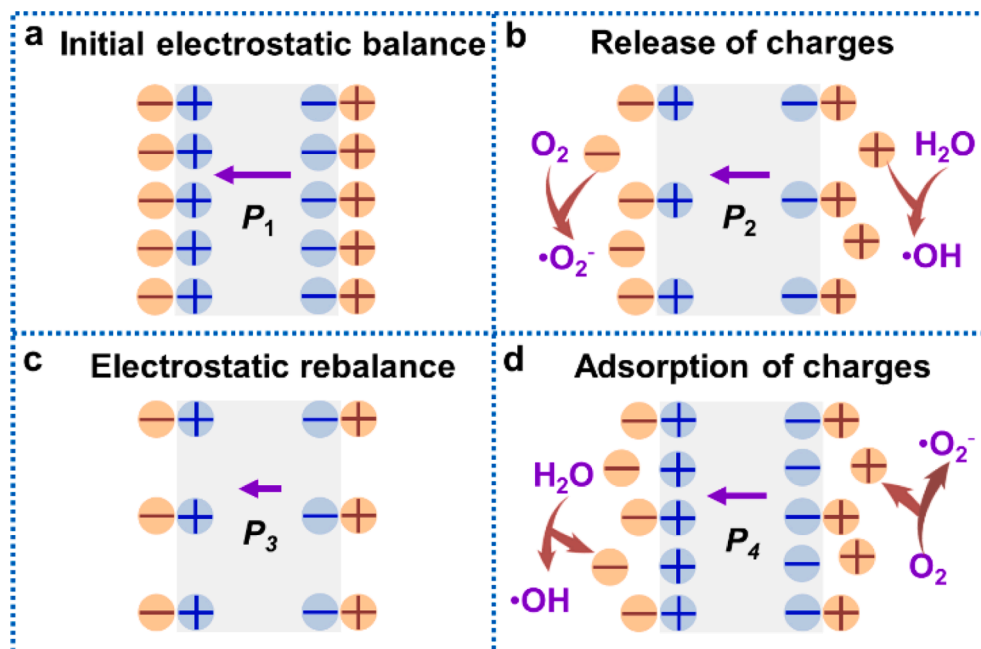

Fig. 8. The schematic description of the screening charge effect of piezocatalytic mechanism, where the orange and blue circles represent surface and bound charges, respectively, and P represents the polarization (reproduced from[110], with the permission of Nature Portfolio): (a) the initial state of the electrostatic balance of an as-polarized piezoelectric material; (b) the release of screening charges to generate the reactive oxygen radicals when the material is subjected to a compressive strain; (c) the state of a new electrostatic balance after the minimization of bound charges; (d) the adsorption of charges from the electrolyte when the compressive strain is reduced. (For interpretation of the references to color in this figure legend, the reader is referred to the web version of this article.)

leave the surface and react with local species such as water to produce ROS, e.g., ·OH and ·O_2^- (Fig. 8b). Before a new electrostatic balance is achieved, the screening charges will be continuously modified until the strain reaches the maximum level (Fig. 8c). Correspondingly, when the polarization is enhanced under stress, the bound charge density will increase with more screening charges adsorbed to the surface. Simultaneously, the charge carriers with opposed polarity will take part in the generation of ROS, e.g., ·OH and ·O_2^- (Fig. 8d). A piezoelectric material will continuously catalyze the redox reactions in terms of the release and adsorption of screening charges, utilizing the piezoelectrically driven potential as the driving force while there is an oscillating mechanical force.

The surface screening charge density is also demonstrated to be proportional to the piezoelectrically driven potential. The following formula was proposed to claim the relationship between screening charge density (σ_s) and polarization (P) based on a model of ZnO-electrode:

$$\sigma_s = \frac{d*P}{\varepsilon_r(\delta_1 + \delta_2) + d} \tag{11}$$

where d is the thickness of the materials, ε_r is the relative permittivity, δ_1 and δ_2 are the thicknesses of the screening charge layers of the two electrodes. It shows that a large polarization will lead to a higher screening charge density, which enables more charges to
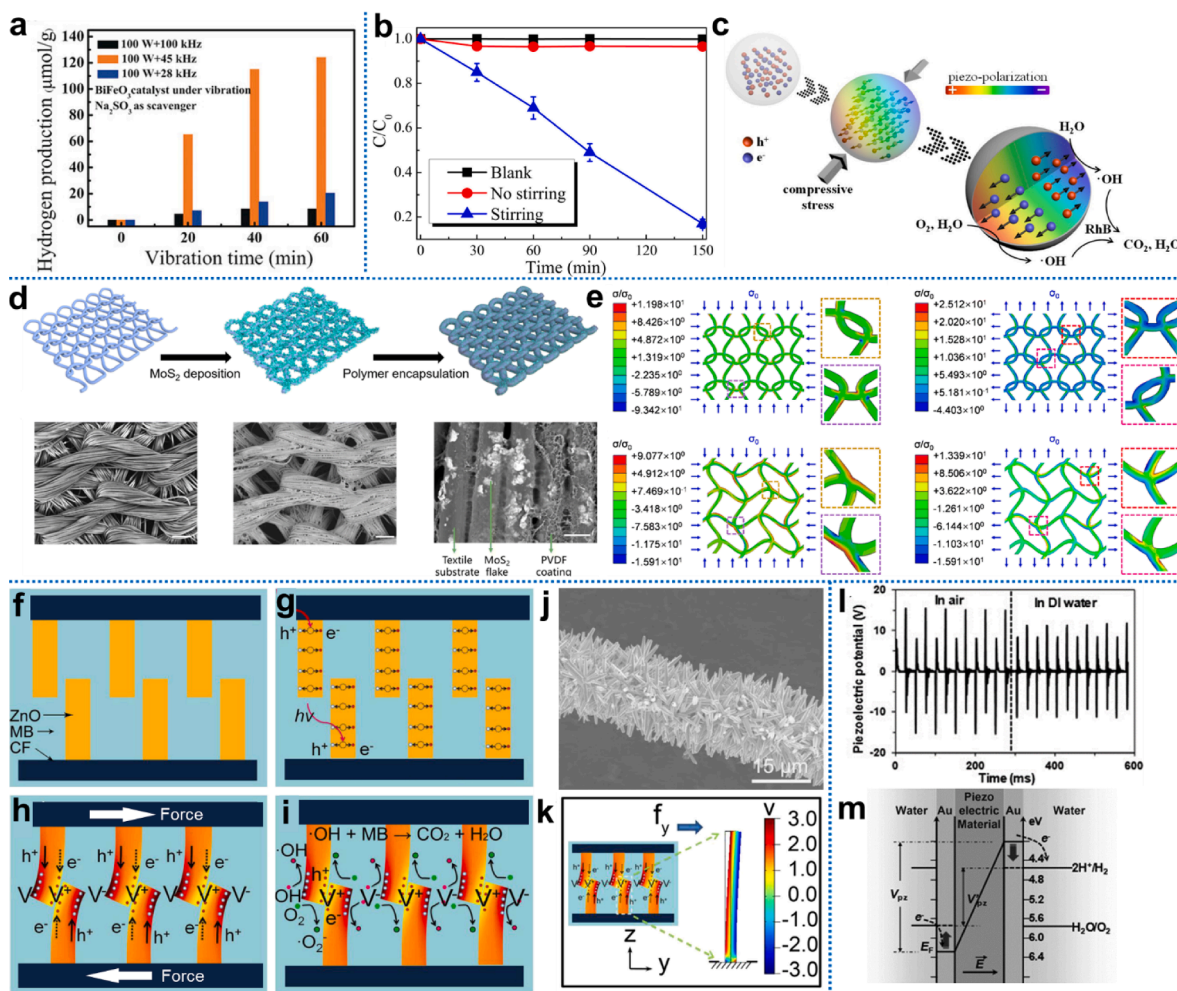

Fig. 9. (a) The hydrogen evolution rate of BiFeO$_3$ nanosheets at different ultrasonication frequencies, highlighting the enhancement arising from resonant frequency (reproduced from [111], with the permission of Wiley). (b) The degradation of RhB using Zr-rich PZT doped with BFO under stirring at 300 rpm, and (c) the proposed mechanism (reproduced from [112], with the permission of Elsevier). (d) The preparation of MoS$_2$ deposited knitted textiles, and (e) the stress distribution in a planar fabric upon the application of a biaxial load (reproduced from [24], with the permission of Royal Society of Chemistry). The schematic illustration of the working mechanism of catalytic activity of ZnO nanowires/CFs: (f) pristine state, (g) the transition of electrons from VB to CB under illumination, (h) the generation of piezopotential under the application of periodic force and (i) the formation of hydroxyl radicals for the oxidization of organic dye; (j) the morphology of ZnO nanowires/CFs and (k) the simulated piezopotential of ZnO nanowires (reproduced from [114], with the permission of Elsevier). (l) The piezopotential of PZT cantilever in different environment, and (m) the proposed mechanism for the piezocatalytic water splitting using PZT cantilever (reproduced from [115], with the permission of Wiley).

participate in the redox reactions in the catalytic process. Compared with bulk materials, the value of potential generated in piezo-electric nanoparticles is still a significant challenge. It is desirable to optimize the polar structure of piezoelectric materials to enhance piezocatalytic efficiency.

Overall, the theory of screening charge effect highlights the role of piezopotential and screening behavior during the piezocatalysis. Piezoelectrically driven potential acts as the main driving force of the cyclic release and adsorption of external charges, which participate in the redox reactions. The magnitude of pizopotential not only determines the possibility of catalyzing a specific reaction, but also correlates with the screening charge density of the material, which is positively linked with the catalytic efficiency. Apart from the structure and properties of the catalyst, all the substances in the environment (e.g., aqueous solution) can have an impact on the catalytic process, which is usually overlooked in the theory of energy band.

3.3. Effect of different mechanical stimulation methods

The mechanical energy used to stimulate piezocatalysis can be roughly divided into high-frequency ultrasonication, low-frequency shear force, mechanical bending *etc*. The predominant method employed to induce the efficient deformation and periodic external strain on piezoelectric materials is ultrasonic irradiation, which is attributed to the intense pressure (up to 10^8 Pa) created by the collapse of cavitation bubbles. By manipulating the power and frequency of ultrasonication, the strength of mechanical stress can be readily modulated to optimize the piezocatalytic reaction. Considering the parameter of frequency, piezoelectric materials usually exhibit a maximum amplitude of vibration at the resonant frequency. BiFeO$_3$ nanosheets have been reported to show a piezocatalytic hydrogen evolution (124.1 μmol g^{-1}h^{-1}) at an ultrasonic frequency of 45 kHz (Fig. 9a), being much higher compared to the hydrogen generation at vibration frequencies of 28 kHz (20.4 μmol g^{-1}h^{-1}) and 100 kHz (8.3 μmol g^{-1}h^{-1}).[111] The enhancement of pie-zocatalytic performance is closely related to the resonant frequency (f_r) of BiFeO$_3$ nanosheets, which was calculated to be 46.5 kHz according to Equation (12),

$$f_r = \frac{\pi}{2}\left[\frac{1}{L^2}+\frac{1}{W^2}\right]\sqrt{\frac{D}{\rho}} \tag{12}$$

$$D = \frac{E \bullet h^3}{12(1-v^2)} \tag{13}$$

where L, W, D and ρ represent the length (380 nm), width (380 nm), bending rigidity and density (8344 kg m^{-3}) of BiFeO$_3$ nanosheets, respectively. D was further determined using Equation (13), where h, E and v are the thickness (20 nm), Yong's modulus (51 GPa) and Poisson ratio (0.33) of materials, respectively.

The practical implementation of ultrasonication stimulated piezocatalysis in industrial settings is hindered by its high energy input. Therefore, it is crucial to explore alternative mechanical stress, e.g., shear force induced by mechanical stirring, to achieve specific piezocatalytic reactions. Unlike ultrasonic vibration, the shear-induced pressure lacks the strength required to trigger significant potential in piezoelectric materials, which demands the amplification of water striking force to attain the threshold for specific re-actions such as generating radicals. Feng *et al.* doped the Zr-rich PZT with bismuth ferrite (BFO) to induce free charges in PZT mi-crospheres, and the produced materials can degrade 80% of RhB under stirring (300 rpm) at 20 °C in dark (Fig. 9b and 9c).[112] Designing porous materials has been proved to be a viable approach towards accomplishing this objective. For example, Shi *et al.* fabricated MoS$_2$ nanoflakes deposited knitted fabrics, which showed a RhB degradation efficiency of 97.3% under a gentle vibration of an orbital shaker (240 rpm) for only 30 min (Fig. 9d).[24] This excellent performance is largely ascribed to the abundant sites of stress concentration arising from the inherent curved and mesoporous structures of knitted fabric (Fig. 9e). Similarly, the three-dimensional porous structured Ni foam was used as substrates to vertically grow ZnO nanorod arrays, and the prepared hybrid system showed enhanced piezoelectric response even subjected to flow turbulences.[113]

Periodic mechanical bending or sliding has also been designed for piezocatalysis, which requires a special design of catalytic system. For example, Xue *et al.* produced carbon fibers (CFs) coated with vertically aligned ZnO nanowires (ZnO nanowires/CFs), which were then woven to make a multi-fibers device (Fig. 9f-j).[114] Upon the application of periodical force, ZnO nanowires un-derwent radical extrusion and moved against with each other when the CFs were aligned. Mechanical pulling one of the CFs led to the bending of ZnO nanowires, which generates a piezoelectric field to facilitate the migration of electron-hole pairs (Fig. 9k). Starr *et al.* designed a PMN-PT cantilever for piezocatalytic electrochemical H$_2$ production.[115] The cantilever underwent an oscillation at a constant frequency and amplitude. When the cantilever was connected to a circuit, a peak voltage of 10 V was detected during the mechanical oscillation of cantilever, which served as a periodic bias voltage to trigger the electrochemical reactions (Fig. 9l and 9 m). The evolution rate of H$_2$ was governed by the frequency and amplitude of oscillation, and the output of H$_2$ per oscillation showed a non-linear relationship with piezopotential.

3.4. Comparison to sonolysis, sonocatalysis

Sonolysis or sonochemical process uses ultrasound waves (without the presence of a catalyst) to decompose molecules in various solutions. It is an important technique to promote advanced oxidation processes (AOP).[116] The range of used ultrasound waves is 20–1000 kHz, which enables the splitting of water into numerous ROS such as ·OH, ·H and ·HO$_2$. Micro-sized cavitation bubbles form, grow and finally collapse within a few microseconds in sonolysis. The amount of energy released at the moment of the collapse of

bubbles enables the reaction with target molecules. These can occur at three-zones from interior to exterior: (1) hot-spot zone, (2) bubble–liquid interface and (3) bulk liquid. [117] Because of the conditions such as elevated temperature (~5000–10,000 K) and pressure (~1000 atm), hot-spot zone can decompose volatile components and hydrophobic molecules using pyrolysis reaction. Moreover, ROS are generated in hot-spot zone and participate into the sonochemical reaction with molecules, which continues at the bubble–liquid interface (temperature: ~2000 K; pressure: ~1.0 atm). The rate of reaction at the interface is higher compared to the exterior zone of bulk liquid (temperature: ~300 K; pressure: ~1.0 atm) due to the enhanced mass transfer driven by more collision/ interaction between radicals and molecules. The molecules can also be thermally decomposed at the interface of bubble–liquid owing to high temperature. The as-formed ROS tend to drift from the interface into the solution, which leads to a restrained sonochemical reaction in the zone of bulk liquid. The degradation of target molecules using sonolysis initiates at the hot-spot zone under the combined reaction of pyrolysis and the formed ROS due to the collapse of cavitation bubbles. However, sonolysis with ultrasound alone cannot effectively decompose hydrophilic toxins, which mainly arises from the formation of hazardous intermediates and the energy loss due to thermal dissipation.[118]

As a result, sonocatalysis with the additional application of catalysts (e.g., semiconductors) has been demonstrated to be an effective strategy to boost the degradation of toxic molecules. Three approaches have been used to elucidate the mechanism of sonocatalysis: heterogenous nucleation, photocatalysis and thermal catalysis.[118] The first mechanism of heterogenous nucleation describes that the solid particles of catalysts offer nucleation sites for the generation of acoustic cavitation bubbles. This is preferred compared to the homogenous nucleation on gas voids formed due to the thermal fluctuation of bulk solution in sonolysis. The second photocatalytic mechanism relates to emitted sonoluminescence due to the collapse of cavitation bubbles, of which the range of wavelength and intensity are calculated to be 200–700 nm and 0.098 W. For a typical sonocatalytic system, the light from sonoluminescence shows greater energy compared to the semiconductor's band gap. This can trigger the generation of electron-hole pairs and further formation of ROS such as $\cdot O_2^-$ and $\cdot OH$ at CB and VB. This is identical to the proposed mechanism of the photocatalysis of semiconductors. Lastly, the thermal catalytic mechanism arises from local elevated temperatures of the collapse of cavitation bubbles, which can also excite the semiconductor to form electron-hole pairs. The dominant mechanism is uncertain with respect to the photo- or thermal catalysis due to the high similarity and the difficult quantitative evaluation of these two processes. Accordingly, the formation of electron-hole pairs can be incorporated as a combined mechanism of photo-thermal-catalysis.

To strengthen the understanding of piezocatalytic mechanism, a comparison with sonolysis and sonocatalysis is summarized in Fig. 10. All the three types of catalysis share the similarity of producing ROS. The main difference of piezocatalysis is the dominant role of piezo-induced potential, which regulates the energy band structure and changes the density of surface charges of materials. During a process of piezocatalysis (average frequency: ~40 kHz), the influence of sonolysis is minor as confirmed by a generally weak degradation level of organic dyes (~10%), and more details are described in Section 6.1.1. Moreover, piezocatalysis driven by gentle forces is desirable and attractive in practical applications of large-scale environmental remediation. For example, a self-powered water-flow driven piezocatalytic reactor built on singe- and few odd-layered MoS$_2$ showed effective degradation of benzothiazole with an efficiency of 94.8% in a short time (~ 2.5 min).[119] A piezocatalytic device of Cu$_2$O@MoS$_2$/PVDF pipeline exhibits excellent degradation of norfloxacin at a flow rate of 1.398 L min^{-1}, and the degradation efficiency reached 99.3% in 40 min. [120]

3.5. Coupling with other catalytic technologies

The coupling of piezocatalysis with other catalytic techniques and a general description of pyrocatalysis are described in this session, which involves photocatalysis, electrocatalysis and tribocatalysis. Fig. 11 shows the schematic illustration of the mechanism of five catalytic technologies, where photocatalysis relies on the light to generate electron-hole pairs. The coupling of piezoelectric effect with photocatalysis, termed as piezo-photocatalysis, has been described in the section of Introduction. The migration of carriers within the region of space charge is regulated by the piezopotential induced built-in electric field, which in turn exerts an influence on the redox kinetics occurring at the interface of metal/semiconductor contacts and semiconductor/semiconductor heterojunctions.

Despite sharing the common feature of accelerating electrochemical reactions in terms of facilitating charge transfer, piezocatalysis
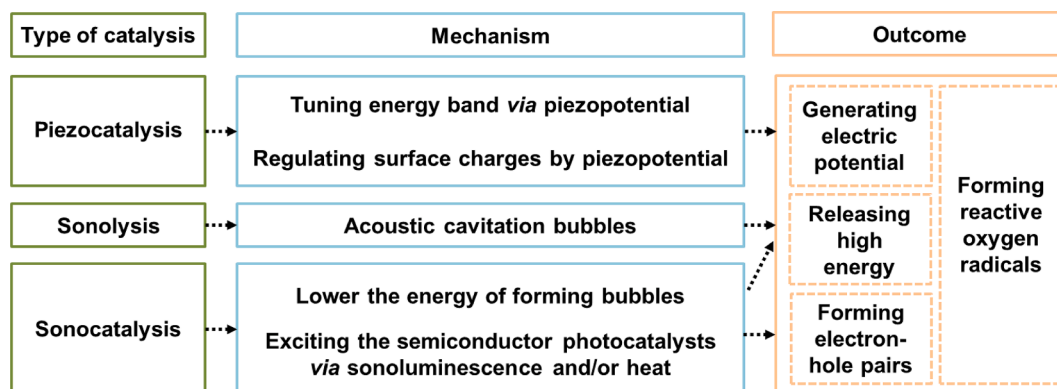

Fig. 10. A comparison of piezocatalysis, sonolysis and sonocatalysis involving mechanism and catalytic outcome.
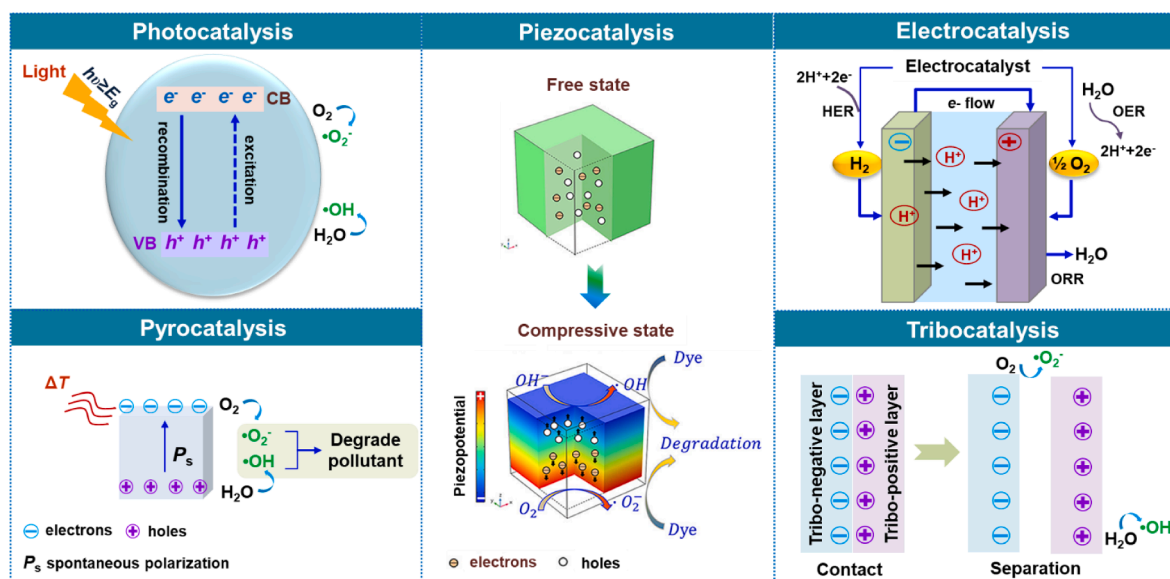
Fig. 11. A schematic illustration of the mechanism of five catalytic technologies, photocatalysis, piezocatalysis, electrocatalysis, pyrocatalysis and tribocatalysis (the mechanism of piezocatalysis was reproduced from [121], with the permission of American Chemical Society).

and electrocatalysis have their own benefits and drawbacks. One of the differences is that the electric field in electrocatalysis relies on the external DC power supply, while the electric field in piezocatalysis relies on the piezoepotential generated by the material under strain (Fig. 11). It should be noted that the applied mechanical strain sources are alternating in piezocatalysis and can lead to an alternating electric field as well. Therefore, the free electrons and holes can undergo opposite migration when the internal electric field is reversed, which may result in enhanced recombination of charge carriers and further deteriorate piezocatalytic efficiency. Electrocatalysis suffers from low current efficiency and high operating costs. With the purpose of making best of the strengths of both piezocatalysis and electrocatalysis, an electrocatalyst can be integrated with a piezocatalyst as power source. Feng *et al.* fabricated MoC quantum dots (QDs) encapsulated in ultrathin N-doped graphene (NG) vesicles (MoC@NG) based on a solid-state thermolysis approach.[122] When the composite is under mechanical stimulation, ultrathin NG layers can generate piezopotential to initiate hydrogen evolution reaction (HER) on MoC QDs, while MoC QDs can act as an electrocatalyst to accept free electrons to decrease the recombination of free charge carriers, and offer abundant highly-active sites. Finally, MoC@NG exhibits an enhanced H_2 evolution rate of 1.690 $\mu mol\ mg^{-1}h^{-1}$, which is higher compared to blank NG (0.469 $\mu mol\ mg^{-1}h^{-1}$), Mo_xC_y (0.377 $\mu mol\ mg^{-1}h^{-1}$) and mechanically mixed sample, Mo_xC_y/NG, with the same mass ratio (1.069 $\mu mol\ mg^{-1}h^{-1}$) (Fig. 12a). It is indicated that optimized catalytic performance results from the compound consisting of conductive MoC and piezoelectric NG. Moreover, piezocatalysis has been proved to enhance performance of an electrocatalytic system. Liu *et al.* designed and prepared a piezo-electrocatalytic sensor using ZnO nanorods and nanosheets to detect L-ascorbic acid (AA).[123] ZnO nanomaterials were synthesized on the ITO coated poly(ethylene terephthalate) film (ITO–PET) substrate. In this way, the mechanical stimulation was applied in terms of controlling the bending curvature of the substrate. The catalytic performance was evaluated based on the current change for different concentrations of AA. It can be seen that the catalytic efficiency was enhanced only with the presence of both ZnO nanomaterials and substrate deformation. In contrast, the catalytic behaviour was negligible in the absence of either ZnO or the deformation. As a result, the kinetic rate constant for the catalytic process, *k*, increased by 4.72 times in 0.4% deformed ZnO nanorods, compared to the undeformed ones (from 0.00127 to 0.00727 $\mu A\ \mu m^{-1}$) (Fig. 12b). Furthermore, *k* exhibited an increase as the strain increased for both ZnO nanorods and nanosheets (Fig. 12c). It reveals that larger strains could lead to a further increase of catalytic performance, which may benefit from the enhancement of piezoelectric properties. To summarize, piezocatalysis and electrocatalysis can be complementary in some circumstances, and a comprehensive understanding of the synergistic mechanism of the two catalytic methods will expand their application scenarios in the future.

In addition to piezocatalysis, tribocatalysis is another emerging strategy to facilitate chemical reactions by harvesting mechanical energy. There are two potential mechanisms for tribocatalysis, namely electron transfer across atoms and electron transition.[127] For the theory based on electron transfer across atoms, the electron transfer can be triggered by the friction between the material and the surrounding environment, as illustrated in Fig. 11. Meanwhile, catalysts can participate in the next step of reaction after gaining or losing electrons. This theory is normally applied to polymer-based materials considering their profound ability to acquire electrons by friction. For the theory based on electron transition, mechanical energy plays the role of exciting electrons from the VB to the CB of the catalyst, leaving holes in the VB and electrons in the CB. Next, the electrons and holes can react with molecules, e.g., water and oxygen to produce free radicals. Tribocatalyic behaviour relies on the energy band structure of materials. This theory is normally applied to semiconductor materials with distinct energy band structures. The differences between piezocatalysis and tribocatalysis have been demonstrated based on experimental results. Li *et al.* reported the tribocatalytic behaviour of $Ba_{0.75}Sr_{0.25}TiO_3$ (BST) nanoparticles
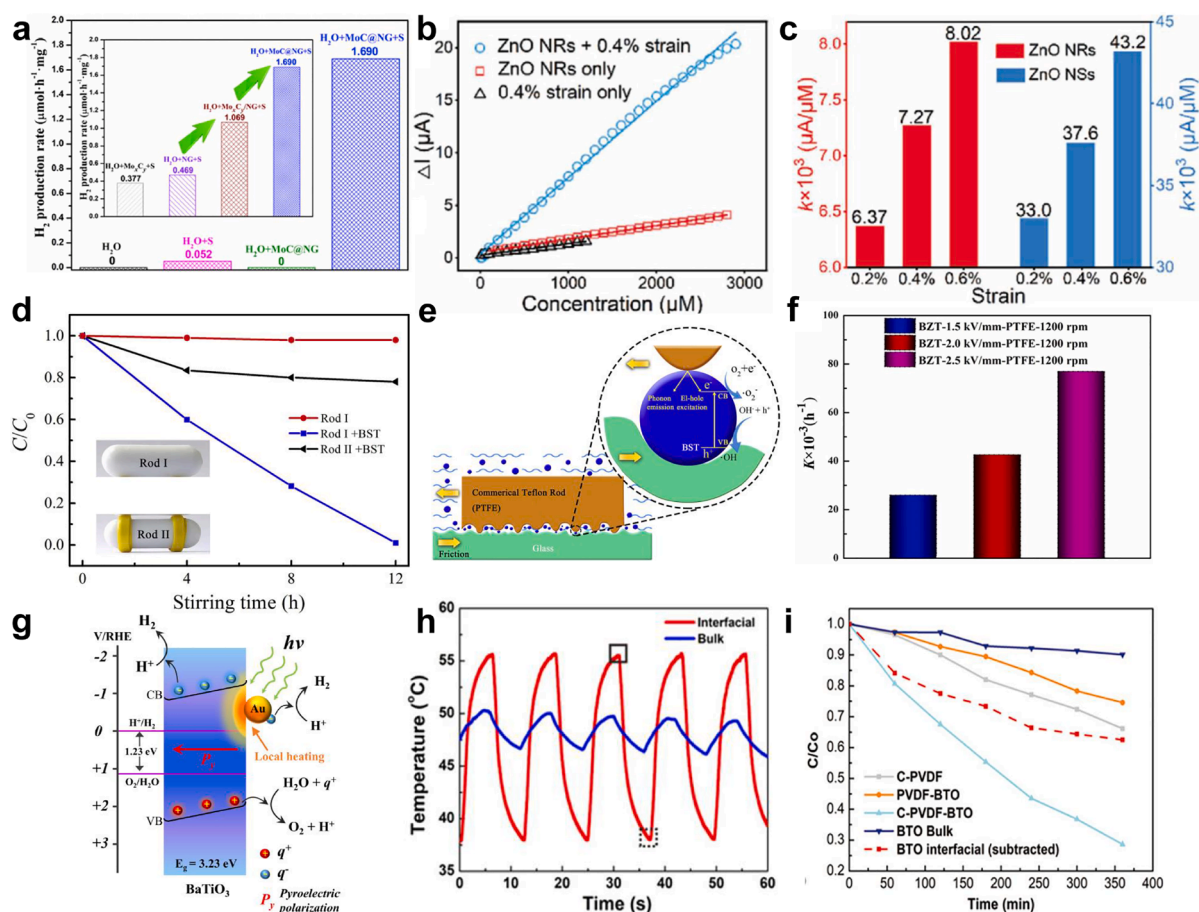
Fig. 12. Piezocatalysis coupling with other catalysis technologies: (a) A comparison of H$_2$ production rate with different treatments (reproduced from [122], with the permission of Elsevier). (b) The current changes of AA under 0.4% tensile strain in the presence of ZnO nanorods and strain, ZnO nanorods only and strain only (reproduced from [123], with the permission of Wiley). (c) Comparison of reaction kinetic constants of reaction with AA under different strain (0.2%, 0.4%, and 0.6%) (red: ZnO nanorods, blue: ZnO nanosheets) (reproduced from [123], with the permission of Wiley). (d) The decomposition efficiency of RhB under magnetic with Rod I (an as-received PTFE rod), with Rod I and BST, and with Rod II (a modified PTFE rod covered with two 1-mm thick rings of PVC electrical tape) and BST nanoparticles (reproduced from [124], with the permission of Elsevier). (e) Schematic illustration of tribo-catalytisis induced by BST nanoparticles under magnetic stirring (reproduced from [124], with the permission of Elsevier). (f) Comparison of reaction kinetic constants of RhB degradation using one PTFE bar and poled BZT at 2.5 kV mm^{-1} (reproduced from [125], with the permission of Elsevier). (g) Schematic illustration of pyrocatalysis-driven H$_2$ production induced by surface plasmon local heating of Au/BaTiO$_3$ nanoparticles (reproduced from [26], with the permission of Nature Portfolio). (h) Temporal temperature curve of Au/BaTiO$_3$ nanoparticles for the interfacial system and bulk solution system (reproduced from [126], with the permission of American Chemical Society). (i) Comparison of degradation curves of RhB as a function of time under different treatments (reproduced from [126], with the permission of American Chemical Society). (For interpretation of the references to color in this figure legend, the reader is referred to the web version of this article.)

which were synthesized using wet-chemical method.[124] With the addition of BST, the decomposition efficiency of RhB was up to ∼ 99.0% after 12 h of continuous stirring, which is unexpectedly higher considering piezocatalysis only. Furthermore, the decomposition efficiency of RhB was enhanced with four PTFE-based stirring rods compared to one stirring rod, ∼99.0% after 3 h of stirring. It is noteworthy that the catalytic efficiency decreased when the PTFE-based rods covered with two 1-mm thick rings of PVC electrical tape on the surface, which highlights the role of the friction between BST and PTFE-glass interface (Fig. 12d). Therefore, it is proposed that the electrons and holes were excited in BST nanoparticles after the mechanical energy absorbed from friction, which was supported by the detection of active species (·OH and ·O$_2^-$) during RhB decomposition (Fig. 12e). Similar to piezocatalysis, ferroelectric polarization can induce more charges and facilitate electron transfer in tribocatalysis. Tang *et al.* reported the enhanced tribocatalytic behaviour of Ba(Zr$_{0.05}$Ti$_{0.95}$)O$_3$ (BZT) nanoparticles after poling treatment.[125] The degradation efficiency of RhB increased with the increase of poling field, and BZT poled at 2.5 kV mm^{-1} exhibited the best tribocatalytic performance ($k = 0.0770$ h^{-1}) (Fig. 12f). The effect of poling treatment can be attributed to the introduction of more bound charges and further the tilt of band structure, which favours the generation of active species to participate in redox reactions. In sum, piezocatalysis and tribocatalysis can take place simultaneously, and the role of piezocatalysis and tribocatalysis play in the redox reactions should be clarified in future research works.

Pyroelectric materials are characterized as some piezoelectric materials exhibiting spontaneous polarization even in the absence of external strain, whereby their electric polarization alters in response to temperature fluctuation, and in turn generates pyropotential along crystals (Fig. 11). Pyropotential can be employed to modify the energy of surface charge, thereby triggering catalytic reactions through pyrocatalysis.[128] Similar to piezo-photocatalysis, pyropotential can improve the efficiency of charge separation and modulate the transport of photo-induced charge carriers across the interface of junctions, which enhances the efficiency of pyro-photocatalytic reactions. Unlike piezocatalysis and piezo-photocatalysis, the incorporation of pyroelectric effect to enhance photo-catalytic performance is still at its early stage of development, and the main challenge is the limited frequency of thermal cycling due to the large heat capacity of surrounding environment. You *et al.* proposed a strategy of locally heating $BaTiO_3$ nanoparticles using the thermo-plasmonic heating of decorated Au nanoparticles under illumination (Fig. 12g). The constructed $Au/BaTiO_3$ pyrocatalytic reactor showed a fine performance of water splitting with a hydrogen production rate of 133.1 ± 4.4 $\mu mol\ g^{-1}h^{-1}$ under illumination (786 mW cm^{-2}) for 60 min. [26] Photothermal effect, converting light to heat, offers another promising avenue for simultaneous localization of light and heat energy *via* the periodic application of solar irradiation on pyroelectric or photothermal materials. For example, a microporous PVDF membrane embedded with $BaTiO_3$ nanoparticles (pyroelectric coefficient: 200 $\mu C\ m^{-2}\ K^{-1}$) and carbon black powers as pyrocatalytic bottom and photothermal top layer, respectively, was positioned at the interface of liquid/air and combined with an optical chopper to realize a fast temperature change between 38.3 and 55.5 °C within a cycle of 12 s (Fig. 12h). [126] This designed pyrocatalytic system accomplished effective dye degradation, showing an efficiency of ~75% for RhB degradation within 6 h (Fig. 12i). It is noteworthy that the catalytic efficiency of the BTO NPs in the C–PVDF–BTO composite was estimated to be ~ 40% (dashed line with red triangles) after the subtraction of the efficiency of C–PVDF membrane from that of the C–PVDF–BTO membrane.

4. Correlation between catalytic performance and piezo/ferroelectric physics

Despite the underlying mechanism of piezocatalysis being under debate, the indispensable role of piezopotential plays during the catalytic process is widely acknowledged. In the theory of energy band, piezopotential regulates the band tilting of the semiconductor and drives the effective separation of charge carriers to participate in redox reactions on opposite surfaces. In screening charge effect, piezopotential determines the energy levels of surface screening charges and the catalytic performance is solely relied on the match between piezopotential and redox potential of specific reactions. Hence, the relationship between piezopotential and piezocatalytic efficiency has been studied both theoretically and experimentally. Based on the semiconductor and piezoelectric physics, electrostatic equations, current density equations, continuity equations, and the piezoelectric equations are generally involved to demonstrate piezotronic effect.[129]

Specifically, to investigate the relationship between the piezopotential and piezocatalytic efficiency, Su *et al.* conducted both the experimental results and theoretical simulations on $BaTiO_3$ nanomaterials with the variation of particle sizes and morphologies.[130] Compared with large-sized nanoparticles (200 nm) and nanowires, the small-sized $BaTiO_3$ nanocubes (10 nm) exhibited a larger longitudinal piezoelectric coefficient (0.45 nm V^{-1}). Furthermore, based on finite element simulation results, the maximized values of surface piezopotential values were calculated to be 2.6 V, 0.5 V and 1.2 V for 10 nm nanocubes, 200 nm nanoparticles, and nanowires, respectively. It should be noted that only the 10 nm $BaTiO_3$ nanocubes fulfil the requirement of the redox potential level for water splitting (1.23 V), which was confirmed by the highest rate of H_2 production (655 $\mu mol\ g^{-1}h^{-1}$) under ultrasound irradiation. Su *et al.* further reported the generation of heteroepitaxial interphase strain in porous $BaTiO_3$ nanoparticles to enhance the piezocatalytic performance.[131] The simulated piezopotential could reach 1.6 V owing to the polarization enhancement induced by strain engi-neering. The strain-engineered $BaTiO_3$ exhibited a promising performance of water splitting with production rates of H_2 and O_2 up to 159 and 75 $\mu mol\ g^{-1}h^{-1}$, respectively.

In addition to piezopotential, the strain state of a piezoelectric material affects the piezocatalysis process. In 2013, Starr *et al.* conducted a comprehensive theoretical analysis of the influencing factors in the piezocatalysis process on the basis of well-established theories covering piezoelectric, semiconductor, molecular orbital and electrochemistry.[132] Their results demonstrated that a high piezoelectric coupling coefficient and a low electrical conductivity were desired for obtaining high electrochemical activity. Considering the coupling of the strain state and electronic state of piezoelectric materials, the lattice strain in piezoelectric materials can also influence the adsorption behaviour of several molecules. Based on density functional theory (DFT), the change of the adsorption energy of *H/*OH on the strained/ unstrained $BaTiO_3$ could be calculated, and the enhancement of adsorption perfor-mance with the increase of strain was confirmed.[133] In 2023, Ai *et al.* reported the enhanced piezocatalytic performance of strain-engineered $BaTiO_3$ (s-BTO) as well.[134] Apart from the contribution of enhanced piezoelectricity, the adsorption and charge transfer behaviour of targeted molecules have been investigated. The adsorption energy of O_2, *OH and *H on the surface of s-BTO was calculated to be -0.45, -3.09 and -0.88 eV, respectively. On one hand, the Bader charges of O_2 and OH on s-BTO were calculated to be larger compared to BTO, demonstrating that O_2 and *OH gain electrons from BTO. On the other hand, the Bader charges of *H on s-BTO were calculated to be smaller compared to BTO, demonstrating that *H offers electrons to BTO. In sum, the lattice strain facilitated the adsorption behaviour of O_2, *OH and *H, and favoured the generation of more free radicals ($\cdot O_2^-$ and $\cdot OH$) and H_2.

Featuring the change of polarization with a change in temperature, pyroelectric materials are a special class of piezoelectric materials with spontaneous polarization which exists in the absence of an external electric field. If the spontaneous polarization can be reversed when an electric field is applied, this class of pyroelectric materials is called ferroelectric materials. Specially for ferroelectric materials, which features the domain structure with the existence of spontaneous polarization. Due to the unaligned direction of polarization in domains, virgin ferroelectric materials (without poling) usually possess inferior piezoelectric properties. Therefore, it can be stated that the catalytic performances of untreated ferroelectric material will not be very effective. Poling is an effective means

to align dipoles in a unidirectional way. The effect of poling was reported on a few ferroelectric ceramics where significant improvement of piezocatalytic efficiency was observed, which proves that optimizing the piezoelectric properties of materials is beneficial to the development of piezocatalysis. Non-ferroelectric piezoelectric materials, on the other hand, do not exhibit spontaneous polarization but can still generate an electric field in response to mechanical stress due to the piezoelectric effect, which has also been investigated in piezocatalysis.

4.1. Polarization rotation

In 2000, Fu and Cohen reported that the polarization rotation induced by an external electric field contributed to the large piezoresponse of single crystal of $BaTiO_3$.[135] Based on their first-principle calculation results, a flat energy surface, abundant charges and strong coupling between the internal degrees of freedom and strain were factors to consider in the design of materials with giant piezoelectric response. For example, bulk $BiFeO_3$ has a strong spontaneous polarization along the [111] direction with a rhombohedral structure ($R3c$), which leads to a large coercive field hampering polarization switching. Based on the Landau model, the energy barrier should be lowered to facilitate the polarization switching, thereby enhancing piezoelectric response.

In $BiFeO_3$, chemical substitution of A-site Bi^{3+} with La^{3+} is an effective method to reduce the energy barrier, in terms of polarization rotation from [111] of $BiFeO_3$ to [112] of BLFO ($Bi_{0.85}La_{0.15}FeO_3$) (Fig. 13a and 13b).[136] From the measured polar vector directions analyzed based on high-angle annular dark field scanning transmission electron microscopy (HAADF-STEM) images of BLFO, the extracted map of polarization reveals a polarization rotation from [111] towards [112] by $\sim 16.1°$, compared with $\sim 10.9°$ of pure $BiFeO_3$ (Fig. 13c-e). The coexistence of multiple phases with similar free energy is beneficial for polarization switching, resulting in the enhanced piezoelectric response to external mechanical stimuli.

Temperature is another important factor affecting the polarization and piezoelectric coefficient of ferroelectrics. Taking $BaTiO_3$ as an example, the spontaneous polarization P_s at room temperature is 0.26 C m^{-2} which drops to 0.22 C m^{-2} at about 80 °C and further reduces with the increase of temperature. When the temperature is above the T_c of $BaTiO_3$ (~120 °C), the intensity of spontaneous polarization and piezoelectric coefficient are zero due to the ferroelectric-paraelectric phase transition from a polar phase (tetragonal) to a non-polar phase (cubic). T_c is believed to have a prominent impact on any catalysis facilitated by polarization because the changes in polarization are maximized near T_c. Therefore, the piezoelectric performance can be tailored in consideration of shifting T_c near ambient temperature for piezocatalysis applications.

The synergy of multiphase coexistence and the gap between T_c and working temperature has been proved to play a crucial part in enhancing piezocatalysis behavior. For example, $BaTi_{0.89}Sn_{0.11}O_3$ (BTS) is a newly developed lead-free bulk material with ultrahigh piezoelectric coefficient ($d_{33} \sim 1100$ pC N^{-1}) and a low T_c (~ 40 °C). In 2021, Zhao et al. prepared BTS nanoparticles with multiple
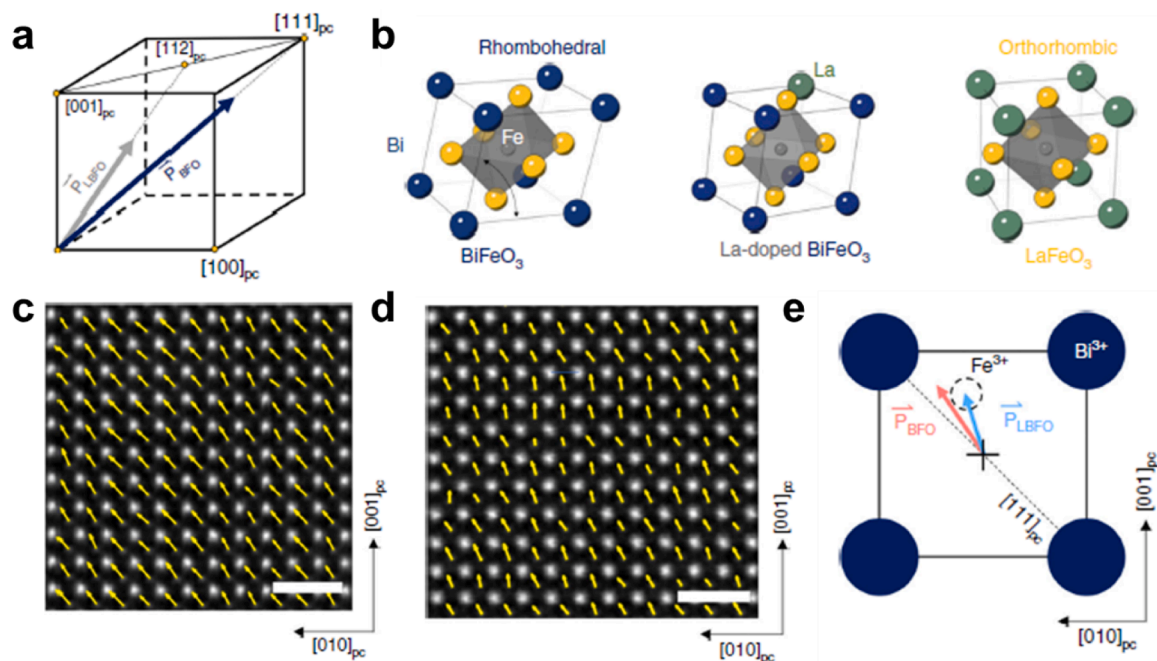

Fig. 13. (a) Schematic illustration of the ferroelectric polarization rotation from [111] ($BiFeO_3$) to [112] ($Bi_{0.85}La_{0.15}FeO_3$) and suppressed polarization induced by La-substitution in $BiFeO_3$. (b) Schematic illustration of the evolution of crystal symmetry from rhombohedral ($BiFeO_3$) to orthorhombic ($Bi_{0.85}La_{0.15}FeO_3$). HAADF-STEM images of (c) $BiFeO_3$ and (d) $Bi_{0.85}La_{0.15}FeO_3$ with the overlay polarization mapping of the Fe atoms. The scale bar is 1 nm. (e) Schematic ferroelectric polarization in $BiFeO_3/Bi_{0.85}La_{0.15}FeO_3$ unit cell. Reproduced from [136], with the permission of Nature Portfolio.

phases using a hydrothermal method.[137] Based on the Rietveld refinement of XRD patterns, a mixture of cubic (*C*, *Pm3m*), rhombohedral (*R*, *R3m*), tetragonal (*T*, *P4mm*), and orthorhombic (*O*, *Amm2*) phases could be identified for BTS nanoparticles (Fig. 14a). Considering the similar free energy profiles between non-polar phase (*C*) and polar phases (*R + O + T*), polarization switching could be facilitated by the multiple phase boundaries, resulting in the enhanced piezoelectric performance. In the PFM measurements, the displacement was up to 1600 pm with 50 V applied at 35 °C, which was over twice larger compared to BTS nanoparticles at 25 °C (Fig. 14b and 14c). Considering the T_c was characterized to be ~ 40 °C, BTS nanoparticles exhibited excellent piezoelectricity near T_c. As a reference to evaluate the piezocatalytic performance of BTS nanoparticles, the first-order reaction rate constant *k* was calculated to be 214.23 and 37.97 ($\times 10^{-3}$) min^{-1} at 35 °C for methyl orange (MO) and RhB degradation at 35 °C. The degradation rate was the highest near T_c (Fig. 14d and 14e). The decomposition efficiency of BTS nanoparticles is even comparable to that of some piezo-photocatalysts. In addition, the catalytic performance of BTS nanoparticles could be further enhanced after the deposition of noble metal (BTS@Ag), in terms of H_2 generation (401.1 μmol $g^{-1}h^{-1}$ at 25 °C in Fig. 14f). Moreover, the enhanced catalytic efficiency *via* large polarization variation near T_c was further verified by the pyrocatalytic activity of BTS under cold–hot excitation within different temperature intervals. RhB was evaluated to be completely degraded after 35 cycles of temperature change between 25 and 45 °C. In comparison, a lower decomposition rate of 53% was detected with BTS after 35 cycles of temperature change between 5 and 25 °C. The mechanism was further demonstrated in terms of pyroelectric response. As a result, the pyroelectric current within the temperature range near T_c was about twice lager compared to the temperatures much lower than T_c. This work illuminates the regulation of multiphase coexistence and T_c shifting to optimize the piezocatalytic efficiency.

4.2. Domain structure

In the previous section, lattice distortion related to the polarization rotation under mechanical stimuli is acknowledged as the intrinsic contribution to piezoelectricity. Correspondingly, domain switching contributes extrinsically to piezoelectricity. This has been intensively studied in polycrystalline materials (e.g., ceramics). Here we will look at how the structure of domains affects piezoelectric properties.

In classic lead-based piezoelectric systems, such as PZT and PMN-PT, their structures near MPB feature the construction of nanoscale domains, leading to a low anisotropy of polarization. The instability of polarized structure facilitates the motion of domain walls and a promising piezoelectric response. The advantage of nano-domain structure near MPB has also been confirmed in lead-free systems. Lead-free materials are more beneficial to the practical applications in environmental and biomedical fields due to their low toxicity and eco-friendly production. For example, a ferroelectric-ferroelectric MPB can be found in the Ba(Zr$_{0.2}$Ti$_{0.8}$)O$_3$–(Ba$_{0.7}$Ca$_{0.3}$)TiO$_3$ (BZT-BCT) system. The piezoelectric coefficient d_{33} near the MPB composition of BZT-BCT has been reported to reach 600 pC N^{-1}, which is comparable to soft PZT (d_{33} = 500–600 pC N^{-1}). BZT-BCT experiences a phase transition from *C* phase to non-centrosymmetric *R* and *T* phases with the variation of temperature from high to low, and MPB locates at the region between *R* and
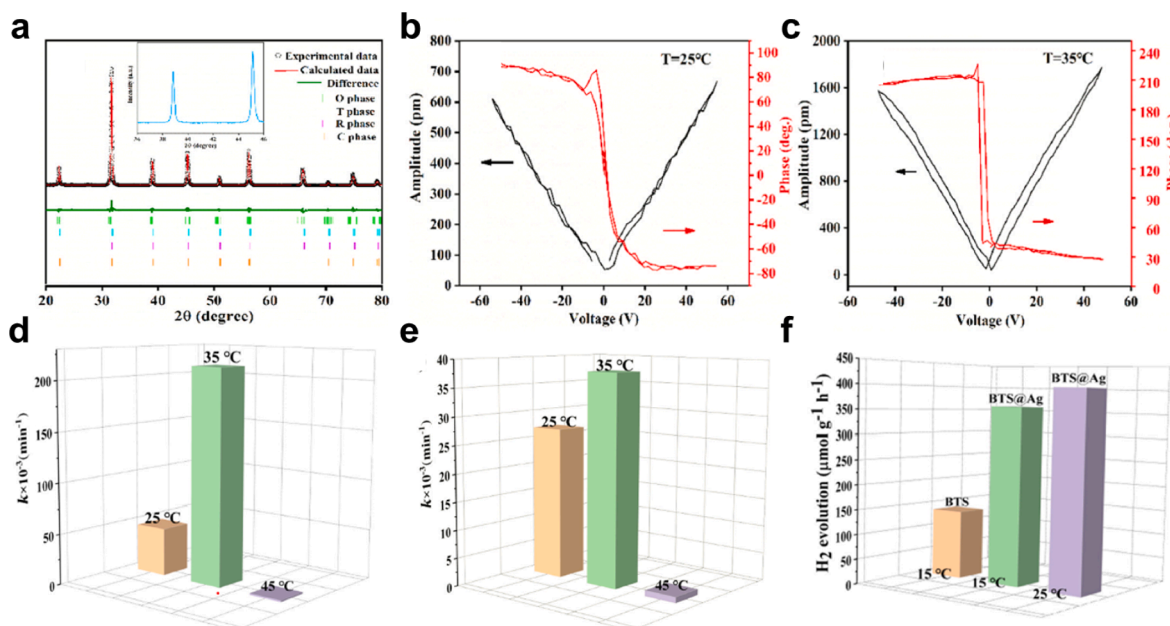
Fig. 14. (a) Rietveld refinement of XRD patterns of BTS nanoparticles, with the inset showing the enlarged patterns in the 2θ range of 36–46°. Hysteresis loops of BTS nanoparticles at temperature of (b) 25 °C and (c) 35 °C in PFM measurement. Comparison of reaction rate constant of (d) RhB degradation, (e) MO degradation and (f) H_2 production at different working temperatures. Reproduced from [137], with the permission of Elsevier.

T phases (Fig. 15a). The domain structure evolution was examined on the BZT-xBCT (x = 0.4–0.6) based on TEM investigation.[138] From the TEM images, the BZT-rich (x = 0.4) sample exhibits a rhombohedral domain structure, while BCT-rich (x = 0.6) one exhibits a tetragonal domain structure. Interestingly, the composition near MPB (x = 0.5) features the constitution of nanoscale domains with an average size of 20–100 nm within the obscured micro-sized domains (Fig. 15b). Likewise, the temperature-induced structure transition was characterized using the *in-situ* TEM cooling observation (Fig. 15c). At 60 °C, BZT-0.5BCT sample exhibited a micro-sized domain structure with tetragonal distortion. When cooled to 25 °C (near the transition temperature), the development of *R*-phase nanoscale domains in the lamellar *T*-phase microscale domains can be observed, which demonstrates the coexistence of *T* and *R* phases. When the temperature was further decreased to −150 °C, the nano-sized domain structure was completely replaced with micro-sized domains with *R*-phase. The domain structure of BZT-BCT undergoes the micron-nano-micron evolution within both the composition-induced and temperature-induced phase transitions. The best performing system near the composition-induced and temperature-induced phase transition points are coincident with the ones with the minimum scale of domains in all of the compositions and temperatures, respectively.

The thermodynamic theory was introduced to explain the enhanced piezoelectricity near MPB.[139] Taking the BZT-BCT system as an example, the MPB locates at a tricritical-triple transition point, which is consistent with an isotropic free energy state. When the system deviates from the MPB composition, a low level of polarization anisotropy energy can be expected. This may cause two major changes to affect piezoelectric response. First, a low polarization anisotropy energy near phase boundary is expected to increase the density of domain walls, thereby facilitating the motion of domain walls and enhancing piezoelectric response. Second, the low polarization anisotropy results in a lowered energy barrier of the two polar phases, and favors the rotation of polarization. Therefore, the intrinsic or extrinsic contributions of piezoelectricity cannot be considered separately. In fact, the phase regulation and domain structure engineering can work synergistically to enhance piezoelectric response. Specifically, the coexistence of multiple phases and the decrease of domain size are both favorable to the optimization of piezoelectric properties.

The piezocatalytic performance of BZT-BCT system was investigated by Wang *et al.* in 2022.[140] In this study, (1-x)Ba(Zr$_{0.2}$Ti$_{0.8}$)O$_3$–x(Ba$_{0.7}$Ca$_{0.3}$)TiO$_3$ (BCZT-x) powders were prepared *via* a solid-state reaction method. Based on the Rietveld refinement analysis results of XRD patterns, all of the BCZT-x compositions can be identified with multiple phases, consisting of major orthorhombic (*O*) phase with minor *T* and *R* phases (Fig. 16a). It should be noted that the *O* phase serves as the intermediate phase between *T* and *R* phases, which possesses the largest proportion (86.37 wt%) for BCZT-0.5, an optimal composition near MPB (Fig. 16b). Intriguingly, the ternary-phase MPB was proved to be related with the second-stage sintering, which was shown to contain *R* and *T* phases. Correspondingly, d_{33} was measured to be 27 pC N^{-1} for BCZT-0.5 without poling, being higher compared to BCZT-0.3 (24 pC N^{-1}) and BCZT-0.7 (16 pC N^{-1}) (Fig. 16c). ROS generation experiments were carried out under ultrasonic irradiation to evaluate the piezo-catalytic performance of samples with different compositions (Fig. 16d). For the yield of H$_2$O$_2$, BCZT-0.5 exhibited the best generation rate of 433 μmol g^{-1}h^{-1}, which was higher compared to BCZT-0.3 (353 μmol g^{-1}h^{-1}) and BCZT-0.7 (271 μmol g^{-1}h^{-1}). It should be noted that the improvement of catalytic efficiency can be linked with the enhanced piezoelectric properties in BCZT-x system (Fig. 16e). The content of intermediate *O* phase reached the highest in BCZT-0.5, which was located in the convergence region of the ternary phases at room temperature (Fig. 16f). This lowered the energy barrier for polarization rotation, thus increasing the piezo-electric coefficient.
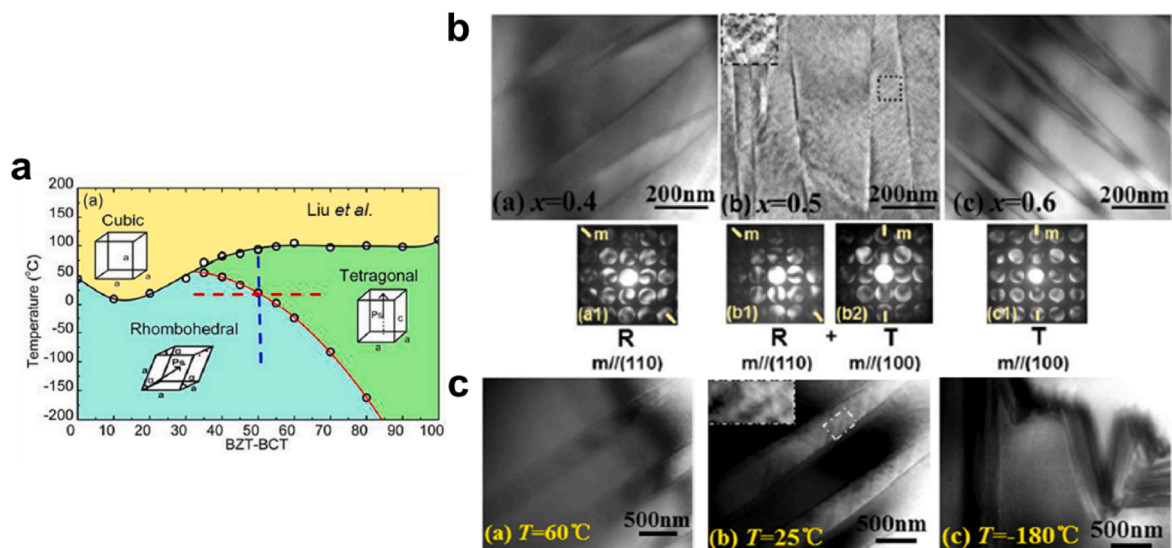

Fig. 15. (a) The phase diagram of Ba(Zr$_{0.2}$Ti$_{0.8}$)O$_3$-x(Ba$_{0.7}$Ca$_{0.3}$)TiO$_3$ (BZT-xBCT) with composition-induced and temperature-induced phase boundary. (b) The TEM images of composition-induced structure transition in BZT-xBCT (x = 0.4, 0.5, and 0.6 at 25 °C) from [0 0 1] incidence. (c) *In-situ* cooling TEM characterization of temperature-induced domain structure transition in BZT-0.5BZT (at 60 °C, 25 °C, and −180 °C) from [0 0 1] incidence. Reproduced from [138], with the permission of AIP Publishing.
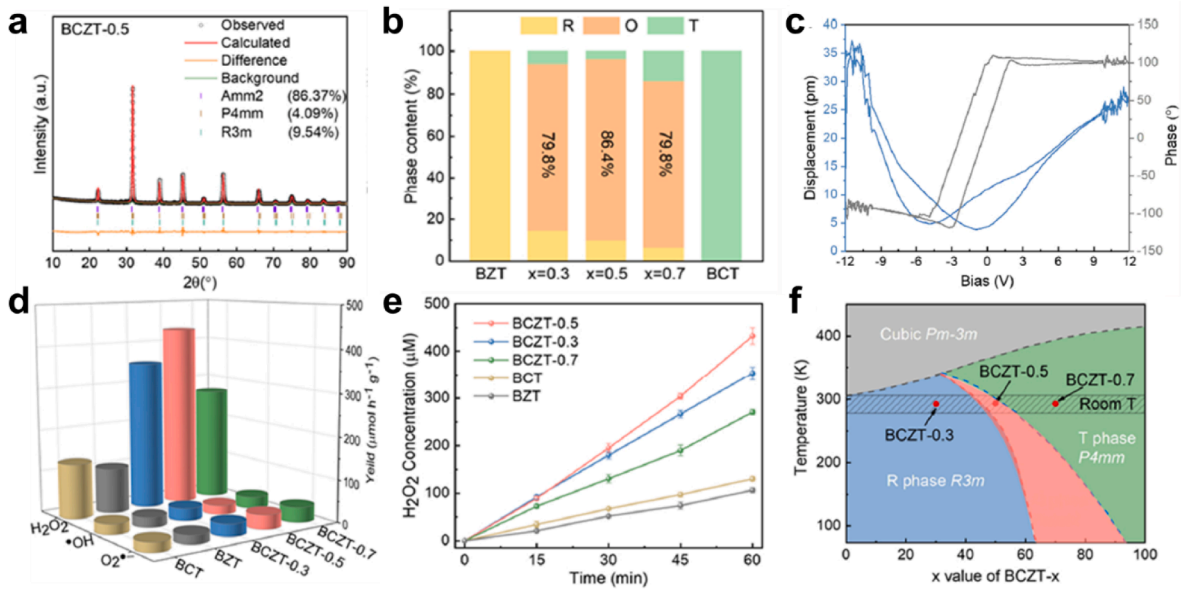
Fig. 16. (a) Refined XRD patterns of BCZT-0.5 (b) The relative phase content of the BCZT-x catalysts (c) Displacement-voltage butterfly loop and hysteresis loop of BCZT-0.5 based on PFM measurement. (d) A summary of the yield of ROS for different catalysts. (e) The generation rate of H_2O_2 for different catalysts (f) Phase diagram of BCZT-x. Reproduced from [140], with the permission of Elsevier.

4.3. Electric field-induced phase transition

The electric field-induced phase transition can be used to manipulate the piezoelectric properties of materials. The relaxor single crystals of $Pb(Zn_{1/3}Nb_{2/3})O_3$–$PbTiO_3$ and $Pb(Mg_{1/3}Nb_{2/3})O_3$–$PbTiO_3$ show a field-induced phase transition from the rhombohedral to tetragonal phase, which is ascribed to the incline of $\langle 111 \rangle$ spontaneous polarization to $\langle 001 \rangle$ direction, and contributes to a high d_{33} (2500 pC N^{-1}) and a large strain (0.6%).[64] Field-induced phase transition was also existed in lead-free materials. $BaTiO_3$ single crystal exhibits a transition from the tetragonal to monoclinic phase at 10 kV cm^{-1}, and further to rhombohedral phase at 30 kV cm^{-1},
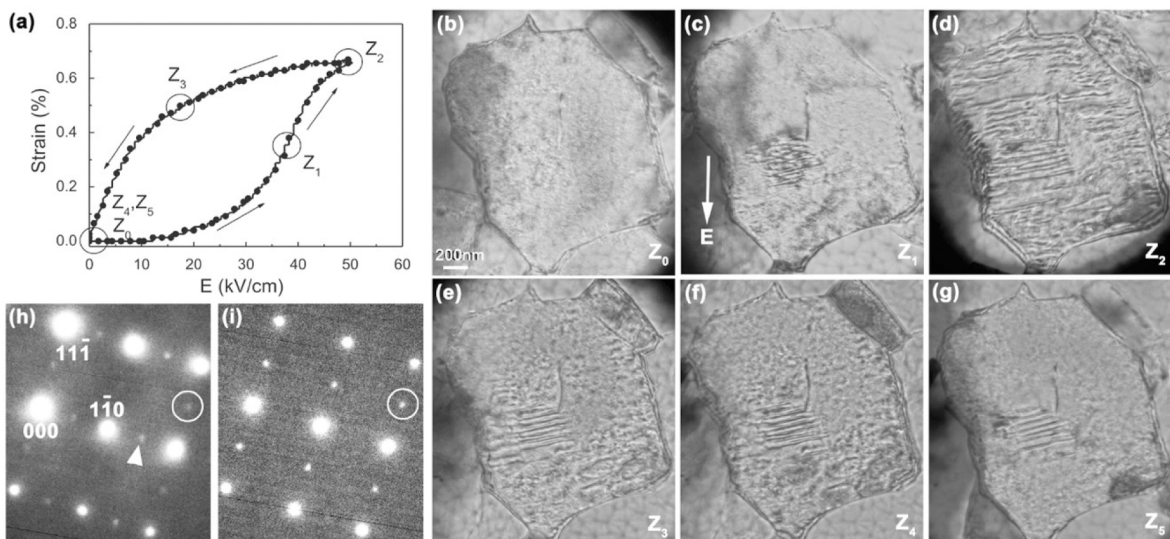

Fig. 17. The electric field-induced phase transition of BNT-2.5Nb ceramics: (a) the strain measurement under unipolar electric fields. The denoted points (Z_0-Z_5) correspond to the electric field applied in the characterizations of *in-situ* TEM, where Z_0, Z_4 and Z_5 represent the original state, the removal of electric field and four days' keeping at zero field of specimen, respectively. (b–g) The *in-situ* bright field TEM images of a grain along $\langle 112 \rangle$ axis, which correlates with the conditions of Z_0 to Z_5, respectively. The arrow in (c) indicates the positive direction of applied electric field. The SAED patterns of (h) the original state (Z_0) and state at the maximum electric field (Z_2) with the highlight of the superlattice diffraction spots of ½{*ooo*} and ½{*ooe*}. Reproduced from [142], with the permission of Wiley.

as a result, the piezoelectric coefficient d_{33} was enhanced (295 pC N^{-1}) under the exposure of electric field along [111] direction.[141] The electric field-induced phase transition of BNT-based materials has been well reviewed [60] and is widely adopted to develop materials with large strain. For example, $(Bi_{1/2}(Na_{0.84}K_{0.16})_{1/2})_{0.96}Sr_{0.04})(Ti_{1-x}Nb_x)O_3$ (x = 0.025, BNT-2.5Nb) was reported to show pronounced piezoelectric properties (strain: 0.7%; d_{33}: 1400 pm V^{-1}), which is largely attributed to the transition of ergodic relaxor (a mixture of $R3c$ and $P4bm$ nano-domains) to ferroelectric $R3c$ large domains.[142] Fig. 17 shows the detailed electric field-induced phase transition studied using *in-situ* TEM observations, where a typical grain along the zone axis of ⟨112⟩ exhibits obvious domain structures, and the superlattice spots of ½{*ooo*} and ½{*ooe*} displayed in the selected area electron diffraction patterns (SAED) clearly prove the presence of $R3c$ and $P4bm$ phases.

Moreover, the electric field-induced phase transition usually leads to the existence of multiple phases (e.g., monoclinic, rhombohedral, orthorhombic and tetragonal), and the intermediate monoclinic phase at the boundary of rhombohedral-orthorhombic, orthorhombic-tetragonal or rhombohedral-tetragonal phase favors the polarization rotation, thereby enhancing the piezoelectric performance. For example, $(Na,K)(Nb,Sb)O_3$-$LiTaO_3$ ceramics with a phase boundary of orthorhombic-tetragonal showed an irreversible transition from orthorhombic to monoclinic phase and a further reversible transition from monoclinic to tetragonal phase, which leads to a co-existence of monoclinic and tetragonal phase with a high instability. Such instability contributes to an easier polarization rotation and a further enhancement of piezoelectric properties.[143]

Despite the ubiquity of electric field-induced phase transition, its adoption in piezocatalysis has not been reported to the best of our knowledge, which would be opportune to comprehensively study the overall effect not only on the piezoelectric properties, but the energy band structure and the piezocatalytic activity of specific materials.
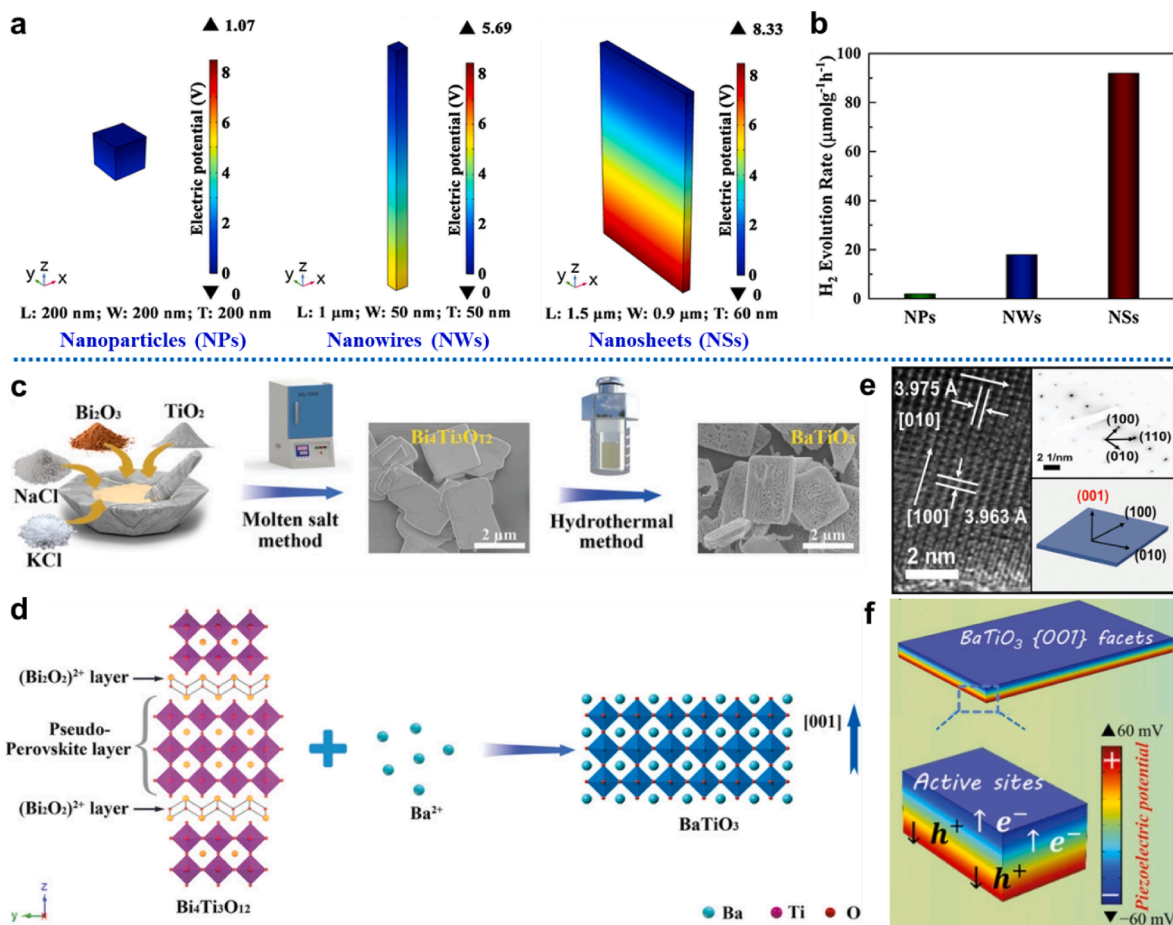

Fig. 18. The H_2 production of $BaTiO_3$ with different nanostructures (reproduced from [146], with the permission of Elsevier): (a) the COMSOL simulation of electric potential and (b) the H_2 evolution rate of $BaTiO_3$ nanoparticles, nanowires and nanosheets. Facets control of $BaTiO_3$ nanosheets (reproduced from [148], with the permission of Wiley): (c) the schematic fabrication route, (d) the proposed transformation from $Bi_4Ti_3O_{12}$ to $BaTiO_3$, (e) the HRTEM and selected area electron diffraction patterns and (f) COMSOL simulation of $BaTiO_3$ nanosheets with exposed (001) facets.

5. Design strategy of piezocatalytic systems

5.1. Morphology and facet control

The catalytic performance is highly dependent on the morphology of catalysts since the active sites on the surface of materials offer positions for the reaction between the induced charges and target molecules. Specially for piezocatalysis, a fast and extensive response to mechanical stress can generate a high electric potential, which governs the catalytic performance. Manipulating morphology to achieve high specific surface area and effective response to external mechanical stimuli is a valuable strategy to enhance the efficiency of piezocatalytic reaction. Shi *et al.* synthesized $Na_{0.5}Bi_{0.5}TiO_3$ nanoparticles with different sizes (340, 280 and 140 nm) and correspondingly different surface areas (3.45, 9.21 and 13.57 m^2 g^{-1}, respectively), where $Na_{0.5}Bi_{0.5}TiO_3$ with smallest size and highest specific surface area showed the most active piezocatalytic dye degradation.[144] Zhu *et al.* prepared electrospun $0.5Ba(Zr_{0.2}Ti_{0.8})O_3$-$0.5(Ba_{0.7}Ca_{0.3})TiO_3$ (0.5BZT-0.5BCT) microfibers, and tuned the diameter of fibers under different electrospinning voltage. 0.5BZT-0.5BCT fibers with smaller diameter showed higher piezocatalytic efficiency of dye degradation, which is positively correlated to a higher d_{33}, larger specific surface area with more exposed active sites and ease of deformation under mechanical stress.[145] Yu *et al.* fabricated $BaTiO_3$ with three different nanostructures (nanosheet, nanowire, nanoparticle), and $BaTiO_3$ nanosheets exhibited enhanced catalytic activity (hydrogen production rate: 92 μmol $g^{-1}h^{-1}$) compared to $BaTiO_3$ nanowires (18 μmol $g^{-1}h^{-1}$) and nanoparticles (2 μmol $g^{-1}h^{-1}$), which is mainly attributed to higher piezoelectric potential generated in 2D nanostructures arising from easier mechanical deformation (Fig. 18a-b).[146] Similar results were also presented in $Bi_4Ti_3O_{12}$ microplates,[147] showing more effective piezocatalytic degradation of methylene blue (MB) (efficiency: 94%; rate: 0.017 min^{-1}) compared to nanosheet-assembled hierarchical microrods (efficiency: 67%; rate: 0.007 min^{-1}) and nanoflake-assembled hierarchical microspheres (efficiency: 85%; rate: 0.012 min^{-1}).

Apart from the control of morphology, crystallographic engineering can be used to further boost catalytic performance of piezocatalysts. $BaTiO_3$ nanosheets with highly exposed (0 0 1) facets were prepared using a hydrothermal method based on the templates of $Bi_4Ti_3O_{12}$ nanosheets (Fig. 18c-f).[148] The exposed polar facets supply adequate reaction sites for the catalytic process, and the (0 0 1) out-of-plane polarization promotes the charge transfer to surface along a short distance perpendicular to the nanosheets, which in turn contributes to a higher rate constant (0.0835 min^{-1}) for dye degradation and a remarkable H_2 production with a generation rate of 305 μmol $g^{-1}h^{-1}$.
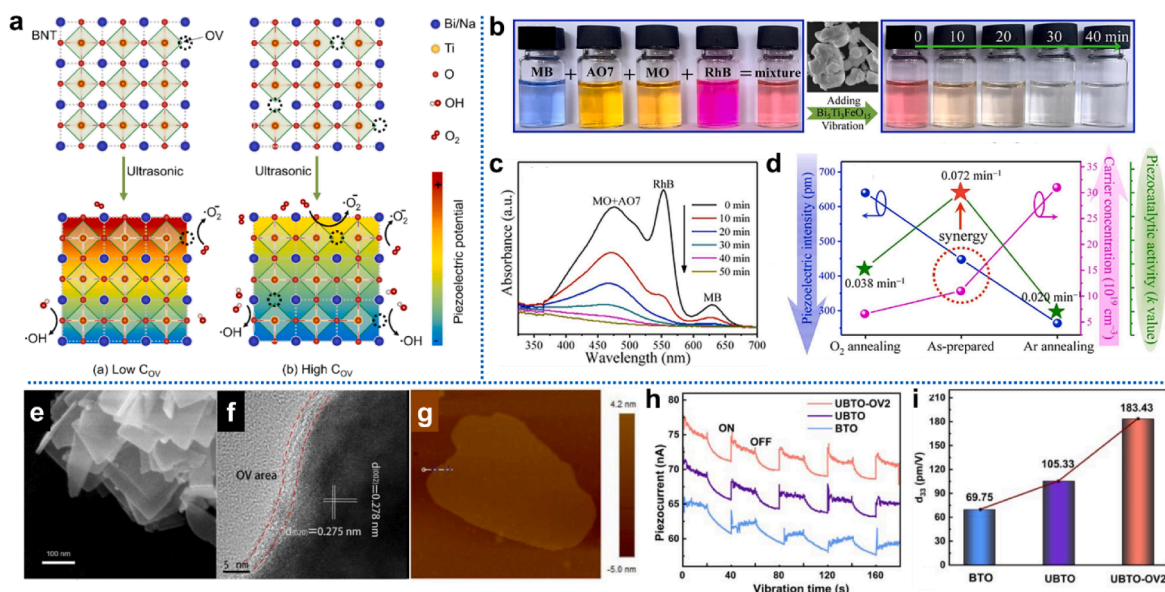

Fig. 19. (a) A schematic illustration of oxygen vacancies induced piezoelectric potential of BNT, where C_{ov} represents the concentration of oxygen vacancies (reproduced from [153], with the permission of Elsevier). The degradation of mixed dyes using $Bi_5Ti_3FeO_{15}$ nanoparticles (reproduced from [154], with the permission of Elsevier): (b) photos of mixed dyes before and after piezocatalytic degradation, (c) the UV–vis spectra of mixed dyes solution during catalytic process, and (d) a comparison of piezoelectricity, carrier concentration and catalytic performance three Bi_5Ti_3-FeO_{15} catalysts. The production of H_2O_2 using surface oxygen vacancies engineered atomic level ultrathin $Bi_4Ti_3O_{12}$ nanosheets (reproduced from [155], with the permission of Elsevier): (e) TEM, (f) HRTEM and (g) AFM images of ultrathin $Bi_4Ti_3O_{12}$ nanosheets with surface oxygen vacancies, (h) the piezocurrent response curves and (i) d_{33} of $Bi_4Ti_3O_{12}$ nanosheets (BTO), atomic ultrathin $Bi_4Ti_3O_{12}$ nanosheets (UBTO) and UBTO with optimized concentration of surface oxygen vacancies (UBTO-OV2).

5.2. Defects engineering

Defects are introduced to adjust the electronic structure, chemical and physical properties, and therefore catalytic performance of materials. Oxygen vacancies with electron-rich nature are ubiquitous in metal oxides, which can serve as reactive sites for redox reaction, regulate the charge distribution and promote the activity of catalyst. Oxygen vacancies can be generated *via* doping [149,150], post-annealing [151], light irradiation [152] *etc.* Liu *et al.* exploited different concentrations of oxygen vacancies to tailor the piezocatalytic activity of BNT, and adopted first-principle calculations to confirm the double-edged-sword role of oxygen vacancies in piezocatalysis.[153] A high concentration of oxygen vacancies promotes the adsorption of O_2 and OH^- as well as the formation of active oxygen species, but under a sacrifice of inhibited piezoelectric properties (Fig. 19a). $Bi_5Ti_3FeO_{15}$ nanoparticles with naturally moderate level of oxygen vacancies (24%, determined using X-ray photoelectron spectroscopy) were developed to purify textile wastewater.[154] The as-synthesized $Bi_5Ti_3FeO_{15}$ nanoparticles were annealed under the atmosphere O_2 (low oxygen vacancies: 20%) and Ar (high oxygen vacancies: 28%) to elucidate that either insufficient or excessive oxygen vacancies hinder the piezocatalytic activity. The as-synthesized $Bi_5Ti_3FeO_{15}$ nanoparticles show the most efficient dye degradation with a high rate constant of 0.072 min^{-1} (Fig. 19b-d). Similar results were also reported in $BaTiO_3$ nanobelts [109], $Sr_{0.5}Ba_{0.5}Nb_2O_6/Sr_2Nb_2O_7$ heterostructures [155], Bi_2WO_6 nanosheets [156], $ZnSnO_3$ nanowires [7], hydroxyapatite [157], where catalysts with moderate concentration of oxygen vacancies show the most enhanced piezocatalytic performance under the combined influence of favorable adsorption of O_2 and elevated piezoelectric potential. Wang *et al.* prepared atomic level ultrathin $Bi_4Ti_3O_{12}$ nanosheets (1–2 unit cell) with controllable surface oxygen vacancies for a two-step piezocatalytic production of H_2O_2 ($O_2 + e^- \rightarrow \cdot O_2^-$; $\cdot O_2^- + 2H^+ + e^- \rightarrow H_2O_2$) (Fig. 19e-i).[155] The surface oxygen vacancies were generated during a process of hydrothermal post-treatment using reductive glyoxal, and the amount of glyoxal was varied to control the degree of oxygen vacancies. The production of H_2O_2 showed a volcano-type trend with the concentration of oxygen vacancies. Notably, ultrathin $Bi_4Ti_3O_{12}$ nanosheets with optimized oxygen vacancies exhibit higher d_{33} compared to the as-synthesized ones, which may be attributed to the enhanced structure asymmetry induced by surface oxygen vacancies. Overall, the easier deformation of ultrathin nanosheets combined with improved piezoelectric properties endows $Bi_4Ti_3O_{12}$ catalysts a pronounced H_2O_2 production (generation rate: 1.61 mmol $g^{-1}h^{-1}$).

Compared to studies of oxygen vacancies, metal vacancies have been less well investigated in piezocatalysis. For example, Bi_2WO_6 (BWO) nanosheets with abundant Bi vacancies were prepared using an ion exchange method,[158] which showed excellent dye degradation with an efficiency and rate constant of 94.4% and 0.0783 min^{-1}, respectively, being a result of improved concentration of charge carriers. Moreover, Bi quantum dots were also decorated using surface plasmon resonance, which served as electron traps to avoid the combination of charge carriers and further enhanced the catalytic performance.
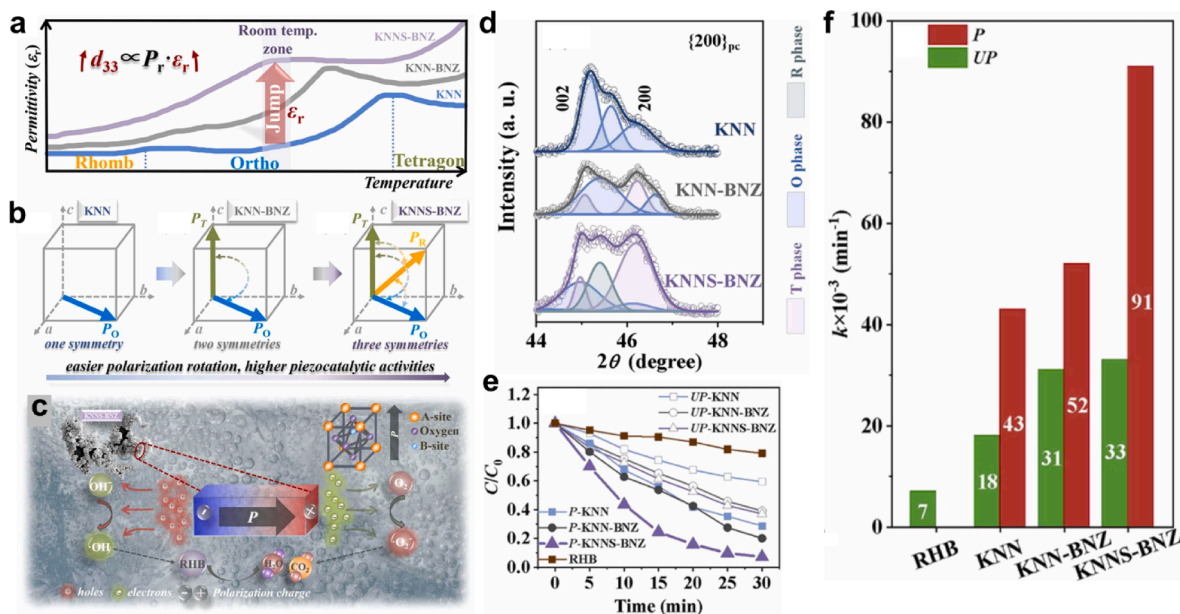
Fig. 20. Phase engineering of KNN-based materials (reproduced from [162], with the permission of Elsevier): (a) Dielectric temperature spectra correlated with different phases. (b) The vectors of spontaneous polarization for three different materials. (c) Schematic graph describing the mechanism of piezocatalysis. (d) XRD patterns of KNN-based materials in the 2θ range of 44-48°.– (e) Piezocatalytic degradation of Rhodamine B using unpoled KNN powders with/without metal oxides. (f) The rate constant (k) of piezocatalysis of unpoled and poled KNN-based powders.

5.3. Polarization modulation (ferroelectrics)

5.3.1. Phase engineering

Designing a system with preferred MPB is a facile and effective strategy to enhance the piezoelectric response of materials. For one of the classic ferroelectrics, PZT, the dielectric and piezoelectric properties exhibit an abrupt increase at/near the MPB. Within the MPB region, the coexistence of multiple phases with low energy barriers leads to the enhanced electromechanical responses to the external stimuli.[159] As a result, the charge carriers are separated more efficiently owing to the increase of internal electric field in MPB structures under the same mechanical stimuli, thus enhancing the piezocatalytic efficiency.[160] In recent years, the strategy of MPB construction has been reported in a few lead-free ferroelectric systems as well, beyond the limitation of PZT.[161] Sun *et al.* prepared three KNN-based materials (KNN, KNN-BNZ and KNNS-BNZ) with compositions of $(K_{0.5}Na_{0.5})NbO_3$, $(0.95(K_{0.48}Na_{0.52})NbO_3$-0.05 $(Bi_{0.5}Na_{0.5})ZrO_3$ and $0.96(K_{0.48}Na_{0.52})Nb_{0.955}Sb_{0.045}O_3-0.04(Bi_{0.5}Na_{0.5})ZrO_3$.[162] KNN, KNN-BNZ and KNNS-BNZ exhibited different crystal structures of orthorhombic, orthorhombic-tetragonal, and rhombohedral-orthorhombic-tetragonal, and their ε_r at room temperature followed an order of KNNS-BNZ > KNN-BNZ > KNN, which proves the enhancement of polarization rotation owing to multiple phases with distinct crystallographic symmetries (Fig. 20a-d). Poled KNNS-BNZ showed superior piezocatalytic dye degradation performance compared to other KNN-based materials (Fig. 20e-f). Wang *et al.* designed lead-free BaCaZrTi system for piezocatalytic H_2O_2 production.[140] The optimized $0.5Ba(Zr_{0.2}Ti_{0.8})O_3$-$0.5(Ba_{0.7}Ca_{0.3})TiO_3$ exhibited H_2O_2 selective generation (rate: 692 $\mu mol\ g^{-1}h^{-1}$; selectivity: 80%) owing to the significantly enhanced piezoelectric properties arising from co-existed ternary phases (orthorhombic, tetragonal and rhombohedral) with reduced energy barrier of polarization rotation. MPB engineering was also reported in BaCaSnTi system,[163] lithium modified $Na_{0.5}K_{0.5}NbO_3$-based materials,[164] ultrafine $BaTiO_3$ nanoparticles,[130] *etc*. Creating diffuse phase transition with polar nanodomains can strengthen the piezoelectric properties of $Ba(Zr_xTi_{1-x})O_3$,[165] which shows effective degradation of RhB.

5.3.2. Curie point manipulating

Ferroelectric materials exhibit transition from ferroelectric to paraelectric phase at Curie point, which contributes to a large change in polarization and possibly much enhanced dielectric permittivity and/or piezoelectric coefficients at temperatures approaching Curie point.[166] Piezocatalysis in the vicinity of Curie point has been demonstrated to be a new strategy for achieving high catalytic activity.[137,167,168] For example, Zhang *et al.* designed Nb-doped PZT (PZTN) with tunable polarization and a low Curie temperature (~ 40 °C) for water splitting using piezocatalysis (Fig. 21).[167] At temperatures below Curie point, the generated piezoelectric potential combined with sono-chemical process under ultrasonication contributed to the production of CO and H_2. At temperatures above Curie point, the properties of water splitting were reduced due to the only contribution of sono-chemical process. Around the Curie point, the large change of polarization promoted the separation and migration to surface of electric charges. As a result, ferroelectric PZTN materials showed the maximum production of CO and H_2 at a temperature approaching Curie point (~ 38 °C).
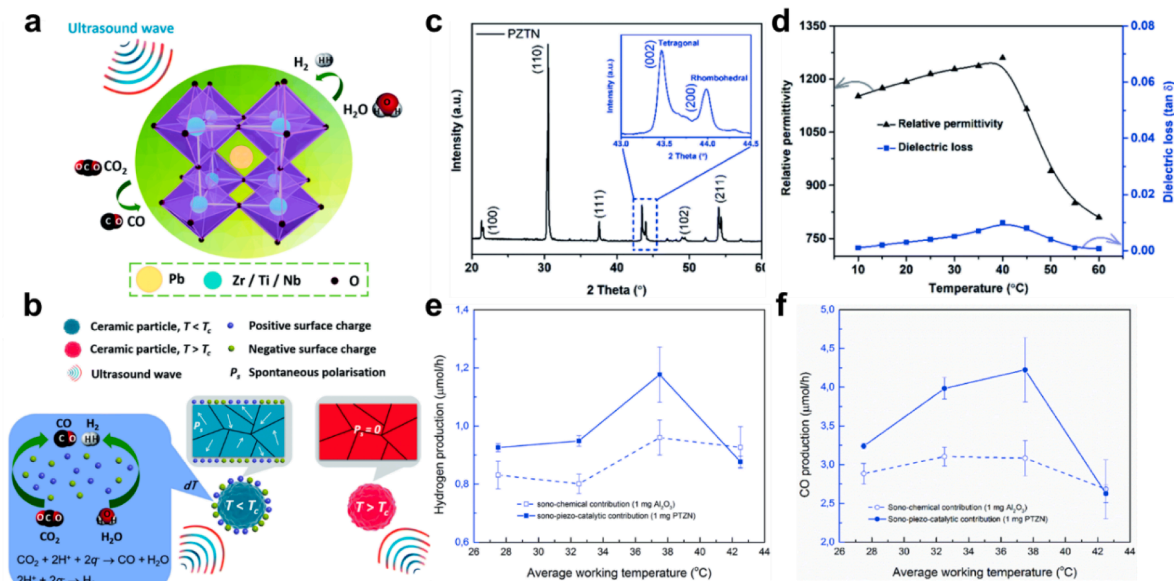
Fig. 21. Water splitting using Nb-doped PZT (PZTN) ferroelectric materials (reproduced from[167], with the permission of Royal Society of Chemistry): The schematic diagrams describing (a) the formation of CO and H_2 under ultrasonication and (b) the enhanced properties of water splitting at temperatures below Curie point due to the combined effect of piezocatalysis and sono-chemical process; (c) XRD patterns and (d) dielectric temperature spectra of PZTN; (e) hydrogen and (f) CO production rate as a function of working temperature using different catalysts of non-ferroelectric Al_2O_3 and PZTN.

5.4. Heterostructure construction

Heterojunction refers to a junction formed by two semiconductor materials with similar crystal structure, atomic spacing and coefficient of thermal expansion but different energy band gaps. Heterojunctions can be divided into p-p (two p-type semi-conductors), n-n (two n-type semi-conductors) and p-n heterojunctions (one p-type and one n-type). Heterojunctions can also be classified into three types with respect to their energy band alignment (Fig. 22), which are straddling gap (type I), staggered gap (type II) and broken gap (type III). In type I, semiconductor 1 (SC-1) shows more positive CB and more negative VB compared to semiconductor 2 (SC-2), being not favorable for separating charges since both the electrons and holes of SC-1 are shifted to SC-2. On the contrary, the type II band alignment of staggered gap offers the most advantageous charge separation, where the electrons from the CB of SC-1 are transported to that of SC-2, and the holes are shifted from the VB of SC-2 to that of SC-1. The broken gap (type III) is the least favorable band alignment for charge separation since there is no overlap in the bandgap of SC-1 and SC-2.

Heterojunction containing piezoelectric semiconductors shows enhanced catalytic behavior, which is attributed to the initiated charges on the surface of piezoelectrics or the tilt of energy band structure, triggering and/or accelerating the redox reactions at the heterojunction interface between semiconductors and reactants due to the promotion of charge transfer. Fig. 23 depicts three scenarios of heterojunctions composed of a n-type piezoelectric semiconductor with a p-type non-piezoelectric semiconductor, a p-type piezoelectric semiconductor or a metal.[169] A built-in electric field is constructed at the interphase of heterojunction under the equilibrium conditions, which arises from the energy-band offset due to the compensation for the unbalanced concentration of charge carriers (left panel in Fig. 23). New energy band alignment tends to be established when the piezoelectric semiconductors are subjected to external mechanical strain, being conducive to the charge regulation under the influence of formed piezoelectric polarization (middle and right panel in Fig. 23).

Cheng et al. synthesized Bi_2S_3-Bi_2WO_6 (BS-BWO) heterojunction via in-situ growing Bi_2S_3 nanorods on Bi_2WO_6 nanosheets and illustrated the piezo-catalytic mechanism using structural characterizations and density functional theory (DFT) calculations (Fig. 24a–d).[170] Bi-S bonds formed at the interface between Bi_2S_3 and Bi_2WO_6 in BS-BWO heterojunction. The DFT calculations were built on the optimized structures (Fig. 24a), which shows the active aggregation and consumption of electrons at the interface of heterojunction (Fig. 24b), and the electrons on the conduction band of Bi_2WO_6 were transferred to the valence band of Bi_2S_3 (Fig. 24c and 24d). Oxygen vacancies were used to engineer the piezocatalytic performance of $Sr_{0.5}Ba_{0.5}Nb_2O_6$/$Sr_2Nb_2O_7$ heterostructure.[171] Specifically, oxygen vacancies on the surface of $Sr_{0.5}Ba_{0.5}Nb_2O_6$ served as electron-rich sites to absorb and activate O_2, forming $\cdot O_2^-$ and $\cdot OH$ radicals. Moreover, a built-in electric field was generated at the junction area of $Sr_{0.5}Ba_{0.5}Nb_2O_6$/$Sr_2Nb_2O_7$, which further enhanced the piezocatalytic performance of hydrogen production with a higher efficiency (109.4 $\mu mol\ g^{-1}h^{-1}$) compared to pristine $Sr_{0.5}Ba_{0.5}Nb_2O_6$ (12 $\mu mol\ g^{-1}h^{-1}$). $BaTiO_3$/metal heterojunctions were built via a simple piezodeposition method, which involves mixing $BaTiO_3$ nanoparticles (diameter: 200 nm) with three types of metal chloride (K_2PtCl_4, $HAuCl_4$ or Na_2PdCl_4) followed by the ultrasound treatment to trigger the reduction reaction. The color change demonstrated the successful deposition of metals (Fig. 24f). The noble metal cocatalysts favored the charge regulation at the interfacial region, and significantly enhanced H_2 production in water (in the absence of O_2) under ultrasonic vibration. In the presence of dissolved O_2, $BaTiO_3$/metal exhibited different electron pathways, four-electron and two-electro pathways for $BaTiO_3$/(Pt, Pd) and $BaTiO_3$/Au, respectively (Fig. 24g). Similarly, Pd nanocubes were deposited in $BiFeO_3$ nanosheets (Fig. 24h-j) [172], which provides more active sites for proton reduction reaction, and facilitates the charge separation and induces the downward tilting of CB of $BiFeO_3$.

5.5. Composites creation

Organic/inorganic piezoelectric composite materials usually exhibit flexibility, durability and ease of recycling, which can effectively prevent the secondary pollution resulting from the sedimentation of materials with particulate form. The flexibility of composites further enables them to be more sensitive and conducive to collecting mechanical energy. Moreover, the piezocatalytic performance can be precisely tuned and enhanced through the structural design of composites.
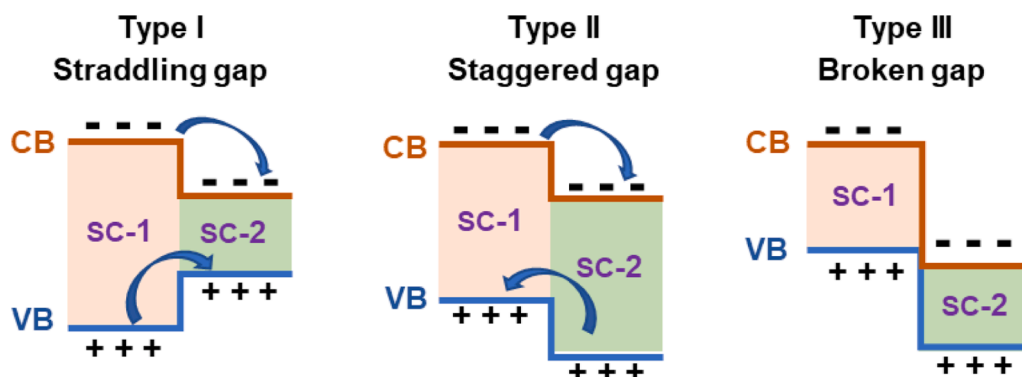

Fig. 22. Schematic diagram of different types of heterojunctions in terms of energy band alignment.
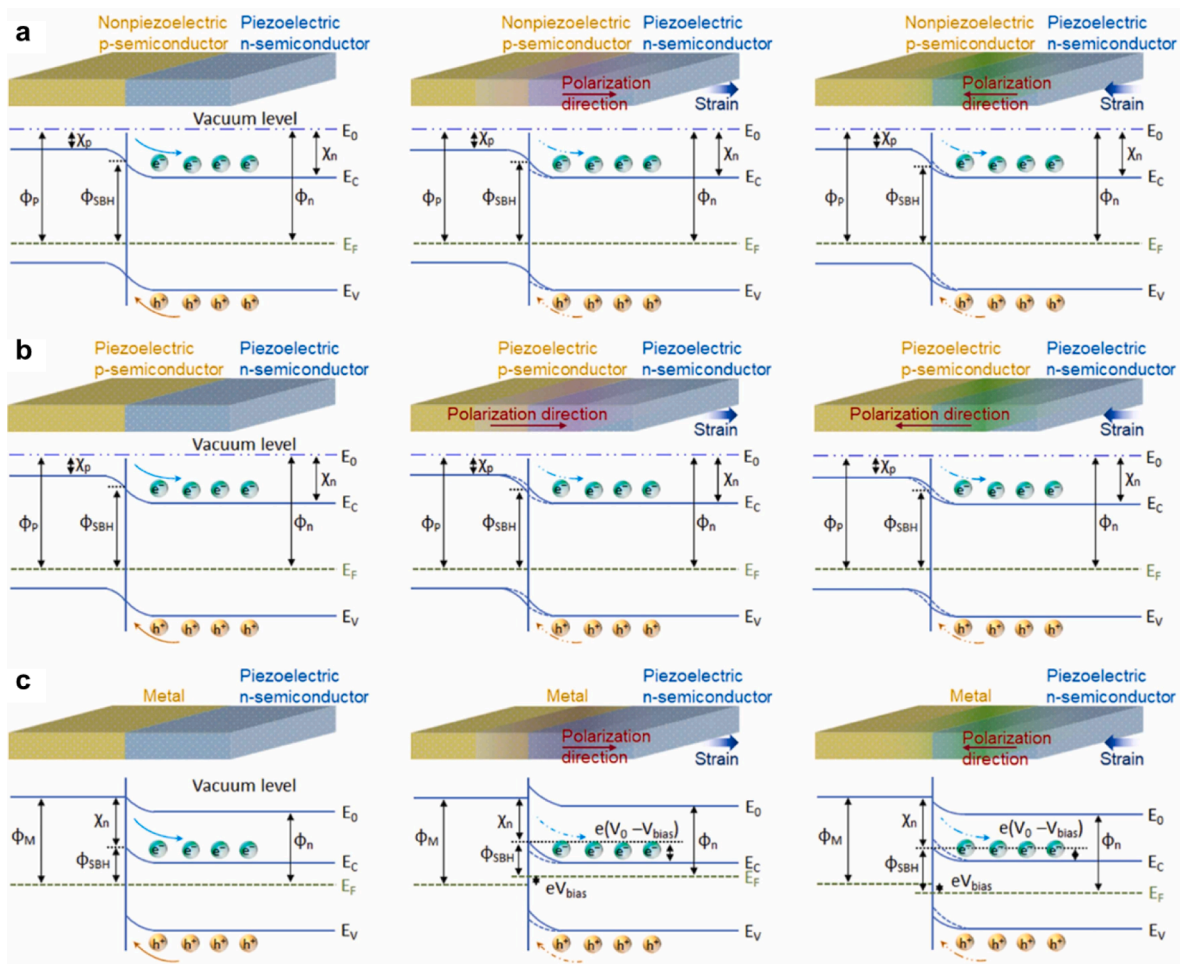
Fig. 23. The schematic diagram of the energy band alignment of heterojunction interphase between an n-type piezoelectric semiconductor and: (a) a p-type nonpiezoelectric semiconductor, (b) a p-type piezoelectric semiconductor and (c) metal, at equilibrium (panel left), under a negative piezoelectric polarization (panel middle) and a positive piezoelectric polarization (panel right). Φ_n, Φ_p, and Φ_m are the work function of n-type piezoelectric, p-type (non) piezoelectric semiconductors and metals, respectively. χ_n and χ_p represent the electron affinity of n-type piezoelectric and p-type (non) piezoelectric semiconductors, respectively. Φ_{SBH}, V_0 and V_{bias} are the Schottky barrier height, the built-in potential and the piezo-potential at the interphase of heterojunction, respectively. e represents the electronic charge. E_0, E_F, E_C and E_V are the vacuum energy level, the Fermi energy, the conduction band and the valence band, respectively. Reproduced from [169], with the permission of Elsevier.

Piezocatalytic composite films can be easily processed *via* solution casting method. For example, the solution casted Ag@LiNbO$_3$/PVDF composite films showed highly active behaviors of degrading organic dyes and pharmaceuticals and bacterial disinfection (Fig. 25a-b) [174]. Similarly, PVDF-based composites embedded with MoS$_2$ nanoflower also showed piezocatalytic activity of dye degradation in the dark (Fig. 25c-f).[175]

Apart from films, porous foam piezocatalyst of BaTiO$_3$–polydimethylsiloxane (PDMS) was developed by Qian *et al.* [176] The fabrication procedure is illustrated in Fig. 26a, where BaTiO$_3$ and PDMS were solution mixed, and the PDMS foam was prepared *via* the dissolution of pre-existed granulated sugar (Fig. 26a and 26b). The formation of PDMS foam exhibited high surface area, which enhances the adsorption capacity of BaTiO$_3$ nanoparticles and further contributes to an enhanced catalytic performance (Fig. 26c to 26f). The optimized BaTiO$_3$-PDMS composite catalyst can effectively degrade RhB dye solution (efficiency: ~ 94%). Similarly, Shi *et al.* [107] prepared PVDF-BaTiO$_3$ foams through casting sacrificial Ni framework (Fig. 26g). The as-prepared composite foams showed excellent piezocatalytic performance of degrading organic dyes, which is mainly ascribed to the mutual effect of piezocatalytic components, large surface area and stress concentration due to the interconnected pores of foams (Fig. 26h-m).

6. Applications

6.1. Environmental remediation

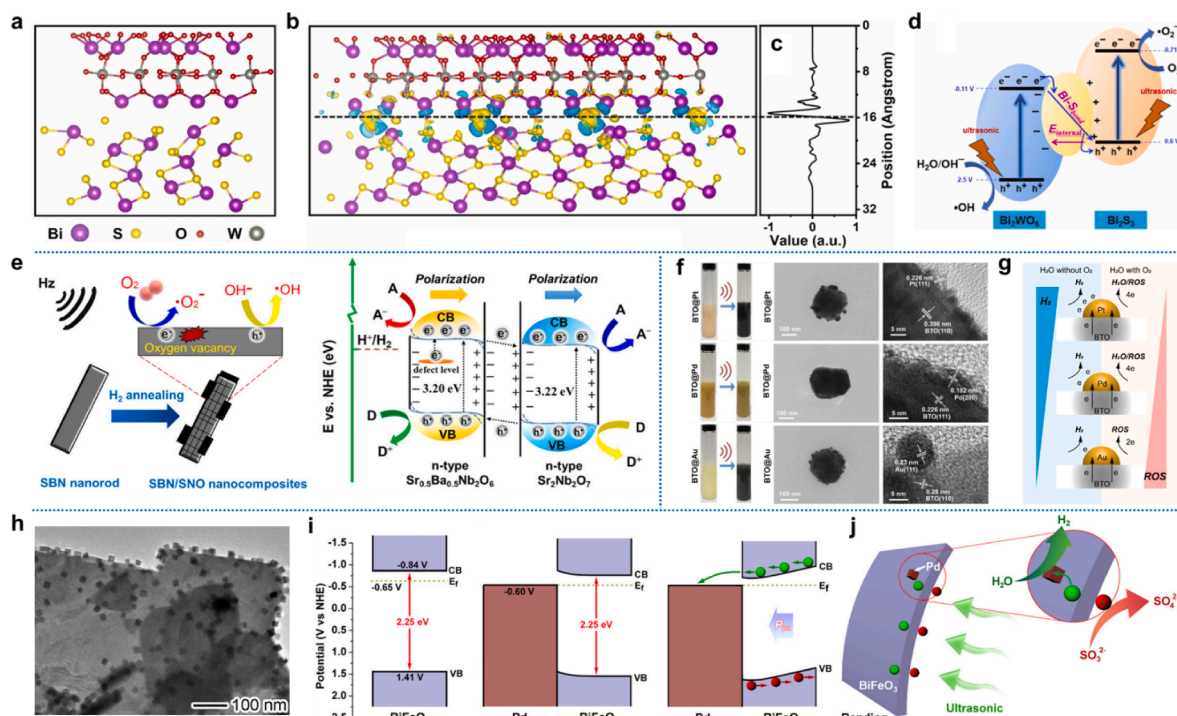ROS, including ·OH, ·O$_2^-$, ^{1}O$_2$ and H$_2$O$_2$, are important highly active chemicals derived from O$_2$. The efficient and controllable

Fig. 24. Bi$_2$S$_3$-Bi$_2$WO$_6$ heterostructure (reproduced from [170], with the permission of Elsevier): (a) the optimized structure; (b) the density functional theory (DFT) calculations of the charge density difference with an *iso*-surface value of 0.003 e Å^{-1}, showing the accumulation (yellow region) and consumption (blue region) of electrons at the interphase between Bi$_2$S$_3$ and Bi$_2$WO$_6$; (c) the planar averaged charge density difference along z-axis and (d) the proposed piezocatalytic mechanism. (e) The schematic diagram of the piezocatalytic mechanism in Sr$_{0.5}$Ba$_{0.5}$Nb$_2$O$_6$-Sr$_2$Nb$_2$O$_7$ heterostructure (reproduced from [171], with the permission of American Chemical Society). BaTiO$_3$@metal heterostructures (reproduced from[173], with the permission of Wiley): (f) the photographs of BaTiO$_3$ (BTO) and metal (M = Pt, Pd and Au) ion mixtures (left) and BTO@M heterostructures (right) after the process of metal deposition, as well as the bright field TEM and HRTEM images of BTO@M heterostructures; (g) a schematic diagram of illustrating the regulation behavior of electrons at the interphase of BTO@M heterostructures during piezocatalysis in water with/without the dissolved oxygen. BiFeO$_3$/Pd heterostructure (reproduced from [172], with the permission of American Chemical Society): (h) TEM image; (i) the energy bands of BiFeO$_3$ and the band alignment in BiFeO$_3$/Pd in the absence/presence of ultrasonic vibration and (j) a schematic diagram of the mechanism of piezocatalyzing H$_2$ evolution of BiFeO$_3$/Pd heterostructure. (For interpretation of the references to color in this figure legend, the reader is referred to the web version of this article.)

generation of ROS is highly crucial in environmental field. Piezocatalysis has been emerged as a novel method to produce ROS, where mechanical vibration (either low-frequency or high-frequency ultrasound waves) can induce polarization as well as the built-in electric field that facilitates the separation of electrons and holes and further redox reactions with H$_2$O or O$_2$.

6.1.1. Dye degradation

Organic dyes are widely existed in industrial wastewater, which lead to severe environmental contamination. The types of dye are estimated to be over than 10,000 [177], and dye wastewater contains non-biodegradable and poisonous pigments which are detrimental to living organisms. Consequently, it is indispensable and challenging to eliminate dyes from aqueous solution. AOP is one of the most effective technologies to remove organic dyes in wastewater. In the process of dye degradation *via* AOP, ROS can destroy the molecular structure of organic dyes through redox reactions. The evolution of ROS such as ·OH and ·O$_2^-$ requires the fit of the band positions with redox potentials (·OH/OH$^-$: 2.10 eV and O$_2$/·O$_2^-$: −0.33 eV vs. NHE at pH = 7) [178,179]. Piezoelectrically induced potential acts as either long-range electric field or driving force to relocate the interfacial charge carriers, which contributes to the band bending with adjustable energetics of redox reaction, thereby triggering and/or enhancing the generation of ROS and further accelerating the reaction process of dye degradation.

Liu *et al.* synthesized BaTiO$_3$ with three different nanostructures of nanocubes (NCs), nanoparticles (NPs) and nanofibers (NFs) using hydrothermal synthesis, sol–gel calcination and electrospinning, respectively (Fig. 27a-e).[180] BaTiO$_3$ NFs exhibit more enhanced performance of piezocatalytic dye degradation compared to NCs and NPs, which is largely attributed to the intrinsic merits of nanofibers such as large specific surface area and ease of response to mechanical deformation (Fig. 27f-h). The dye degradation is attributed to the formation of ·OH and ·O$_2^-$ radicals during ultrasonic vibration, as verified using electron spin resonance (Fig. 27i-k). The performance of dye degradation of recently reported piezocatalysts is summarized in Table 4. The working mechanism of degrading dyes using piezoelectric materials can be roughly described as follows [180,181]:
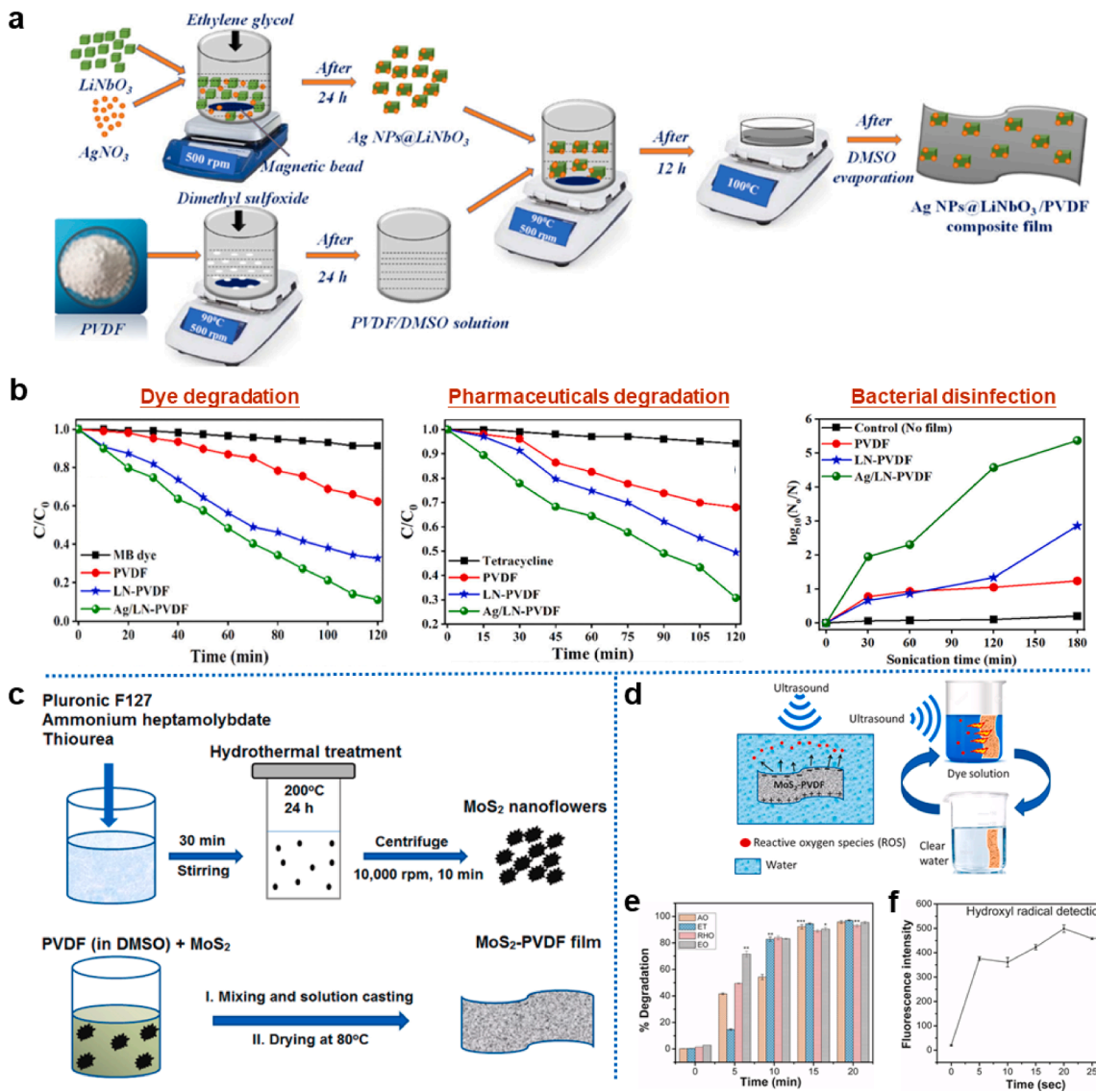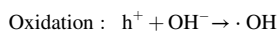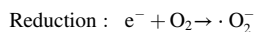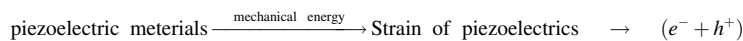
Fig. 25. Ag@LiNbO$_3$/PVDF composite films (reproduced from [174], with the permission of American Chemical Society): (a) fabrication process and (b) piezocatalytic performance of dye/pharmaceuticals and bacteria inactivation. MoS$_2$-PVDF composite films (reproduced from [175], with the permission of Nano Energy): (c) preparation route, (d) piezocatalytic mechanism, (e) degradation of different types of dyes and (f) evolution of hydroxyl radicals under ultrasonic bath vibration.

$$\text{piezoelectric materials} \xrightarrow{\text{mechanical energy}} \text{Strain of piezoelectrics} \rightarrow (e^- + h^+)$$

$$\text{Reduction}: \ e^- + O_2 \rightarrow \cdot O_2^-$$

$$\text{Oxidation}: \ h^+ + OH^- \rightarrow \cdot OH$$

$$\cdot OH (\text{or} \ \cdot O_2^-) + \text{Dye} \rightarrow \text{degradation}$$

6.1.2. Antibiotics degradation

Apart from dyes, antibiotics are another type of ubiquitous contaminants resulting in hazards to ecosystem and human health such as the disturbance of natural bacterial communities, the increase of birth defects and multiple organ injuries. Like dye degradation, ROS plays a decisive role in degrading antibiotics. For example, 3D flower-like Fe@MoS$_2$ powders prepared *via* mechanochemical ball-milling showed excellent degradation of tetracycline as verified using the three-dimensional excitation-emission matrix fluorescence spectra (Fig. 28). The responsible reaction for degrading tetracycline involves the processes of demethylation, ring-opening,
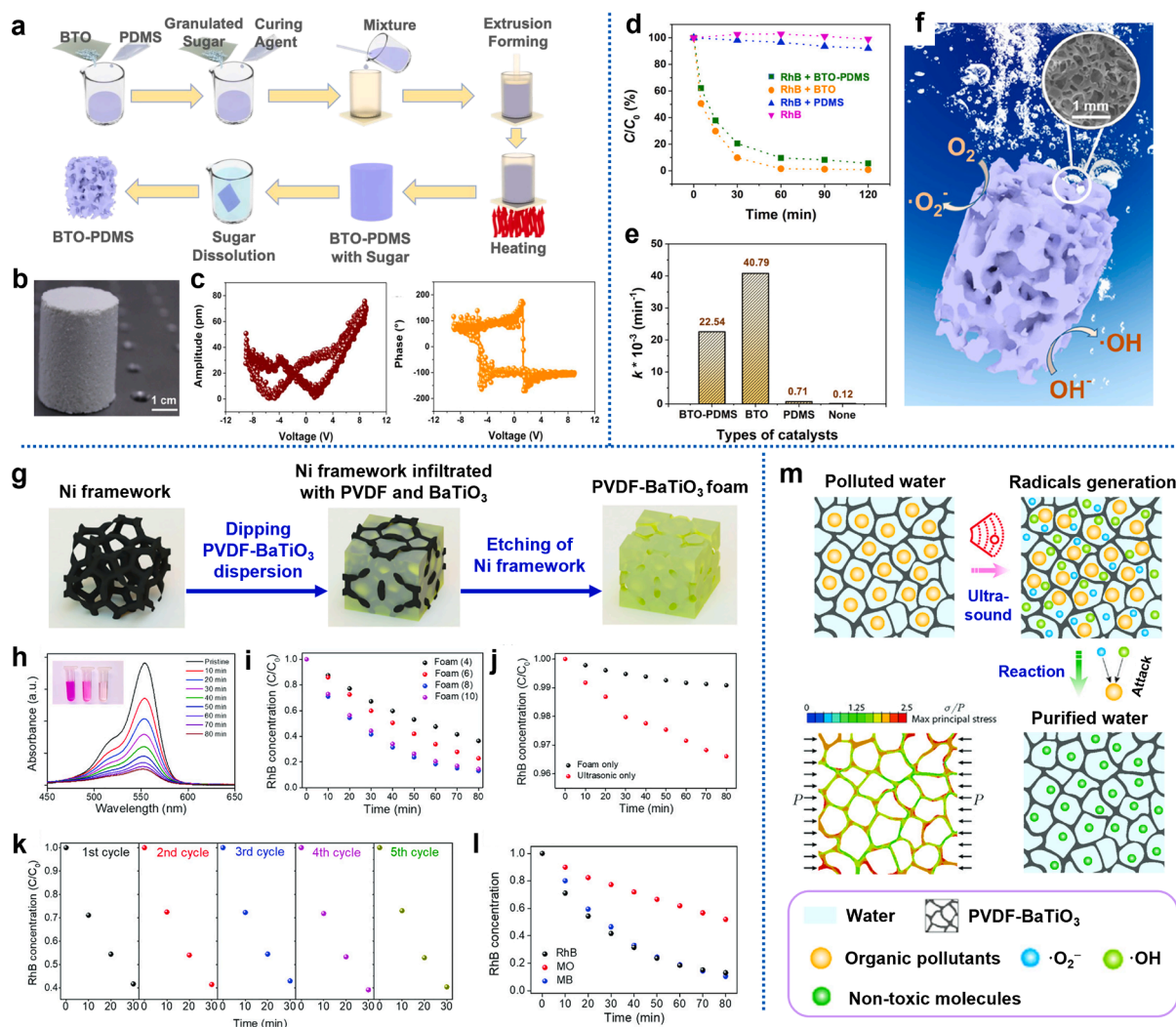
Fig. 26. Preparation and piezocatalytic performance of BaTiO₃-PDMS porous foams (reproduced from [176], with the permission of American Chemical Society): (a) fabrication process; (b) image of cylindrical BaTiO₃-PDMS catalyst; (c) PFM characterization of BaTiO₃ (left: amplitude, right: phase); (d) piezo-catalytic performance of degrading RhB solution using different catalysts; (e) kinetic rate constant of RhB degradation using different catalysts and (f) schematic illustration of piezo-catalytic process. Preparation and piezocatalytic performance of PVDF-BaTiO₃ foams (reproduced from [107], with the permission of Wiley): (g) schematic illustration of preparation process; (h) the UV–vis absorption of RhB aqueous solution during piezocatalysis (inset: image of RhB solution); (i) the piezocatalytic comparison of different PVDF-BaTiO₃ foams; (j) the RhB degradation without foam or ultrasonic irradiation; (k) the cycling performance; (l) piezocatalytic comparison of degrading different dyes (RhB: rhodamine B, MO: methyl orange and MB: methylene blue); (m) schematic illustration of the piezocatalytic degradation process of pollutants along with the stress distribution based on finite element analysis. (For interpretation of the references to color in this figure legend, the reader is referred to the web version of this article.)

decarboxylation and dihydroxylation, which leads to the consequent formation of CO_2, H_2O and compounds with smaller molecules. The highly piezo-active nature is attributed to the few-layered structure and semi-metallic characteristic, and ·OH and $^1O_2$ radicals were the responsible active sites for the process of tetracycline degradation.[189] The recently reported work of antibiotics degradation using piezocatalysts is summarized in Table 5.

6.1.3. Piezo-assisted Fenton-like process

The classic Fenton reaction generally refers to the reaction process of the decomposition of H_2O_2 into strongly oxidizing ·OH in the presence of ferrous ions (Fe^{2+}). The discovery of the Fenton reaction originated in the late 19th century, when the British chemist H. J. Fenton found that the acidic solution mixed of Fe^{2+} and H_2O_2 led to the oxidation of tartaric acid.[192] To commemorate this discovery, the mixed solution of Fe^{2+} and H_2O_2 are referred to as 'Fenton's reagent'. Due to the simple raw materials and useful properties, Fenton's reagents soon expanded to the field of organic chemistry and were widely used in organic analysis and synthesis. In 1964, H. R. Eisenhauer used Fenton's reagent in the purification of wastewater containing organic substances such as phenol for the
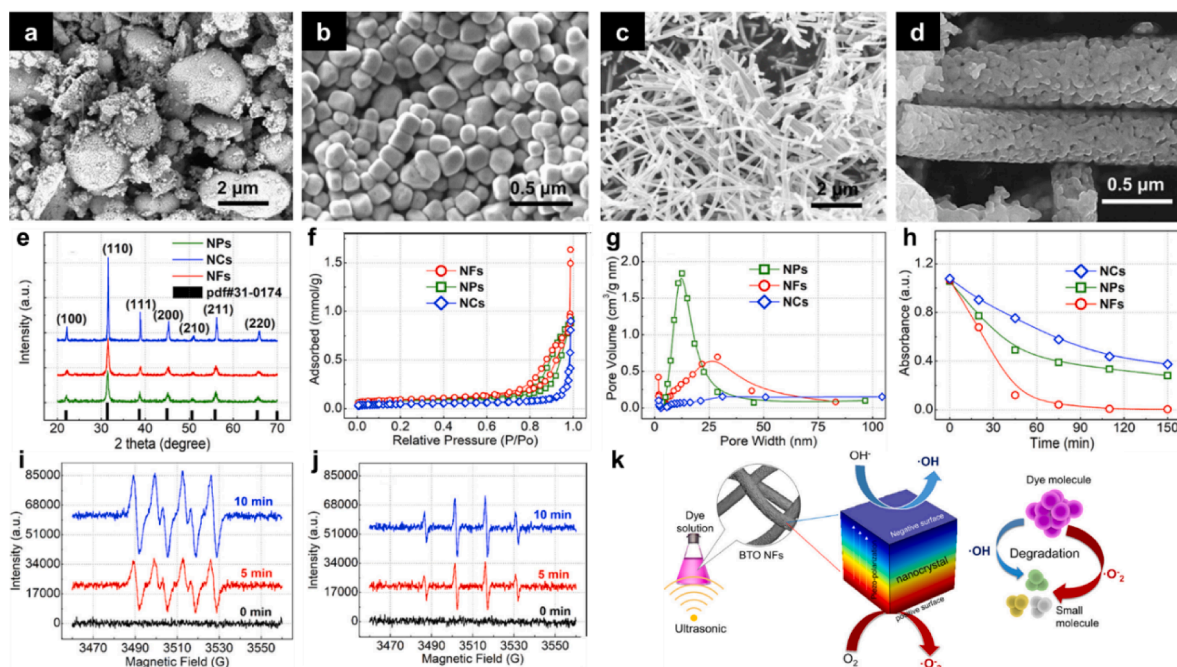
Fig. 27. SEM image of BaTiO$_3$: (a) NCs, (b) NPs, (c) and (d) NFs. (e) XRD patterns, (f) BET isotherms, (g) pore size distributions and (h) piezo-catalytic Rhodamine B degradation curves of three BaTiO$_3$ nanostructures. ESR detection of (i) $\cdot O_2^-$ and (j) $\cdot$OH of BaTiO$_3$ NFs. (k) Schematic diagram of the underlying mechanism responsible for the piezocatalytic degradation using BaTiO$_3$ NFs. Reproduced from [180], with the permission of American Chemical Society.

Table 4
A brief summary of dye degradation of recently reported piezocatalysts.

Materials	Processing	ROS	Dye degradation efficiency (%)	Ultrasonic condition	Ref
Ba$_{0.8}$Sr$_{0.2}$TiO$_3$, nanowires	Template hydrothermal method	$\cdot$OH, $\cdot O_2^-$	MO, ~99–100	80 W,40 kHz; 120 min	[182]
Co/MoS$_2$, nanosheets	Co doped	e^-, $\cdot O_2^-$	MB, ~99–100	40 kHz,100 W; 300 s	[183]
NaNbO$_3$, nanowires	hydrothermal method	$\cdot$OH	RhB, ~ 80	40 kHz; 120 min	[184]
ZnSO$_3$, nanoparticles	solution-based colloidal methods	$\cdot$OH	RhB, ~ 99–100	33 kHz,120 W; 150 min	[185]
BaTiO$_3$, nanofibers	Electrospinning	$\cdot$OH	RhB, ~ 99–100	100 W; 150 min	[180]
ZnO, nanorods	solid-state method	$\cdot$OH, $\cdot O_2^-$	MB, ~ 99–100	40 kHz,150 W; 5.5 h	[186]
Ag/PbBiO$_2$I; nanosheets	Ag doped& hydrothermal method	$\cdot O_2^-$, holes, $\cdot$OH	RhB, ~ 80	40 kHz, 120 W; 90 min	[187]
MoO$_x$ /ZnS/ZnO ternary complex	one-step method	holes, $\cdot O_2^-$	RhB, ~99	40 kHz,120 W; 90 min	[188]

first time,[193] which created a precedent for the application of Fenton's reagent in the field of sewage treatment. Even today, Fenton's reagent is a classic sewage treatment reagent, widely used in the field of environmental science.

To achieve the best performance in the organics' degradation, numerous efforts have been made to improve the efficiency of Fenton reaction. The dosage of reagents (H$_2$O$_2$ and Fe^{2+}) is a consideration in enhancing the efficiency of the yield of $\cdot$OH. In recent years, piezocatalysis has been applied to facilitate Fenton reaction in terms of *in-situ* generation of H$_2$O$_2$ to promote the additional yield of free radicals.[194] Lv *et al.* reported that the degradation of acid orange 7 (24.3%), phenol (16.9%) and 4-chlorophenol (7.8%) in the 30 min BaTiO$_3$-mediated piezocatalysis with the addition of Fe^{2+} ions,[195] which was attributed to the additional generation of $\cdot$OH by the Fenton reaction of Fe^{2+}, and *in-situ* generated H$_2$O$_2$ (5.3 μmol/L) by piezocatalysis.

Compared with homogenous Fenton reactions involving free Fe^{2+} ions, heterogeneous Fenton systems have attracted increasing attention to avoid the drawback of traditional Fenton reactions, such as poor recyclability and limited pH working range. In the process of heterogeneous Fenton reactions, iron exists stably in the catalysts and the precipitation of iron hydroxide does not occur with the generation of $\cdot$OH. Wei *et al.* designed and prepared Fe-loaded BiVO$_4$ (Fe/BVO) for the enhanced degradation of p-chlorophenol (Fig. 29a).[196] The kinetic rate constants (*k*) for BVO and Fe/BVO were 0.005 min^{-1} and 0.016 min^{-1}, respectively. This indicates
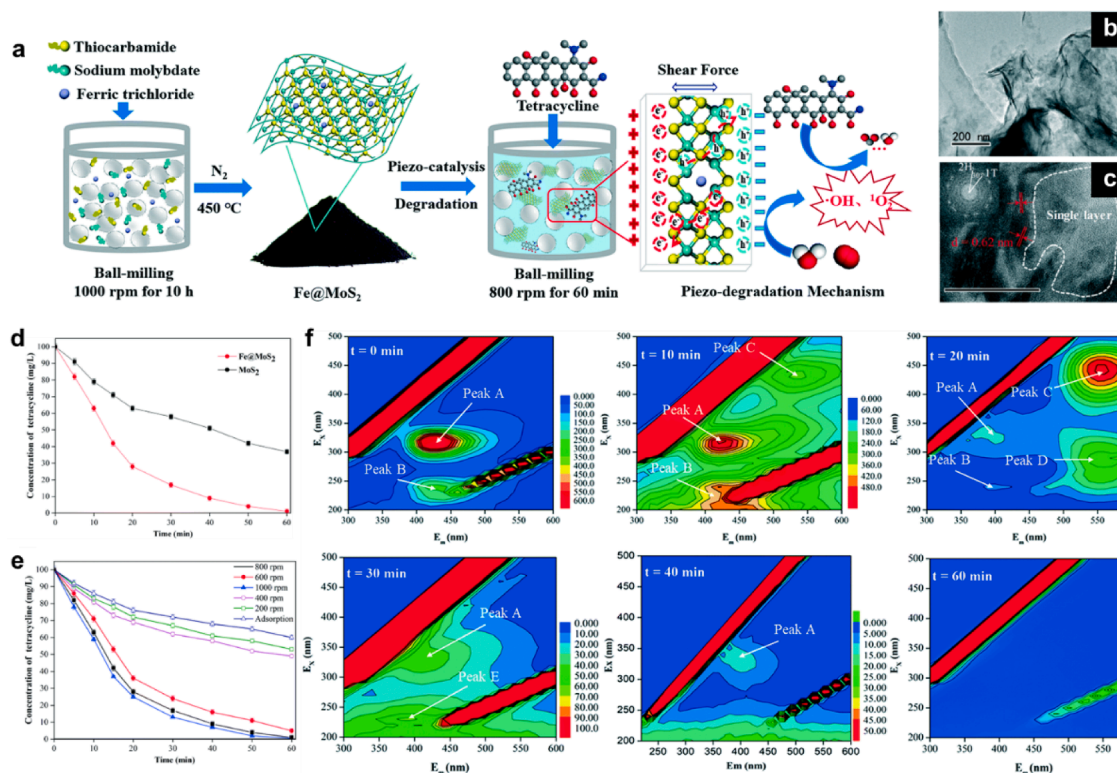
Fig. 28. (a) The fabrication route of Fe@MoS$_2$ powders; (b) SEM and (c) HRTEM images of Fe@MoS$_2$ powders; (d) and (e) the enhanced piezo-catalytic activity of Fe@MoS$_2$ for degrading tetracycline; (f) the three-dimensional excitation-emission matrix fluorescence spectra of tetracycline aqueous solution after degradation using Fe@MoS$_2$ for different time. Reproduced from [189], with the permission of Royal Society of Chemistry.
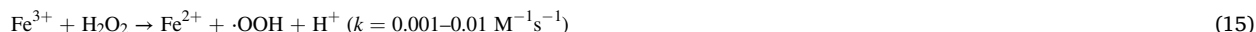
Table 5
A brief summary of antibiotics degradation performance of recently reported piezocatalysts.

Materials	Processing	ROS	Antibiotics degradation efficiency (%)	Degradation condition	Ref
3D flower-like Fe@MoS$_2$, powders	Ball-milling and calcination	·OH, $^1O_2$	tetracycline, ~99–100	Ball-milling at 800 rpm; 60 min	[189]
Bi$_4$Ti$_3$O$_{12}$, nanosheets	Hydrothermal method	·OH	tetracycline hydrochloride, ~70–80	Ultrasonication at 40 kHz,180 W; 300 s	[147]
SnO$_2$-Sb/t-BaTiO$_3$, nanoparticles	Hydrothermal method	·OH, $^1O_2$, ·O$_2^-$	metronidazole, ~ 70–80	Ultrasonication at 40 kHz, 110 W 60 min	[190]
Graphene-doped MoS$_2$, nanoparticles	Ball-milling and calcination	·OH	tetracycline, ~ 92	Ball-milling at 800 rpm; 60 min	[191]
MoS$_2$, WS$_2$, and WSe$_2$, nanosheets	Electrospinning	·OH and ·O$_2^-$	tetracycline, ~60–95	Ultrasonication at 40 kHz,110 W; 120 min	[180]

that Fe loading enhanced the degradation rate of p-chlorophenol, being more than three times compared to pure BVO (Fig. 29b). Apart from the increased H$_2$O$_2$ generated by the reduction of oxygen in piezocatalysis, H$_2$O$_2$ was involved in the transition cycle of Fe(II)/Fe(III) to produce ·OH, which realized the integration of heterogeneous piezo-Fenton catalyst.

The reaction between the heterogeneous Fenton catalyst and H$_2$O$_2$ not only includes the reaction of iron ions leaked from the catalyst with H$_2$O$_2$ (Equation 14 and 15), but also includes the iron element (valence state + 3) on the surface of the material reacting with H$_2$O$_2$ (Equation 16 and 17).

$$Fe^{2+} + H_2O_2 \rightarrow Fe^{3+} + \cdot OH + OH^- \ (k = 40\text{–}80 \ M^{-1}s^{-1}) \tag{14}$$

$$Fe^{3+} + H_2O_2 \rightarrow Fe^{2+} + \cdot OOH + H^+ \ (k = 0.001\text{–}0.01 \ M^{-1}s^{-1}) \tag{15}$$

$$\equiv Fe(III) + H_2O_2 \rightarrow \equiv Fe(II) + \cdot OOH + H+ \tag{16}$$

$$\equiv Fe(II) + H_2O_2 \rightarrow \equiv Fe(III) + \cdot OH + OH^- \tag{17}$$
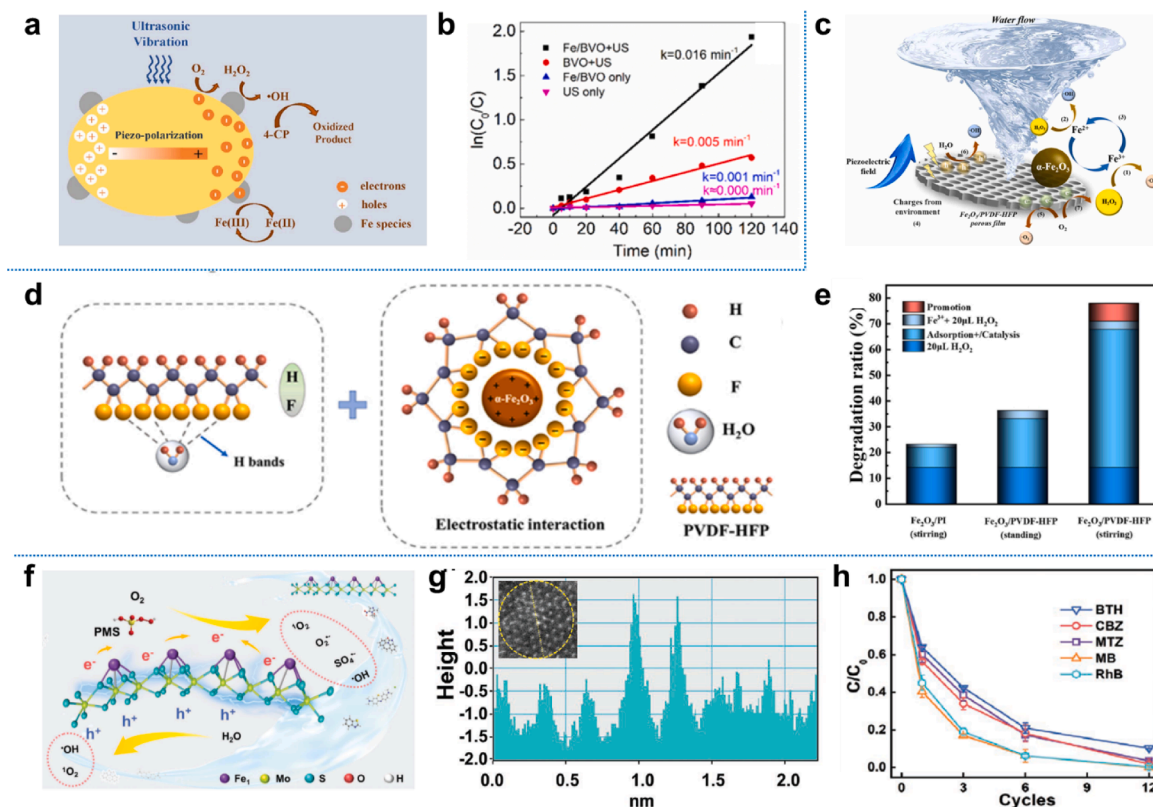
Fig. 29. Piezo-assisted Fenton process of Fe/BVO (reproduced from [196], with the permission of Elsevier): (a) schematic illustration of the piezo-assisted Fenton degradation of p-chlorophenol; (b) the first-order kinetics constant rate of p-chlorophenol degradation under different conditions. Piezo-assisted Fenton catalyst of α-Fe$_2$O$_3$/PVDF-HFP porous film (reproduced from [197], with the permission of Elsevier): (c) schematic diagram of mechanism; (d) the schematic illustration of the interaction of hydrogen bond and electrostatic force between α-Fe$_2$O$_3$ NPs and PVDF-HFP molecules and (e) the degradation ratio of tetracycline of the Fe$_2$O$_3$/polyimide (PI) and Fe$_2$O$_3$/PVDF-HFP porous films under different conditions. Fe$_1$-MoS$_2$ for water purification (reproduced from [198], with the permission of Wiley): (f) the schematic illustration of piezo-activated PMS for water purification; (g) the HAADF-STEM image of Fe$_1$-MoS$_2$ and (h) the comparison of degradation efficiencies of different organic pollutants.

Therefore, an analogy to homogeneous Fenton reaction, the redox cycle between Fe(II) and Fe(III) is the rate-limiting step of restricting the efficiency of heterogeneous Fenton reaction. In terms of enhancing Fenton reactivity, the introduction of piezo-induced electric field not only favors the *in-situ* yield of H$_2$O$_2$, but also accelerates the transition of the Fe(III)/Fe(II) cycle. Chai *et al.* prepared a novel composite based on piezoelectric polymer, P(VDF-HFP) with α-Fe$_2$O$_3$ nanoparticles as fillers to further improve the catalysis performance (Fig. 29c).[197] The introduction of α-Fe$_2$O$_3$ nanoparticles not only enhanced the piezoresponse of P(VDF-HFP) by the increase of β-phase duo the hydrogen bonding and electrostatic interactions between the P(VDF-HFP) matrix and the α-Fe$_2$O$_3$ nanoparticles (Fig. 29d). It also provides the active sites for Fe(III) to react with the *in-situ* generated H$_2$O$_2$, leading to an enhanced degradation performance driven by water flow, a much gentler force compared to the commonly used ultrasound. For the Fe$_2$O$_3$/P (VDF-HFP) film with stirring, the degradation ratio of tetracycline was up to 77.9%, of which 53.7% was attributed to the combination of piezocatalysis and Fenton reaction of the α-Fe$_2$O$_3$/P(VDF-HFP) film itself. Considering the removal rate of tetracycline by H$_2$O$_2$ (14.1%) and the Fenton reaction with additional H$_2$O$_2$ (3.2%), the Fenton reaction solely enhanced by the electric field was calculated to be 6.9%, which was attributed to the field-induced acceleration of Fe^{3+}/Fe^{2+} cycle (Fig. 29e).

The application of piezocatalysis has been extended to promote Fenton-like reactions based on peroxymonosulfate (PMS). Lan *et al.* designed and fabricated MoS$_2$ nanosheets with Fe single atomic sites (Fe$_1$-MoS$_2$) (Fig. 29f).[198] The single atomic sites of Fe was observed in sub-angstrom resolution high-angle annular dark field scanning TEM (HAADF-STEM) images (Fig. 29g). With the mechanical stimuli provided by water flow, Fe$_1$-MoS$_2$ exhibited prominent performance on the degradation of different kinds of contaminants, including industrial chemicals (butylated hydroxytoluene), antibiotics (metronidazole, carbamazepine), and dyes (RhB, MB) (Fig. 29h). With the application Fe$_1$-MoS$_2$, <20% of each pollutant remained after 12 water flow cycles. The piezo-assisted PMS-oxidation process involved various types of ROS, including ·OH, SO$_4^{\cdot-}$, O$_2^{\cdot-}$, and ^{1}O$_2$ based on the EPR analysis. The Fe single atom played triple roles in enhancing the overall catalytic performance analyzed using the theoretical calculation results: (i) Fe atomic sites increased the asymmetry of the MoS$_2$ structure, thus improving the piezo-response; (ii) Fe atomic sites acted as the electron acceptor to further promote the charge separation on the surface of MoS$_2$; (iii) the Fe atomic sites were Fenton-active sites which utilized the electrons in the Fe(III)/Fe(II) transition cycle to activate PMS in additional ROS generation. This work not only deepens the

understanding of the synergistic effect of piezocatalysis and Fenton-like reactions, but also highlights the role of single atom sites play in enhancing piezocatalytic performance.

6.2. Renewable energy production

The severe energy crisis urges the development of renewable energy. The capability of converting mechanical energy to electric energy endows piezoelectric materials with great potentiality of harvesting kinetic energy. More recently, piezocatalysis has underwent a surge in renewable energy production *via* converting mechanical energy to chemical energy under the applied external mechanical vibration, which perfectly remedies the deficiency of poor photocatalytic activity arising from incompatible energy band structure and the recombination of photogenerated charge carriers.

6.2.1. Hydrogen production

Hydrogen energy, a new energy with zero-carbon emissions and high heat of combustion (about 286 kJ mol^{-1}), has always been regarded as promising alternative to fossil energy. The application fields of hydrogen energy include but not limited to transportation, construction and manufacturing industry. Various methods have been adopted to produce hydrogen energy, among which photocatalytic water splitting is termed as the most straightforward and sustainable way due to the sole utilization of semiconductors and light irradiation. The overall water splitting involves the production of H_2 and O_2 (Equation 18 and 19). Piezoelectric semiconductors such as $BaTiO_3$ nanoparticles [130,131], $Bi_{0.5}Na_{0.5}TiO_3$ particles [199], ZnO microfibers [200], vanadium (V)-doped $NaNbO_3$ (V-
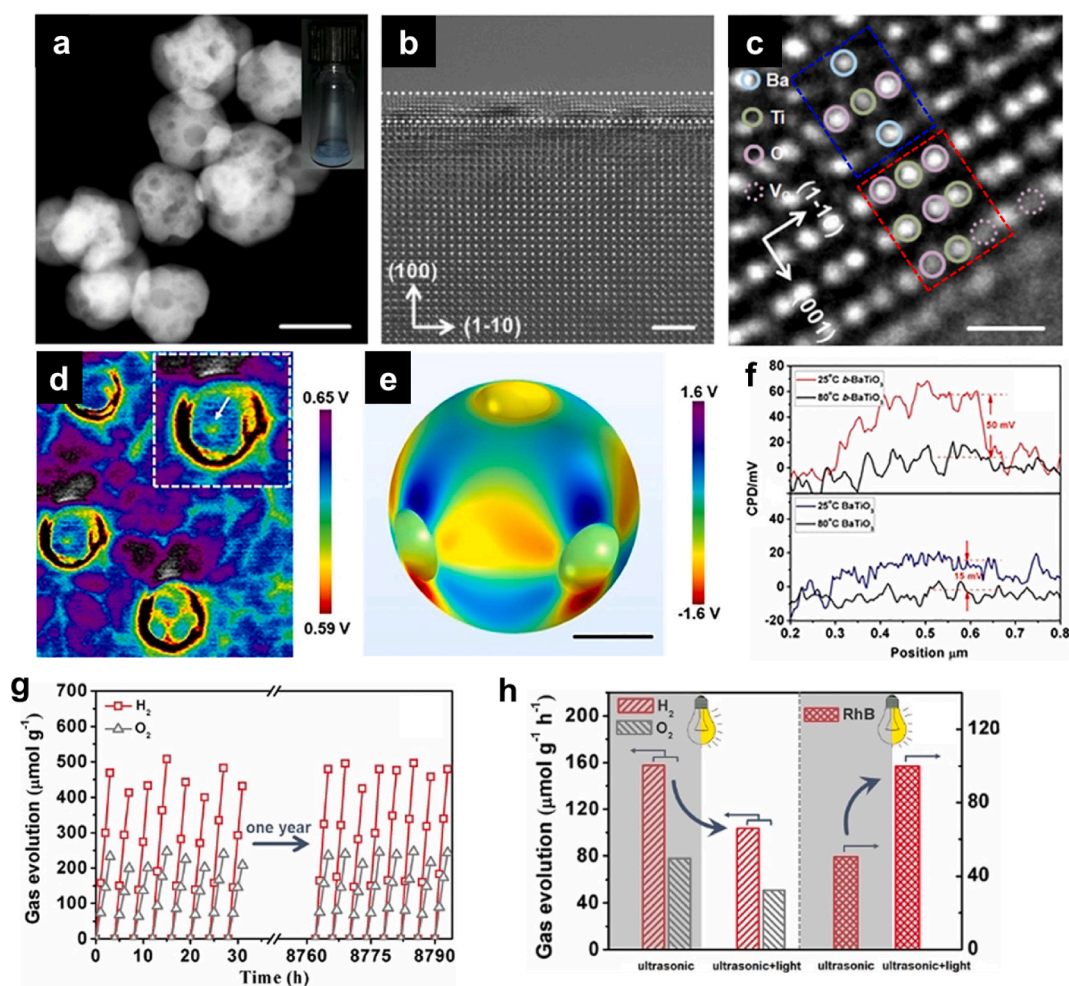
Fig. 30. (a) TEM image, (b) Cross-section HRTEM image and (c) AFM topographic image of porous $BaTiO_3$ powders (scale bar: 200 nm). (d) Kelvin probe force microscopy (KPFM) phase image of porous $BaTiO_3$ powders. (e) The distribution of potential in a *b*-$BaTiO_3$ nanoparticle based on COMSOL simulation. (f) Comparison of surface potential for the pristine and mesoporous $BaTiO_3$ nanoparticles at different temperatures. (g) The recycling piezocatalytic H_2 and O_2 evolution tests of porous $BaTiO_3$ powders under an ultrasonic vibration of 40 kHz. (h) A comparison of water splitting and dye degradation activities of porous $BaTiO_3$ particles under the treatment of ultrasonication with/without illumination. Reproduced from [131], with the permission of Wiley.

NaNbO$_3$) nanocubes [201] and C-doped KNbO$_3$ single crystals [202] have been designed for efficient hydrogen production.

$$4H^+ + 4e^- \rightarrow 2H_2 \text{ (reduction)} \tag{18}$$

$$2H_2O + 4 h^+ \rightarrow 4H^+ + O_2 \text{ (oxidation)} \tag{19}$$

Mesoporous BaTiO$_3$ nanoparticles (*b*-BaTiO$_3$) with heteroepitaxial strain were fabricated *via* the pH control and high-temperature etching of NaBH$_4$,[131] which consists of alternate planes of BaO and TiO$_2$. The mesoporous structure originates from the dissolve of BaO planes in acidic condition, and BaTiO$_3$ particles were covered with an inhomogeneous layer (Fig. 30a-b) due to the etching and reduction of NaBH$_4$. The atomic locations of Ba, Ti and O were determined using the spherical aberration-correct TEM (Fig. 30c), which clearly shows the typical perovskite structure of BaTiO$_3$ and surface reconstruction of TiO$_x$, as highlighted using the blue and red rectangular dashed line in Fig. 30c, respectively. *b*-BaTiO$_3$ particles showed localized distribution of electric potential around pores that was simulated to be as high as 1.6 V according to the finite element method (Fig. 30d-e). Moreover, free charges can be eliminated from the surface of BaTiO$_3$ particles at high temperature such as 80 °C (Fig. 30f). All of these results confirm an enhanced ferroelectric polarization *via* strain engineering. The generated electric potential (1.6 V) is sufficient to induce overall water splitting (required band gap: 1.23 V), and the piezocatalytic activity maintained well over a long time period with a maximum hydrogen production rate of 159 μmol g^{-1}h^{-1} (Fig. 30g). Anomalously, *b*-BaTiO$_3$ exhibited reduced rates of hydrogen and oxygen evolution under simultaneous ultrasonication and illumination (Fig. 30h), which may be ascribed to the decreased absorption of H$^+$/OH$^-$ induced by the increased separation of photoexcited charge carriers by the internal electric field.

In addition to strain engineering, phase engineering was also employed to enhance the piezocatalytic H$_2$ production. For example, BaTiO$_3$ nanoparticles (average size: 10 nm) with a high electromechanical coefficient were fabricated using hydrothermal method [130], and showed a high piezocatalytic overall water splitting with a H$_2$ production rate of 655 μmol g^{-1}h^{-1}. By producing a BaTiO$_3$ nanofluid, H$_2$ production has been improved to 270 mmol g^{-1}h^{-1} for a loading of 5 mg L^{-1} of BaTiO$_3$ in 10% MeOH/H$_2$O.[203] Increases in piezocatalytic activity stem from the incorporation of more than one phase, at least one phase is non-centrosymmetric, and reducing particle size to increase surface area. The performance of piezocatalytic water splitting is dependent on working temperature. Bowen *et al.* reported that Ba$_x$Sr$_{1-x}$TiO$_3$ pellets showed enhanced piezocatalytic performance with a H$_2$ production rate of 3590 μmol g^{-1}h^{-1} at working temperatures (40–42 °C) just below the Curie point of materials (42 °C), which is mainly ascribed to the great change of polarization within applied stress as the temperature approaching Curie point.[168] Table 6 summarized the recent research works about adopting piezocatalysis for hydrogen production.

6.2.2. Recycling of greenhouse gas

Greenhous gases absorb and reradiate infrared radiant energy emitted by Earth, leading to the greenhouse effect. Carbon dioxide (CO$_2$), methane (CH$_4$) and nitrous oxide (N$_2$O) are three main sources of global warming.

There is a growing need for environment protection, and the economic value of carbon products has motivated the development of CO$_2$ utilization technologies. Various methods including thermocatalytic, photocatalytic and electrocatalytic conversion have been evolved to convert CO$_2$ into useful organic feedstocks and hydrocarbon fuels such as ethanol, ethylene, methane *etc*.[208,209] Among

Table 6
A brief summary of piezocatalysts used in H$_2$ production.

| Materials	Processing	Enhancing strategy	H$_2$ production rate (μmol g^{-1}h^{-1})	Piezocatalytic condition	Ref
Mesoporous BaTiO3 nanoparticles	Hydrothermal and high temperature etching of NaBH$_4$	Strain engineering	~ 159	Ultrasonication at 40 kHz	[131]
10 nm BaTiO$_3$ nanoparticles	Hydrothermal method	Morphotropic phase boundary	~ 655	Ultrasonication at 60 kHz	[130]
Vanadium (V)-doped NaNbO$_3$	Hydrothermal method	Morphology control	~ 346	Ultrasonication at 68 kHz, 192 W	[201]
Glutathione modified acidized-MoS2 nanosheets	Hydrothermal method	Promoting carriers' separation	~ 1250	Ultrasonication at 280 W	[204]
Pd decorated BiFeO$_3$ nanosheets	Hydrothermal method	Cocatalyst Engineering	~ 1140	Ultrasonication at 40 kHz, 100 W	[172]
BiFeO$_3$ square nanosheets	Hydrothermal method	Morphology control	~ 124	Ultrasonication at 45 kHz, 100 W	[111]
Bi$_2$WO$_6$ nanoplates	Hydrothermal method	Morphology control	~ 191	Ultrasonication at 40 kHz	[205]
0.7BiFeO$_3$–0.3BaTiO$_3$ nanoparticles	Hydrothermal method	Band structure engineering	~ 1322	Ultrasonication at 40 kHz, 100 W	[206]
Ni/GaN nanowires	Chemical vapor deposition followed by photo-deposition	Cocatalyst Engineering	~ 88	Ultrasonication at 40 kHz, 110 W	[3]
La$_2$NiO$_4$ nanoplates	Citrate sol–gel followed by calcination	Morphology control	~ 680	Ultrasonication at 40 kHz	[207]
Ba$_x$Sr$_{1-x}$TiO$_3$ pellets	Solid-state reaction	Working at temperature of around Curie point	~ 3590	Ultrasonication at 40 kHz, 60 W	[168]
BaTiO$_3$ powders	Solid-state reaction	Reactor design, nanofluidic suspension	~ 270,000	Pre-shaking followed by ultrasonication at 40 kHz	[203]
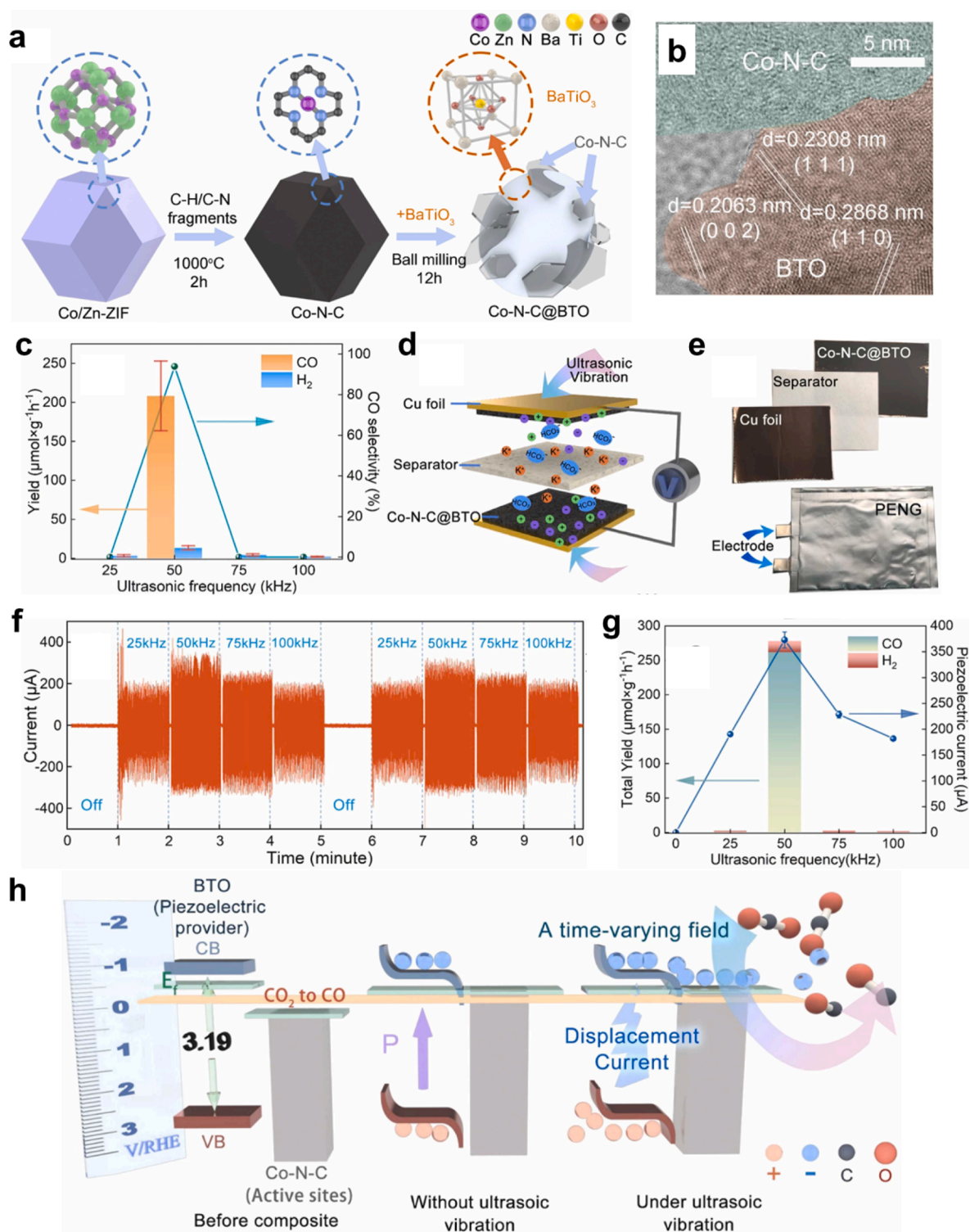
Fig. 31. (a) The synthetic route of Co-N-C@BTO piezocatalysts. (b) The high-resolution TEM of Co-N-C@BTO showing the interface of between Co-N-C and BTO. (c) The production of CO and H_2, and the CO selectivity of Co-N-C@BTO under ultrasonication at different frequencies. (d) The scheme of electrochemical characterization based on piezoelectric nanogenerator. (e) An image of Co-N-C@BTO piezoelectric nanogenerator. (f) The chronoamperometry curve of Co-N-C@BTO piezoelectric nanogenerator. (g) The generated piezoelectric current and total gas production of piezocatalysis of Co-N-C@BTO. (h) The schematic illustration of the mechanism of piezocatalytic CO_2 reduction reaction using Co-N-C@BTO, which involves the energy band structure and piezoelectric current. Reproduced from [211], with the permission of Elsevier.

these methods, piezocatalytic CO_2 reduction reaction exhibits the distinct advantages of mild condition (compared to thermocatalytic conversion), zero usage of sacrificial agents or extra light source (compared to photocatalytic conversion), and utilizing green and competitive mechanical energy (compared to the electric energy of electrocatalytic conversion). Like piezocatalytic H_2 production, the research of piezocatalytic CO_2 reduction reaction mainly focuses on the structural and compositional design of piezocatalysts with the final purpose of achieving pronounced catalytic performance.

Lead-free lithium-doped potassium sodium niobate ($K_{0.5}Na_{0.5})_{0.97}Li_{0.03}NbO_3$ (KNLN) particles were synthesized *via* a solid-state reaction,[210] showing a CO production rate of 438 µmol $g^{-1}h^{-1}$. In addition to modulating piezoelectric properties, designing proper active sites is also critical to enhancing the catalytic performance and the selectivity of products after CO_2 reduction reaction. Co-nitrogen-carbon (Co-N-C) derived from Co/Zn-ZIF was integrated with $BaTiO_3$ (BTO) to fabricate Co-N-C@BTO piezocatalysts (Fig. 31a-b) [211], which showed a high CO selectivity (93.8%) along with a CO production rate of 261.8 µmol $g^{-1}h^{-1}$ only under ultrasonication of 50 kHz (Fig. 31c). The authors proposed that the only CO_2 production at 50 kHz was related to the piezoelectric resonance effect, and proved the assumption *via* measuring the current of Co-N-C@BTO-based piezoelectric nanogenerator (Fig. 31d-f). The generated piezoelectric current showed a similar trend of the CO production as a function of ultrasonication frequency (a maximum value at 50 kHz in Fig. 31g). It is suggested that a time-varying electrostatic potential generates on the surface of pieocatalysts under the principle of piezoelectric nanogenerator. This acts as the driving force to promote the transfer of electrons, and further regulates the energy band structure to trigger the CO_2 reduction reaction (Fig. 31h). More importantly, a high piezocatalytic activity does not necessarily require large external mechanical energy since the piezoelectric material can largely deform under the ultrasonication at frequencies close to resonance frequency. Similar to facilitating the H_2 production of $Ba_xSr_{1-x}TiO_3$ pellets *via* working in the vicinity of Curie point,[168] the niobium-doped lead zirconate titanate (PZTN) powders [167] showed a low Curie temperature (~39 °C) arising from the introduction of Nb, which contributed to a great change of spontaneous polarization in the vicinity of Curie point and a further promising piezo-catalytic CO_2 reduction rate of 789 µmol $g^{-1}h^{-1}$ at a small dosage of PZTN. Further increasing the dosage of PZTN did not promote the catalytic performance due to the agglomeration of particles. Table 7 briefly summarizes the recently reported work of piezocatalytic CO_2 reduction reaction, involving the composition, structure, processing details and catalytic performance of specific piezocatalysts.

Like CO_2 reduction reaction, piezocatalysis has also been utilized to realize CH_4 conversion. Hydroxyapatite ($Ca_{10}(PO_4)_6(OH)_2$, HAp) (piezoelectric coefficient of 1–16 pm V^{-1}) whose ferroelectric nature arising from the alignment of OH^- along [0 0 1] directions has been exploited to promote the activation of CH_4 into small molecules (Fig. 32a).[212] HAp displayed a characteristic butterfly loop of amplitude–voltage, verifying its piezoelectricity (Fig. 32b). The generated current under ultrasonication was observed using transient current response (Fig. 32c), which clearly showed obvious change with/without ultrasonication. The response current showed its maximum under N_2, and decreased after the inlet of O_2 and CH_4, suggesting the activation of O_2 and CH_4 using HAp. CH_4 converted to liquids of methanol, ethanol and 2-proponal, of which the highest production rates were 84.4, 43.2 and 9.6 µmol g^{-1} h^{-1}, respectively (ratio of CH_4:O_2: 1:0.5) (Fig. 32d). HAp also showed a decent piezocatalytic cycling performance (Fig. 32e). The catalytic mechanism was illustrated in Fig. 32f-g. The surface charges of HAp induced by ultrasound acted as the surface cathode/anode to initiate electrochemical reactions, and realized the activation of methane, oxygen, and water molecules. Specifically, the ·OH generated during the redox reactions of oxygen and water molecules could attack the C–H bond of methane and further converted it into a lower alcohol. It should be noted that no by-products like CO_2 or CO was generated during the formation. This study prolonged the reaction path of methane conversion through C–C coupling and alleviated the excessive oxidation of methanol based on piezocatalysis.

6.3. Biomedicine and biotechnology

From the biological perspective, ROS is a class of oxygen-containing active molecules which are continuously produced, transformed and consumed in organisms.[213] Appropriate ROS level plays a key role in maintaining the normal physiological function of cells.[214] The role of ROS in cells is like a double-edged sword. Low levels of ROS regulate cell proliferation and apoptosis with their fundamental function in metabolism.[215] Once ROS is over-generated, the redox homeostasis will be broken and the continuously accumulated ROS will result in oxidative stress in cells, which causes irreversible oxidative damage to the components of cells, such as DNA, proteins and lipids, thus leading to cell apoptosis or necrosis.[216] Therefore, piezocatalysis can be applied to various biomedical domains, such as tumor treatment, bacteria killing, tissue regeneration, Alzheimer's disease treatment and tooth whitening.

Table 7
A brief summary of piezocatalysts used in CO_2 reduction.

Materials	Processing	Enhancing strategy	CO production rate (µmol $g^{-1}h^{-1}$)	Piezocatalytic condition	Ref
Co-N-C@$BaTiO_3$ particles	Ball milling	Active sites engineering	~ 261.8	Ultrasonication at 50 kHz	[211]
Lithium-doped potassium sodium niobate particulates	Solid-state reaction	Lattice distortion	~ 438	Ultrasonication at 40 kHz	[210]
Nb-doped lead zirconate titanate particulates	Solid-state reaction	Curie temperature engineering	~ 789	Ultrasonication at 40 kHz	[167]

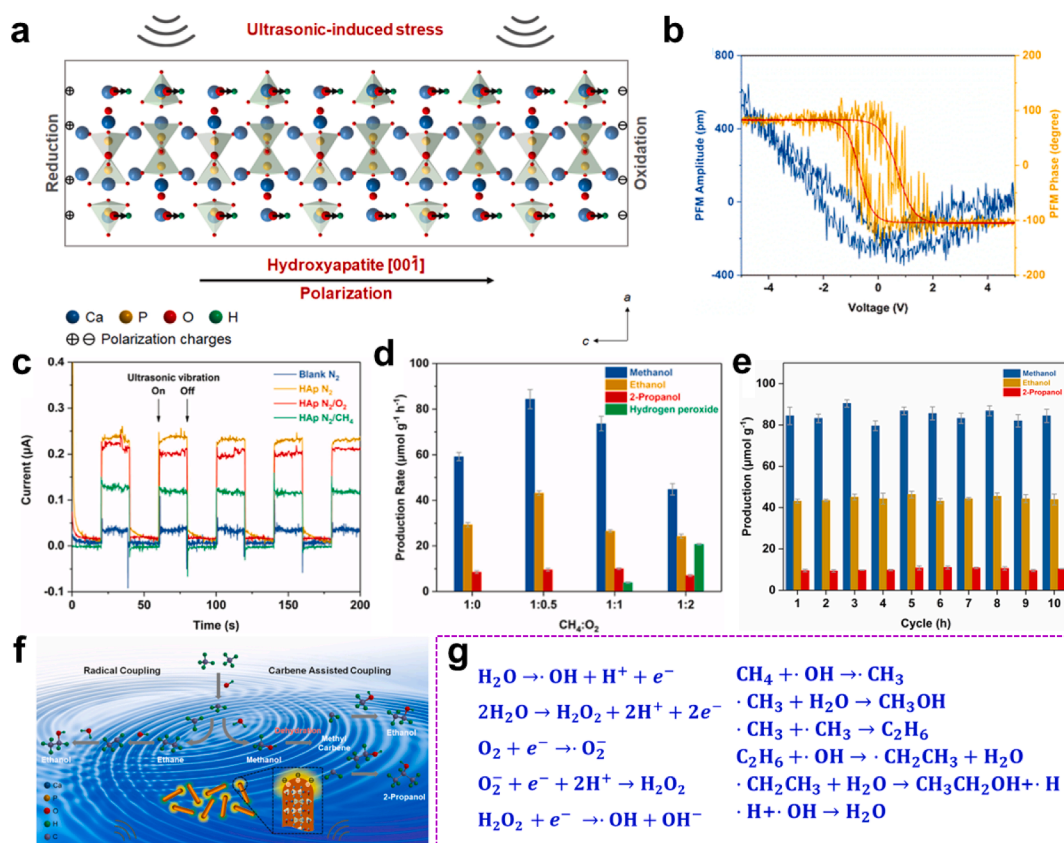**Fig. 32.** Piezocatalytic methane conversion using hydroxyapatite ($Ca_{10}(PO_4)_6(OH)_2$, HAp): (a) the structure and piezoelectric effect of HAp; (b) the PFM hysteresis loops of HAp; (c) the response of transient current of HAp under different atmosphere; (d) the liquid production of piezocatalytic methane conversion of HAp in different ratios of methane/O_2; (e) cycling tests of methane conversion catalyzed by HAp; (f) the schematic description of piezocatalytic methane conversion over HAp; (g) the mechanism of methane conversion to alcohol. Reproduced from [212], with the permission of Elsevier.

6.3.1. Tumor treatment

Compared with normal cells, tumor cells possess elevated ROS levels, which make them more vulnerable to a further increase of ROS.[217] For the last few decades, increasing ROS level beyond the antioxidant capacity of cancer cell has emerged and developed as an effective method of selectively killing tumor cells (Fig. 33a).[218] This is the principle of dynamic therapies relying on the *in-situ* yield of ROS in the tumor area. Among the currently developed dynamic therapies, it is necessary to combine with external physical fields (e.g. laser, ultrasound and radiation), or intrinsic chemical energy (e.g. overexpressed H_2O_2) for activation.[219] Therefore, based on the types of utilized energy, the mainstream dynamic therapies can be divided into the following categories: photodynamic therapy (PDT)[220], electrodynamic therapy (EDT)[221], radiodynamic therapy (RDT)[222], sonodynamic therapy (SDT)[223], chemodynamic therapy (CDT)[224] *etc.* Compared with near-infrared light (NIR) with a poor penetration depth (<1 cm) and high-energy X-ray with numerous side effects, ultrasound draws increasing attention with high tissue penetration and bio-safety, which promotes the development of SDT.[225] For traditional SDT, the therapeutic mechanism is mainly attributed to the energy transfer process caused by sonoluminescence due to ultrasound cavitation.[226] The sonoluminescence excites the electron orbitals of the sonosensitizer, and triggers certain photocatalytic processes to enhance the yield of ROS. However, the efficiency of SDT is still heavily restricted from the inefficient separation and rapid recombination of free electrons and holes, leading to the insufficient generation of ROS.

As one of the ultrasound-responsive materials, piezoelectric materials can not only efficiently separate charge carriers under piezo-induced electric field, but also enhance the redox ability in terms of band bending, further promoting ROS generation.[231] Despite the fact that the application of piezoelectric materials was ascribed to SDT by some researchers, the mechanism of the yield of ROS *via* piezocatalysis is different from that of classic sonosensitizers. In 2020, Zhu *et al.* applied tetragonal barium titanate (T-BTO) piezo-electric nanoparticles to kill tumor cells under ultrasound, which was separated from SDT for the first time and has been named 'piezocatalytic therapy' (Fig. 33b).[227] Under the mechanical stimuli provided by low-energy ultrasonic irradiation (1.0 W cm^{-2}), the polarization inside T-BTO changed, and an internal electric field was built inside the lattice. T-BTO exhibited prominent degradation performance (41.36 %) of MB under ultrasonic irradiation compared to control group (7.04 %). It is worth mentioning that the cubic BTO nanoparticles (symmetric structure without piezoelectricity) showed negligible MB degradation performance (10.8 %),
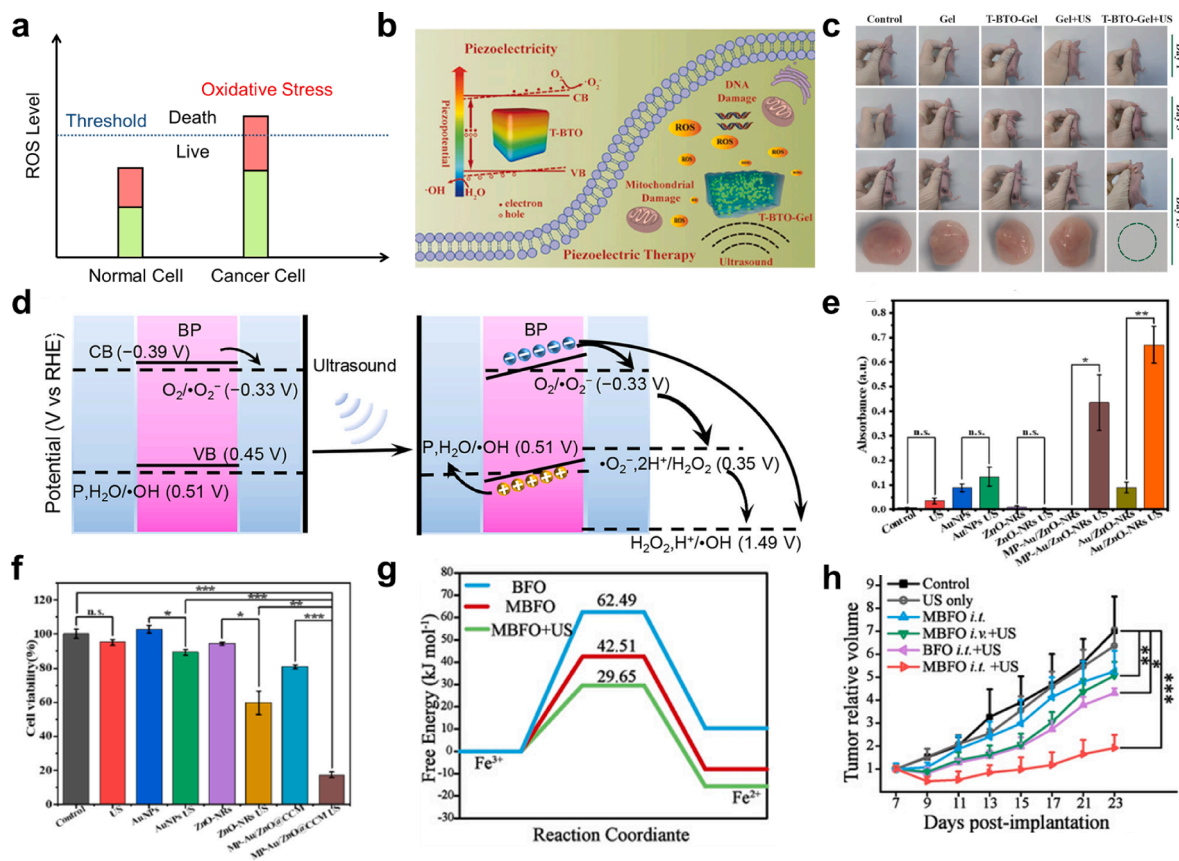
Fig. 33. (a) Schematic illustration of ROS-modulation in normal cell vs. cancer cells (reproduced from [218], with the permission of Elsevier). (b) Schematic mechanism of tetragonal barium titanate (T-BTO) mediated piezocatalytic tumor therapy (reproduced from [227], with the permission of Wiley). (c) Photos of tumor bearing mice and corresponding tumor regions after different treatment conditions using T-BTO (reproduced from [227], with the permission of Wiley). (d) Schematic illustration of the original energy band structure of black phosphorus nanosheets (BP NS) and tilted band structure under piezo-induced electric field, which facilitated ·OH yield (reproduced from [228], with the permission of American Chemical Society). (e) Absorbance at 650 nm of 3,3',5,5'-tetramethylbenzidine (TMB) generated by cascade catalysis in 1 mg mL^{-1} glucose solution for different treatment groups (reproduced from [229], with the permission of Elsevier). (f) Cell viabilities of C6 cells in different treatment groups (reproduced from [229], with the permission of Elsevier). (g) Energy diagram for Fe^{3+}–Fe^{2+} conversion process under different electron density conditions (reproduced from [230], with the permission of Wiley). (h) Relative tumor volumes in different treatment groups during the therapeutic process (*$p < 0.05$, **$p < 0.01$, ***$p < 0.001$) (reproduced from [230], with the permission of Wiley).

which confirms the role of piezoelectricity played in promoting the yield of ROS. Based on the simulation using finite element method (FEM), the piezopotential generated by T-BTO is enough to tilt the energy bands favoring the reduction of O_2 to generate ·O_2^-, as well as the oxidation of H_2O to generate ·OH. Finally, the enhanced yield of ROS contributed to the oxidative damage of tumor cells, as evaluated *in vitro* and *in vivo* (Fig. 33c).

Apart from classic piezoelectric perovskites, emerging piezoelectric materials with various structures have also been investigated in terms of anti-tumor effect. For example, few-layer black phosphorus nanosheets (BP NSs) are typical piezoelectrically active 2D semiconductors. In 2021, Li *et al.* prepared few-layer BP NSs based on liquid phase exfoliation method, and studied the killing effect of tumor cell under ultrasonic irradiation.[228] The intrinsic bandgap of BP NSs was measured to be 0.84 eV, where the CB and VB edges were −0.39 eV and 0.45 eV, respectively (vs. RHE). The redox potential of the CB edge of BP NSs was more negative compared to O_2/·O_2^- (−0.33 eV), which indicates that the electrons were energetically favorable for the reduction of O_2. However, the redox potential of the VB edge was less positive compared to H_2O/·OH (0.51 eV). It is worth mentioning that the built-in electric field formed under ultrasound tilted the VB position, which turned out to be more positive than the redox potential of H_2O/·OH (Fig. 33d). This work inspires that similar 2D-structured piezoelectric materials (e.g., WS_2 and MoS_2) have the potential to be applied in tumor treatment. [232]

In addition to material selection, electronic structure design is a vital technology to tailor the piezocatalytic performance, e.g., heterostructure construction [233] and defect engineering [171]. In terms of heterostructure construction, Ma *et al.* designed and prepared heterostructured Au/ZnO nanoparticles which were further modified with mitochondrial targeting peptides (MLS) and polyethylene glycol (PEG) and coated with C6 cell membrane (MP-Au/ZnO@CCM) for tumor treatment.[229] The Schottky barrier was formed between the insulated ZnO and metallic Au nanoparticles. Apart from the ability to decompose H_2O and O_2, Au/ZnO

exhibited peroxidase-like activity owing to the introduction of Au nanoparticles, which could catalyze the decomposition of H_2O_2 to generate ROS. Moreover, based on simulation results of the electric properties of Au/ZnO under ultrasound, the piezopotential and current density were estimated to be 140 mV and 70 A m^{-2}, respectively. The enhanced current density around the Au nanoparticles favored the migration and separation of electrons and holes, thus promoting the enzyme-like catalytic behavior of Au/ZnO. Based on the oxidation experiments of 3,3',5,5'-tetramethylbenzidine (TMB), the blue color could be observed in the MP-Au/ZnO-NRs + US group and Au/ZnO-NRs + US group when glucose was used to evaluate the cascade catalytic activity, suggesting that the introduction of ZnO can enhance the catalytic activity of Au (Fig. 33e). MP-Au/ZnO@CCM exhibited satisfactory performance of cell killing with the cell viability reduced to 17.40% under ultrasonic irradiation (Fig. 33f). It is also worth mentioning that the piezopotential generated by MP-Au/ZnO@CCM could disturb mitochondrial membrane potential and lead to cell apoptosis, other than the yield of ROS during the therapeutic process. In terms of defect engineering, Wang *et al.* applied KNN-based nanocrystals with the composition of 0.92(Na$_{0.5}$K$_{0.5}$)NbO$_3$-0.02(B$_{i0.5}$Li$_{0.5}$)TiO$_3$-0.06BaZrO$_3$ to the osteosarcoma treatment.[234] The enhanced generation of ROS was attributed to the increased catalytic behavior of oxygen vacancies in combination with enhanced separation of charge carriers driven by the built-in electric field.

In tumor cells, the yield of ROS is originated not only from H_2O and O_2, but also from the overexpressed H_2O_2, which can be associated with Fenton reactions.[235] CDT is a novel tumor treatment strategy based on the promotion of Fenton/Fenton-like reactions to catalyze the conversion of intratumoral H_2O_2 into strong oxidative ·OH, thereby inducing the apoptosis of tumor cells.[236] As is mentioned in Section 6.1.3, the introduction of piezo-induced electric field in Fenton catalysts can facilitate the generation of ·OH. In 2021, Zhao *et al.* proposed the 'intra-crystalline electron lever' (IEL) strategy, and fabricated the piezoelectric 3% Mn^{4+}-doped bismuth ferrite (BiFe$_{0.97}$Mn$_{0.03}$O$_3$, MBFO) nanocrystals using air-quenching sol–gel method.[230] In MBFO, the concentration of free electrons was enhanced through the donor doping of Mn^{4+} ions. Meanwhile, a Mn^{4+}-O-Fe^{3+} local dipole, named as 'electron lever',
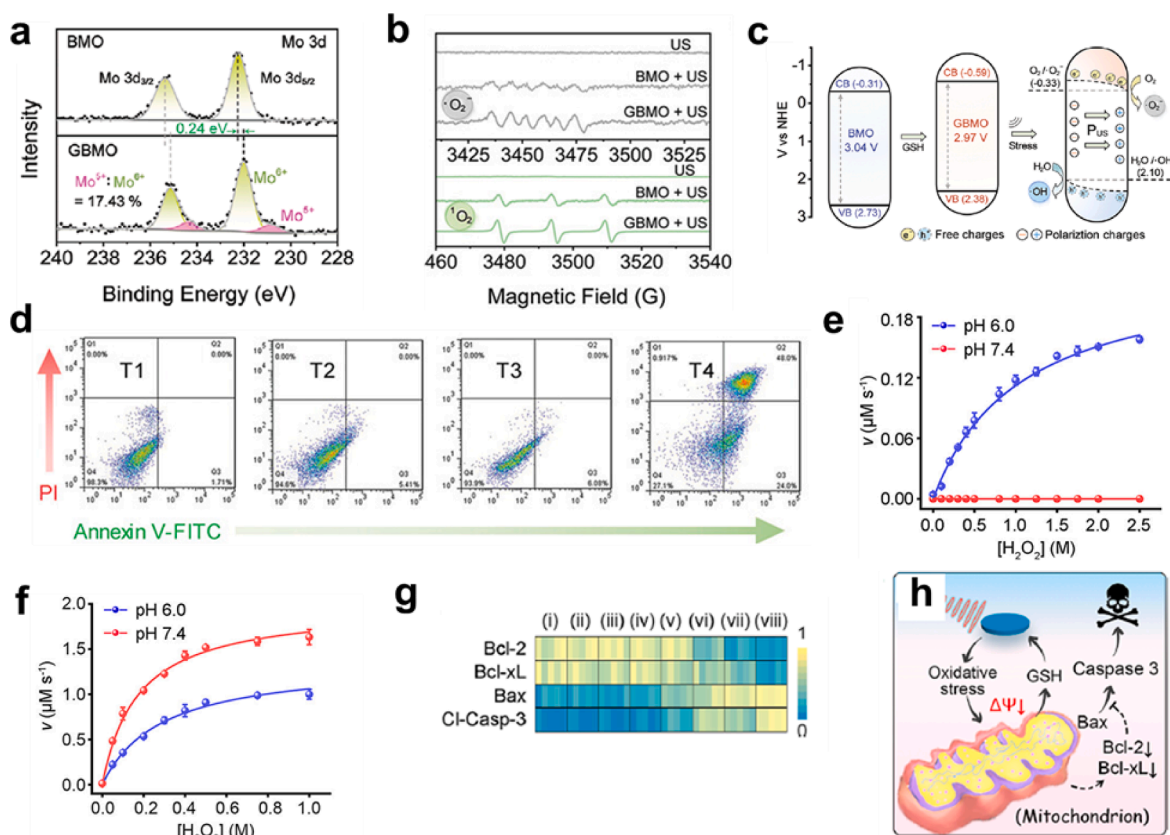

Fig. 34. Bismuth molybdate (Bi$_2$MoO$_6$) nanoribbons (BMO NRs) for glutathione-enhanced sonodynamic therapy (reproduced from [237], with the permission of Wiley): (a) Mo 3d peaks in the XPS spectra of BMO NRs before and after incubation with glutathione (GBMO); (b) ESR spectra of ·O$_2^-$ trapped by 5,5-dimethyl-1-pyrroline N-oxide (DMPO) and $^1O_2$ trapped by 2,2,6,6-Tetramethyl-4-piperidinol (TEMP); (c) the schematic illustration of the energy band structure of BMO and GBMO NRs, and tilted energy bands under piezo-induced electric field, which facilitated the yield of ·O$_2^-$ and ·OH and (d) Fluorescein–annexin V and PI staining assay of HeLa cells treated with different conditions. MnTiO$_3$ nanodisks for multiple enzymatic-mimicking activities (reproduced from [238], with the permission of American Chemical Society): (e) peroxidase (POD)-like and (f) catalase (CAT)-like enzymatic kinetics rate of MnTiO$_3$ nanodisks under different pH conditions; (g) relative expression of Bcl-2, Bcl-xL, Bax, and cleaved caspase-3 (Cl-Casp-3) was normalized to the expression of GAPDH for different treatment groups which were blank control (i), pH 6.0 (ii), ultrasound (iii), pH 6.0 + ultrasound (iv), MnTiO$_3$ nanodisks (v), MnTiO$_3$ nanodisks + pH 6.0 (vi), MnTiO$_3$ nanodisks + ultrasound (vii) and MnTiO$_3$ nanodisks + pH 6.0 + ultrasound (viii), and (h) the mechanism of cell apoptosis after the treatment with MnTiO$_3$ nanodisks and ultrasound.

was constructed, which could efficiently regulate the distribution of valence electrons and free electrons around the Fe^{3+} site. More interestingly, under ultrasonic irradiation, the piezo-induced electric field in MBFO could drive excess free electrons to the Fe site for further accumulation of electrons. As a result, the enhanced electron density on Fe site lowered the activation energy of rate determining Fe^{3+} reduction step in the Fenton reaction (Fig. 33g). Therefore, the energy barrier of Fe^{3+}/Fe^{2+} conversion was reduced by 55.3%, and the kinetics rate was increased by 6.1 times, and finally enhancing the yield of ·OH. Moreover, satisfactory CDT efficiency was achieved in terms of *in vitro* and *in vivo* anti-cancer effect of MBFO under ultrasound (Fig. 33h).

Apart from the structure engineering of piezoelectric materials, the therapeutic effect of ultrasound-driven piezocatalytic therapy can be further optimized from the perspective of biological characteristics of tumor cells. For example, the efficiency of ROS-based therapy suffers from a high level of antioxidant (1–10 mM), such as glutathione (GSH), in the tumor microenvironment, which renders the tumor cells more resistant to oxidative stress. In 2021, Dong *et al.* prepared 2D bismuth molybdate (Bi_2MoO_6) nanoribbons (BMO NRs) *via* hydrothermal method.[237] BMO features a unique layered Aurivillius structure, consisting of $[Bi_2O_2]^{2+}$ layers sandwiched between $[MoO_4]^{2-}$ slabs. The BMO NRs could react with GSH to further disrupt redox homeostasis in terms of the reduction of Mo^{6+} to Mo^{5+}, which was evidenced based on Mo 3d XPS spectra (Fig. 34a). The generation of ·O_2^- and $^1O_2$ was confirmed using the ESR spectra (Fig. 34b). Moreover, the yield of Mo^{5+} introduced oxygen vacancies to the structure of BMO, which results in a shortened distance between the band edge and the redox potentials of $O_2/·O_2^-$ (−0.33 eV) and $H_2O/·OH$ (2.10 eV) (Fig. 34c). Representative flow cytometric apoptosis assay was conducted to reveal the anti-tumor mechanism of BMO NRs (Fig. 34d). The apoptotic ratio in the T4 group (BMO + US) was up to 72% (sum of Q2 + Q3), which was prominently higher than those of other groups. Furthermore, *in vivo* experiments suggested that BMO NRs could also play the role of a contrast agent for CT imaging to provide real-time X-ray imaging in the evaluation of therapeutic effect.

Moreover, the piezocatalytic performance can be regulated by solution environment, e.g., temperature, pH and ion concentrations. [170] Based on the difference of normal cells and tumor cells in pH, piezocatalysts possess the potential to realize different functions in terms of cell types, which may achieve precise tumor eradication with minimal side effects. In 2022, Xu *et al.* adopted one-pot hydrothermal method to prepare $MnTiO_3$ nanodisks for multiple enzymatic-mimicking activities, covering glutathione oxidase (GSHOx), peroxidase (POD) and catalase (CAT).[238] Featuring multiple valences, manganese usually acts as the catalytic center of various natural enzymes. Considering the sub-acidic (pH = 6.0) tumor microenvironment, $MnTiO_3$ nanodisks was found to exhibit POD-mimicking activity involving H^+ (Fig. 34e). In this way, the overexpressed H_2O_2 was converted into highly toxic ·OH to damage tumor cells. Comparatively, in normal physiological conditions (pH 7.4), the POD-mimicking activity of $MnTiO_3$ nanodisks could be barely detected, showing CAT-mimicking activity instead (Fig. 34f). In this way, H_2O_2 was converted into non-toxic O_2 in normal cells. Going a step further, the authors built a biocomputing platform based on a Boolean logic-based algorithm. Ultrasound and acidic conditions were selected as input signals to output toxicity for programed tumor treatment. As a result, Bax/Bcl-2/caspase-3 signaling pathway was reprogrammed to inhibit tumor cells from anti-apoptosis (Fig. 34g and 34 h). Overall, this research broadened the range of artificial enzymes with piezocatalysts, and shed light on the design of next-generation nanomedicine for more precise and effective tumor treatment.

6.3.2. Anti-bacteria

In the human body, the bacteria in the gastrointestinal tract play an essential role in maintaining the regular functions of the immune system.[239] The chemical substances they produce can regulate the immune system, so that the immunity can remain in an appropriate state of defense.[240] As long as the imbalance of the bacteria takes place, the mutualism between human and bacteria is destroyed, and bacteria are likely to induce various diseases, e.g., gastroenteritis. Currently, antibiotics are the most common treatment to kill and inhibit pathogenic bacteria that invade the human body. In order to achieve satisfactory therapeutic effect, the dosage of antibiotics is usually high due to its non-targeting properties, which can cause side effects, such as hematopoietic disorder and liver damage.[241] Moreover, the overuse of antibiotics has been found to be mainly responsible for the development of drug resistance in certain types of bacteria, which may obstruct the treatment if reinfection occurs.[242] Therefore, it is urgent to explore up-to-date antibiotic-free therapies for rapid sterilization.

It has been widely reported that the presence of antibiotics can produce excessive ROS, and further lead to an increased oxidative stress in bacteria, which is the key mechanism of bacterial cell death.[243] In analogy to piezocatalytic therapy for tumor treatment, piezoelectric materials have massive potential in anti-bacteria by means of promoting the yield of ROS under ultrasonic irradiation, without taking the risk of drug resistance. In 2021, Wu *et al.* deposited Au nanoparticles on $BaTiO_3$ nanocubes (Au@BTO) for antimicrobial applications.[244] The as-prepared Au@BTO featured a Schottky heterojunction construction, which could further promote the separation of charge carriers in addition to the piezo-induced potential. To detect the generation of $^1O_2$, 1, 3- diphenyl isobenzofuran (DPBF) was used as the scavenger. The time-dependent $^1O_2$ generation curve for the Au@BTO + ultrasound (US) group showed the largest slope (0.7113 min^{-1}), which was 2.42 times and 5.02 times larger compared to the BTO + US and US group, respectively (Fig. 35a). From the live/dead staining images, the ratio of dead cells in the Au@BTO + US group was calculated to be 81.86% of the total cells, which was higher compared to other groups (Fig. 35b). After ultrasonic irradiation for 4 min, the antibacterial efficiencies of Au@BTO against E. coli (gram-negative) and Staphylococcus aureus (S. aureus, gram-positive) were up to 99.23% and 99.94%, respectively. Au@BTO also exhibited *in vivo* satisfactory antibacterial effect in a model of mouse wound.

In 2021, Liu *et al.* innovatively designed the piezo-deposition of Au on BTO (BTO@Au NPs) to achieve antibacterial effect under low-frequency mechanical vibration like stirring.[245] It should be noted that under mechanical stimuli, the piezo-induced electrons could reduce metal precursors to nanoparticles, which guaranteed the favorable deposition on the electron-accumulated area instead of random chemical reduction (Fig. 35c). This novel design could enhance the charge density around Au and further facilitated the reduction from oxygen to ·O_2^-. For BTO@Au NPs, the degradation efficiency against RhB reached 99 % after stirring for 6 h. As
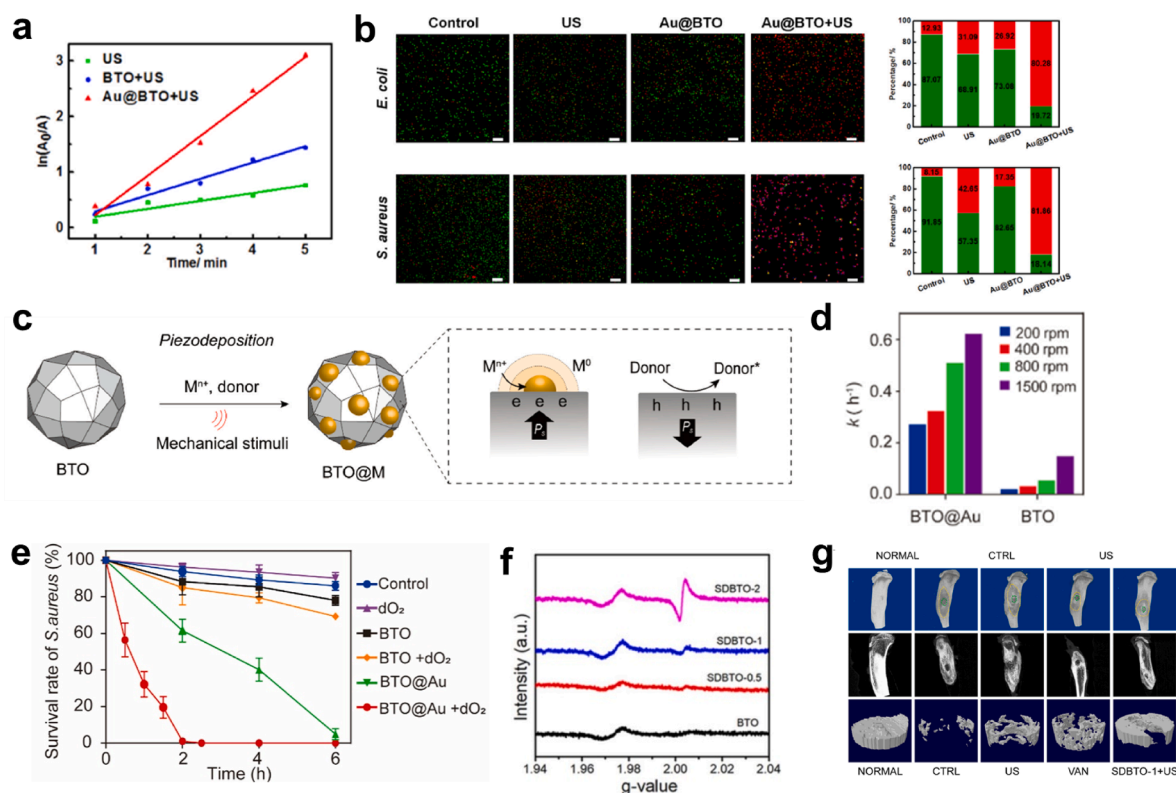
Fig. 35. (a) The kinetic rate constant for DPBF decomposition for US, BTO + US and Au@BTO + US groups (reproduced from [244], with the permission of Elsevier). (b) Live/dead staining images and quantitative analysis of antibacterial effect of Au@BTO against E. coli and S. aureus (reproduced from [244], with the permission of Elsevier). (c) Schematic illustration of piezodeposition process of BTO@Au (reproduced from [245], with the permission of Elsevier). (d) The piezocatalytic performance of BTO and BTO@Au under stirring at 200, 400, 800 and 1500 rpm in terms of the corresponding k values of RhB degradation (reproduced from [245], with the permission of Elsevier). (e) Survival rate of S. aureus before and after different treatment conditions. (f) EPR spectra of BTO and SDBTO (reproduced from [150], with the permission of Elsevier). (g) Micro-CT analysis and reconstruction behavior in different treatment groups, where the yellow and green dotted-line represent the bone destruction area and the defect site, respectively (reproduced from [150], with the permission of Elsevier). (For interpretation of the references to color in this figure legend, the reader is referred to the web version of this article.)

expected, the dye degradation efficiency increased with increasing stirring rates for BTO@Au samples (Fig. 35d). Other low-frequency vibration sources (e.g., votex, rotator, human walking) were also examined to be available to trigger the piezocatalytic reaction. *In vitro* results showed that S. aureus treated with BTO@Au were completely inactivated after stirring for 6 h, which could be reduced to 2 h if additional oxygen was provided (Fig. 35e). Based on RNA sequencing analysis, Bacteroides with the most antibiotic resistance mechanisms underwent a significant decrease in their abundance as total amount of bacteria in BTO@Au + dO_2 group, which suggested that the disinfection effect *via* BTO@Au NPs has potential to treat drug-resistant pathogens. This strategy takes one step further for piezoelectric materials in the treatment of anti-bacteria under mild mechanical vibrations.

Moreover, piezocatalysis can be extended to more disease treatment with the necessity of antibiosis. In 2022, Lei *et al* designed and fabricated sulfur-doped barium titanate (SDBTO) to achieve bacterial inhibition and bone regeneration at the same time.[150] An appropriated amount of sulfur doping increased the local crystal asymmetry, thus enhancing the piezoresponse. Oxygen vacancies, confirmed by unpaired electron signal at g = 2.003 in the EPR spectra (Fig. 35f), were introduced to SDBTO to narrow the bandgap and act as an electropositive center to further separate electrons and holes. These synergistically enhanced the catalytic behavior with surrounding oxygen and water to produce ROS. SDBTO exhibited prominent *in vitro* antibacterial effect with a killing efficiency of 97.12% against S. aureus. Interestingly, the electric field established in SDBTO under ultrasound promoted the osteogenic differentiation of human bone marrow mesenchymal stem cells (hBMSCs) in terms of upregulating the signaling pathway of TGF-β. SDBTO-1 could resist bacterial infection with depressed inflammation and significantly improve bone regeneration simultaneously (Fig. 35g). In sum, the applications of piezocatalytic therapy can be further extended to other disease treatment considering antibacterial and tissue regeneration.

6.3.3. Alzheimer's disease treatment

Alzheimer's disease (AD) is one of the most common chronic neurodegenerative diseases.[246] It has been generally acknowledged that the major pathological features of AD are the self-assembly of Aβ monomers into aggregates and their deposition on extracellular

regions of the brain.[247] As a result, the accumulation of Aβ aggregates can cause neurons and synapses to lose physiological functions.[248] Due to the strong side-chain interactions in Aβ structures, Aβ aggregates are highly resistant to dissociation by classic physical or chemical method.[249] In 2020, Jang *et al.* firstly applied bismuth oxychloride (BiOCl) nanosheets to dissociate Aβ aggregates for AD treatment (Fig. 36a).[250] BiOCl possesses an anisotropic layered structure consisting of $[Bi_2O_2]^{2+}$ slabs and interlayered double Cl^- slabs with dominant (0 0 1) facets. Using thioflavin T (ThT) as a fluorescence probe into β-sheet structure, and bicinchoninic acid (BCA) assay to evaluate the amount of protein, the decrease of ThT-binding sites on the Aβ fibrils was attributed to the piezocatalysis effect of BiOCl nanosheets instead of adsorption. Based on circular dichroism (CD) analysis, the intensity of peak corresponding to β-sheet-rich secondary structure decreased only in the experimental group incubated with BiOCl nanosheets after ultrasonic treatment (Fig. 36b). In the AFM images, the Aβ fibrils were observed to be broken into tiny debris, which was <100 nm in length (Fig. 36c). Moreover, it was suggested that the dissociation of Aβ fibrils was attributed to the ROS catalyzed by BiOCl nanosheets. The oxidative damage in Aβ fibrils was examined using ionization time-of-flight mass spectrometry (MALDI-TOF-MS). Moreover, the alleviated neurotoxicity induced by piezocatalysis induced by BiOCl nanosheets was validated using *in vitro* and *ex vivo* models (Fig. 36d and 36e). It has been also reported that the controlled electric signal can effectively realize neuro modulation and neuronal repair, and piezoelectric materials have massive potential in neurological disease treatment in the future.

6.3.4. Aesthetic medicine

Different from disease treatment, aesthetic medicine focuses on altering cosmetic appearance through the treatment of conditions, covering scars, wrinkles, excess fat, *etc.* In the modern world, the demand of tooth whitening has been increased sharply with the
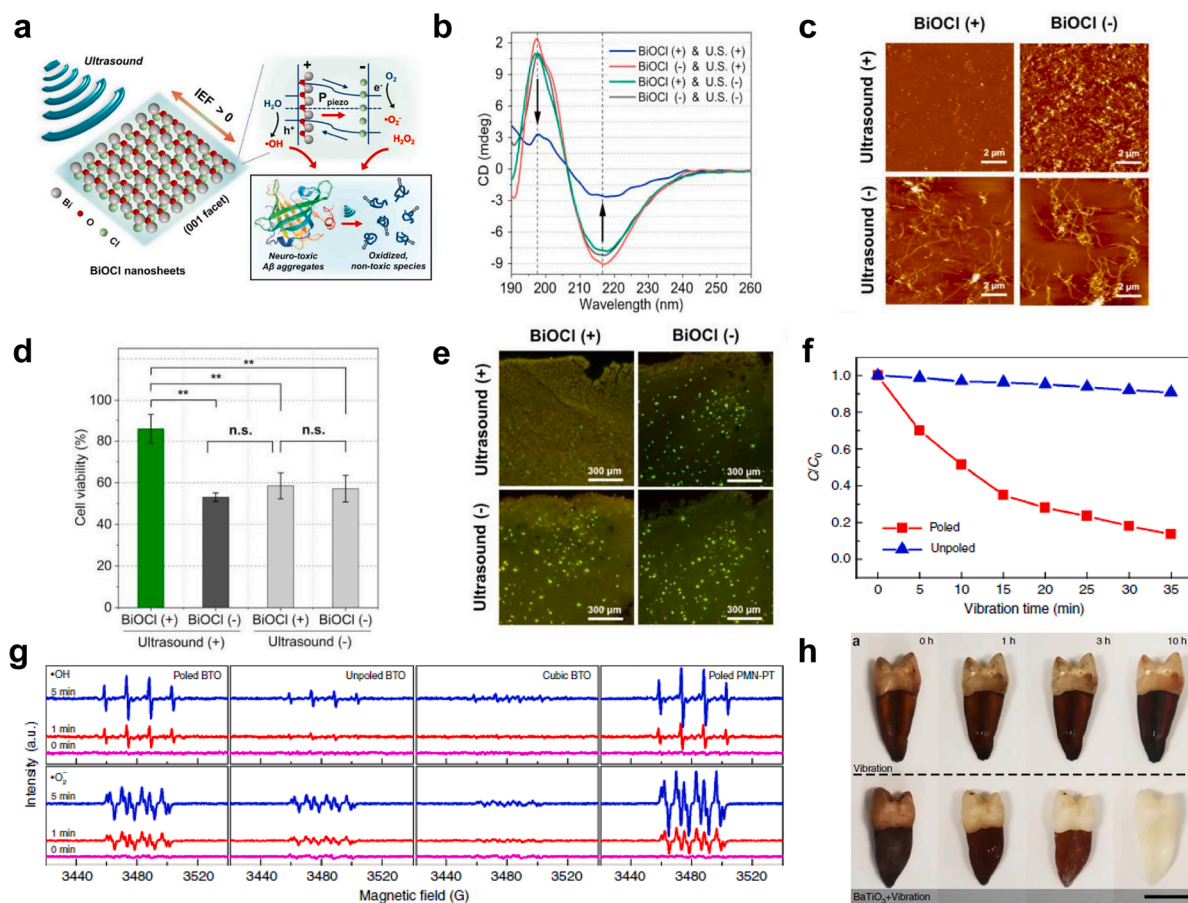

Fig. 36. BiOCl nanosheets for the treatment of AD (reproduced from[250], with the permission of Elsevier): (a) schematic mechanism of piezocatalysis-based dissociation of Aβ aggregates mediated by BiOCl nanosheets; (b) CD spectrua of Aβ fibrils after treating Aβ fibrils with/without BiOCl nanosheets after ultrasound; (c) the AFM images of Aβ fibrils after incubated with/without BiOCl nanosheets under ultrasound; (d) the alleviated neurotoxicity of Aβ fibrils after different treatment conditions, and all of the values were statistically analyzed by means of one-way ANOVA (n = 3, **p < 0.01, n.s. not significant) and (e) Fluorescent images of ThS-stained brain slices after various treatment conditions. Poled BaTiO$_3$ for tooth whitening (reproduced from[110], with the permission of Nature Portfolio): (f) piezocatalytic degradation efficiency of the poled and unpoled BTO nanoparticles; (g) ESR spectra of ·OH and ·O$_2^-$ trapped with different treatment groups in water (top) and dimethyl sulfoxide (DMSO) dispersion (bottom), respectively and (h) the photographs of single tooth under treatment of vibration in pure deionized water (top) and poled BTO turbid liquid (bottom) for 0, 1, 3, and 10 h, respectively.

evolution of aesthetic standard.[251] The traditional way is based on the mechanical friction between tooth and abrasives in the toothpaste, which is time-consuming and may cause side effects to the teeth. In 2020, Wang *et al.* innovatively applied poled BaTiO$_3$ (BTO) nanoparticles to degrade organic compounds stained on the teeth in terms of the piezocatalytic release of ROS.[110] To evaluate the catalytic performance of poled BTO, over 90% of Indigo Carmine was degraded with poled BTO after ultrasonic vibration for 35 min. The kinetic rate constant of RhB with poled BTO ($k = 0.448$ h^{-1}) was about eight times higher compared to the unpoled BTO ($k = 0.062$ h^{-1}) (Fig. 36f), which might be attributed to the enhanced piezoelectricity after poling. Furthermore, the significant role of piezoelectricity was verified based on the ultrahigh kinetic rate constant of poled single crystal PMN-PT powder ($k \sim 0.036$ min^{-1}). The comparison of reactive species (·OH and ·O$_2^-$) yield was further evaluated based on the ESR results (Fig. 36g). To simulate long-term daily toothbrushing, the tooth was brushed using an electric toothbrush periodically at 2 min intervals for 10 h instead of ultrasonic vibration. Based on the Commission Internationale De L'Eclairage (CIELab) measurements, the tooth brushed using poled BTO turbid liquid showed a prominent whitening effect, while there was no obvious change in the color of the tooth brushed with water alone (Fig. 36h). Finally, the application of poled BTO was demonstrated to do much less harm to the enamel and biological cells compared to H$_2$O$_2$, which made piezocatalysts promising candidates to replace abrasives in the toothpaste. This work not only firstly introduced piezocatalysis to aesthetic medicine, but also inspired the exploration of piezocatalysis in other biomedical applications related to generation of ROS.

7. Summary and perspective

Piezocatalysis, an emerging frontier catalytic technique driven by mechanical energy, has great potentials in various fields of application such as environmental remediation, renewable energy production and biotechnology. In this review, we summarized the recent advances of piezocatalysis with special emphasis on decoding the underlying correlation between the catalytic activity and piezo-/ferroelectric physics. The reaction process of piezocatalysis is dominated by the piezo-potential generated under the stimuli of mechanical strain. Here are the main points:

i). The category of piezocatalysts has extended from classic inorganic oxides to 2D-layered materials and polymer-based piezo-electrics. Materials with ferroelectricity are drawing increasing attention due to immense design space to regulate piezoelectricity.

ii). The mainstreams of piezocatalytic mechanisms are based on either energy band theory or screening charge effect. Rational explanations of piezocatalysis have been provided to support their own concepts in terms of experimental results and theoretical simulations. It is highlighted that the connection between piezopotential and piezocatalytic performance has been acknowledged in both theories.

iii). The distinction between piezocatalysis and photocatalysis/pyrocatalysis/electrocatalysis/tribo-catalysis have been elaborated. Considering the comparatively low catalytic efficiency of piezocatalysis, the coupling between piezocatalysis and other catalysis technologies should arouse more attention from researchers.

iv). In piezoelectric/ferroelectric physics, piezoelectric properties are intimately linked with polarization rotation (intrinsic) and domain switching (extrinsic). The coexistence of multiple phases, the decrease of domain size and introduction of field-induced phase transitions are useful to enhance piezoelectric properties, thus improving piezocatalytic performance.

v). The design strategies to enhance the piezocatalytic efficiency covers morphology and facet control, defect engineering, polarization modulation (ferroelectrics), heterostructure construction and composites creation.

vi). Piezocatalysis can take place in a variety of complex environments, and have broader potential applications involving environmental remediation, renewable energy production and biomedicine.

In piezoelectric/ferroelectric physics, piezoelectric properties are intimately linked with polarization rotation (intrinsic) and domain switching (extrinsic) behavior. Generally speaking, the coexistence of multiple phases facilitates the polarization rotation and the decrease of domain size facilitates the motion of domain wall, which will enhance piezoelectric properties. However, the correlation between catalytic reaction kinetics and physical mechanism is still unexplored in various aspects. Some aspects are shown below:

7.1. The temperature sensitivity of electrical properties

As the most investigated mechanical stimuli source of piezocatalysis, ultrasonic irradiation also exhibits thermal effects, which increases ambient temperature during the reaction. Piezoelectric properties, on the other hand, are closely related to the working temperature. For a few lead-free ferroelectric systems, e.g., KNN and BNT, the temperature sensitivity of structural evolution and piezoelectric properties is yet to be clearly elucidated, which impedes the further investigation of piezocatalysis. Moreover, the quantitative analysis of relationship between the variation of temperature and the power density of ultrasonication, as well as the duration of time is necessary to control the thermal effect of ultrasonication, which also benefits the designated shift of Curie point or the depolarization temperature of ferroelectrics to optimize the piezoelectric performance at practical working temperature. Therefore, future work should focus on balancing the thermal effect of ultrasonication and the temperature sensitivity of piezoelectricity.

7.2. Electric field-induced phase transitions

In the application of piezoelectric ceramics, poling is an effective strategy to enhance piezoelectric properties, which require a continuous period of time under a DC voltage. Poling treatment makes the polarization of domains align along the direction of the electric field, which boosts the piezoelectric properties.[252] The importance of poling treatment before application has been gradually acknowledged to enhance piezocatalytic efficiency. Apart from domain switching in ferroelectrics, electric field-induced phase transitions can take place in relaxor ferroelectrics and anti-ferroelectrics, which have a great impact on the piezo-response as well. However, the impact of field-induced transitions on the piezocataytic performance has not been studied so far. Both experimental results and theoretical calculation should be carried out.

7.3. Doping effect

Apart from poling treatment, doping is another strategy to tailor piezoelectric properties, in terms of regulating lattice distortion and domain wall motion. It should be noted that doping can also lead to the formation of cation/anion defects and affect the charge carrier density and charge transfer rate, which play a dominant role in the reaction kinetics of piezocatalysis. Moreover, the electron spin state of doping element can also change the reactivity of the piezocatalysts. Despite the fact that doping has already attracted attention in regulating piezocatalysis, a comprehensive understanding of the doping effect on the electronic structure, the kinetics of charge transfer and the reaction of piezoelectric materials has not been achieved, and requires more efforts to put into.

As an emerging research area involving condensed matter physics and process chemistry, piezocatalysis has been developed rapidly in this decade and shows massive potential in various applications. In the future, researchers with different backgrounds, mainly embracing piezoelectric physics and catalysis, should work more closely to put more efforts to investigating and clarifying the relationship between piezoelectric properties enhancement and chemical reactivity optimization. We believe that significant progress will be made to enhancing piezocatalytic efficiency with the deepening of understanding physicochemical relationship of piezocatalysts, which may further extend the application areas and increase practicability of piezocatalysis.

Declaration of Competing Interest

The authors declare that they have no known competing financial interests or personal relationships that could have appeared to influence the work reported in this paper.

Data availability

Data will be made available on request.

Acknowledgement

References

[1] Wu C, Wang AC, Ding W, Guo H, Wang ZL. Triboelectric Nanogenerator: A Foundation of the Energy for the New Era. Adv Energy Mater 2019;9:1802906.

[2] Liu J, Qi W, Xu M, Thomas T, Liu S, Yang M. Piezocatalytic Techniques in Environmental Remediation. Angew Chem Int Ed 2023;62:e202213927.

[3] Zhang M, Zhao S, Zhao Z, Li S, Wang F. Piezocatalytic Effect Induced Hydrogen Production from Water over Non-noble Metal Ni Deposited Ultralong GaN Nanowires. ACS Appl Mater Interfaces 2021;13:10916–24.

[4] Liu W, Fu P, Zhang Y, Xu H, Wang H, Xing M. Efficient hydrogen production from wastewater remediation by piezoelectricity coupling advanced oxidation processes. Proc Natl Acad Sci 2023;120.

[5] Chen S, Zhu P, Mao L, Wu W, Lin H, Xu D, et al. Piezocatalytic Medicine: An Emerging Frontier Using Piezoelectric Materials for Biomedical Applications. Adv Mater 2023;2208256.

[6] Wang Y, Tang Q, Wu R, Sun S, Zhang J, Chen J, et al. Ultrasound-Triggered Piezocatalysis for Selectively Controlled NO Gas and Chemodrug Release to Enhance Drug Penetration in Pancreatic Cancer. ACS Nano 2023;17:3557–73.

[7] Wang Y-C, Wu JM. Effect of Controlled Oxygen Vacancy on H_2-Production through the Piezocatalysis and Piezophototronics of Ferroelectric R_3C $ZnSnO_3$ Nanowires. Adv Funct Mater 2020;30:1907619.

[8] Wu JM, Chang WE, Chang YT, Chang C-K. Piezo-Catalytic Effect on the Enhancement of the Ultra-High Degradation Activity in the Dark by Single- and Few-Layers MoS_2 Nanoflowers. Adv Mater 2016;28:3718–25.

[9] Wu M-H, Lee J-T, Chung YJ, Srinivaas M, Wu J-M. Ultrahigh efficient degradation activity of single- and few-layered $MoSe_2$ nanoflowers in dark by piezo-catalyst effect. Nano Energy 2017;40:369–75.

[10] Wang C, Hu C, Chen F, Li H, Zhang Y, Ma T, et al. Polar Layered Bismuth-Rich Oxyhalide Piezoelectrics Bi_4O_5X2 (X=Br, I): Efficient Piezocatalytic Pure Water Splitting and Interlayer Anion-Dependent Activity. Adv Funct Mater 2023;2301144.

[11] Gaur A, Dubey S, Elqahtani ZM, Sb A, Al-Buriahi MSA, Vaish R, et al. Effect of Poling on Multicatalytic Performance of $0.5Ba(Zr_{0.2}Ti_{0.8})O_3$–$0.5(Ba_{0.7}Sr_{0.3})TiO_3$ Ferroelectric Ceramic for Dye Degradation. Materials 2022;15:8217..

[12] Sharma M, Singh G, Vaish R. Dye degradation and bacterial disinfection using multicatalytic $BaZr_{0.02}Ti_{0.98}O_3$ ceramics. J Am Ceram Soc 2020;103:4774–84.

[13] Kumar M, Vaish R, Elqahtani ZM, Kebaili I, Al-Buriahi MS, Sung TH, et al. Piezo-photocatalytic activity of $Bi_2VO_{5.5}$ for methylene blue dye degradation. J Mater Res Technol 2022;21:1998–2012.

[14] Singh G, Sharma M, Vaish R. Exploring the piezocatalytic dye degradation capability of lithium niobate. Adv Powder Technol 2020;31:1771–5.

[15] Huang X, Yan W, Sun J, Hu T, Feng J, Huang Z, et al. Inorganic hydrogen-bonded $SnO(OH)_2$ as molecular springs boosted the piezocatalytic degradation of contaminants. Environ Sci Nano 2023;10:1109–25.

[16] Singh KP, Singh G, Vaish R. Utilizing the localized surface piezoelectricity of centrosymmetric $Sr_{1-x}Fe_xTiO_3$ (x≤0.2) ceramics for piezocatalytic dye degradation. J Eur Ceram Soc 2021;41:326–34.

[17] Singh G, Sharma M, Vaish R. Transparent ferroelectric glass–ceramics for wastewater treatment by piezocatalysis. Communications Materials 2020;1:100.

[18] Sharma M, Singh G, Vaish R. Transparent glass-nanocomposites possessing piezoelectric ZnO/Zn_2SiO_4 nanocrystallites for piezocatalytic dye degradation. Environ Sci Water Res Technol 2023;9:533–41.

[19] Singh G, Sharma M, Vaish R. Polar glass-ceramics for piezocatalytic applications. J Appl Phys 2021;130.

[20] Kumar M, Singh G, Vaish R. A reduced graphene oxide/bismuth vanadate composite as an efficient piezocatalyst for degradation of organic dye. Materials Advances 2021;2:4093–101.

[21] Alfryyan N, Kumar S, Ahmed SB, Kebaili I, Boukhris I, Azad P, et al. Electric Poling Effect on Piezocatalytic $BaTiO_3$/Polymer Composites for Coatings. Catalysts 2022;12:1228.

[22] Meng N, Zhang Y, Liu Y, Shi Y, Jiang R, Wu J, et al. Boosting photocatalytic removal of organic pollutants through enhanced piezoelectricity in free-standing nanofibril pyridyl-functionalized conjugated microporous polymer/poly(vinylidene fluoride–trifluoroethylene) hybrids. J Mater Chem C 2022;10:15367–76.

[23] Sharma M, Singh G, Vaish R. Piezocatalysis in ferroelectric $Ba_{0.85}Ca_{0.15}Ti_{0.9}O_3$/polyvinylidene difluoride (PVDF) composite film. J Appl Phys 2021;130.

[24] Shi J, Yang S, Zheng Z, Li J, Wang L, Zeng W, et al. Textile-based piezocatalytic platform for organics degradation under low-frequency water flow. J Mater Chem A 2023;11:7596–604.

[25] Tan D, Xiang Y, Leng Y, Leng Y. On the metal/ZnO contacts in a sliding-bending piezoelectric nanogenerator. Nano Energy 2018;50:291–7.

[26] You H, Li S, Fan Y, Guo X, Lin Z, Ding R, et al. Accelerated pyro-catalytic hydrogen production enabled by plasmonic local heating of Au on pyroelectric $BaTiO_3$ nanoparticles. Nat Commun 2022;13:6144.

[27] Chen Y, Wang L, Gao R, Zhang Y-C, Pan L, Huang C, et al. Polarization-Enhanced direct Z-scheme $ZnO-WO_{3-x}$ nanorod arrays for efficient piezoelectric-photoelectrochemical Water splitting. Appl Catal B 2019;259:118079.

[28] Singh S, Khare N. Coupling of piezoelectric, semiconducting and photoexcitation properties in $NaNbO_3$ nanostructures for controlling electrical transport: Realizing an efficient piezo-photoanode and piezo-photocatalyst. Nano Energy 2017;38:335–41.

[29] Liu Y-L, Wu JM. Synergistically catalytic activities of $BiFeO_3/TiO_2$ core-shell nanocomposites for degradation of organic dye molecule through piezophototronic effect. Nano Energy 2019;56:74–81.

[30] Kumar M, Ansari MNM, Boukhris I, Al-Buriahi MS, Alrowaili ZA, Alfryyan N, et al. Sonophotocatalytic Dye Degradation Using $rGO-BiVO_4$ Composites. Global Chall 2022;6:2100132.

[31] Pan L, Sun S, Chen Y, Wang P, Wang J, Zhang X, et al. Advances in Piezo-Phototronic Effect Enhanced Photocatalysis and Photoelectrocatalysis. Adv Energy Mater 2020;10:2000214.

[32] Jing L, Xu Y, Xie M, Li Z, Wu C, Zhao H, et al. Piezo-photocatalysts in the field of energy and environment: Designs, applications, and prospects. Nano Energy 2023;108508.

[33] Zhu Q, Zhang K, Li D, Li N, Xu J, Bahnemann DW, et al. Polarization-enhanced photocatalytic activity in non-centrosymmetric materials based photocatalysis: A review. Chem Eng J 2021;426:131681.

[34] Tu S, Guo Y, Zhang Y, Hu C, Zhang T, Ma T, et al. Piezocatalysis and Piezo-Photocatalysis: Catalysts Classification and Modification Strategy, Reaction Mechanism, and Practical Application. Adv Funct Mater 2020;30:2005158.

[35] Mohanty R, Mansingh S, Parida K, Parida K. Boosting sluggish photocatalytic hydrogen evolution through piezo-stimulated polarization: a critical review. Mater Horiz 2022;9:1332–55.

[36] Meroni D, Bianchi CL. Ultrasound waves at the service of photocatalysis: From sonochemical synthesis to ultrasound-assisted and piezo-enhanced photocatalysis. Curr Opin Green Sustainable Chem 2022;36:100639.

[37] Li S, Zhao Z, Zhao J, Zhang Z, Li X, Zhang J. Recent Advances of Ferro-, Piezo-, and Pyroelectric Nanomaterials for Catalytic Applications. ACS Applied Nano Materials 2020;3:1063–79.

[38] Hu C, Tu S, Tian N, Ma T, Zhang Y, Huang H. Photocatalysis Enhanced by External Fields. Angew Chem Int Ed 2021;60:16309–28.

[39] Wang K, Han C, Li J, Qiu J, Sunarso J, Liu S. The Mechanism of Piezocatalysis: Energy Band Theory or Screening Charge Effect? Angew Chem Int Ed 2022;61: e202110429.

[40] Bößl F, Tudela I. Piezocatalysis: Can catalysts really dance? Curr Opin Green Sustainable Chem 2021;32:100537.

[41] Qian W, Yang W, Zhang Y, Bowen CR, Yang Y. Piezoelectric Materials for Controlling Electro-Chemical Processes. Nano-Micro Letters 2020;12:149.

[42] Ali A, Chen L, Nasir MS, Wu C, Guo B, Yang Y. Piezocatalytic removal of water bacteria and organic compounds: a review. Environ Chem Lett 2023;21: 1075–92.

[43] Jiang Z, Tan X, Huang Y. Piezoelectric effect enhanced photocatalysis in environmental remediation: State-of-the-art techniques and future scenarios. Sci Total Environ 2022;806:150924.

[44] Liang Z, Yan C-F, Rtimi S, Bandara J. Piezoelectric materials for catalytic/photocatalytic removal of pollutants: Recent advances and outlook. Appl Catal B 2019;241:256–69.

[45] Mamba G, Mafa PJ, Muthuraj V, Mashayekh-Salehi A, Royer S, Nkambule TIT, et al. Heterogeneous advanced oxidation processes over stoichiometric ABO_3 perovskite nanostructures. Materials Today Nano 2022;18:100184.

[46] Gao J, Hu X, Wang Y, Liu Y, Zhang L, Ke X, et al. Understanding the mechanism of large dielectric response in Pb-free $(1-x)Ba(Zr_{0.2}Ti_{0.8})O_3-x(Ba_{0.7}Ca_{0.3})TiO_3$ ferroelectric ceramics. Acta Mater 2017;125:177–86.

[47] Wang B, Li F, Chen L-Q. Inverse Domain-Size Dependence of Piezoelectricity in Ferroelectric Crystals. Adv Mater 2021;33:2105071.

[48] Ren X. Large electric-field-induced strain in ferroelectric crystals by point-defect-mediated reversible domain switching. Nat Mater 2004;3:91–4.

[49] Gindele O, Kimmel A, Cain MG, Duffy D. Shell Model force field for Lead Zirconate Titanate $Pb(Zr_{1-x}Ti_x)O_3$. J Phys Chem C 2015;119:17784–9.

[50] Ma C, Guo H, Beckman SP, Tan X. Creation and Destruction of Morphotropic Phase Boundaries through Electrical Poling: A Case Study of Lead-Free $(Bi_{1/2}Na_{1/2})TiO_3-BaTiO_3$ Piezoelectrics. Phys Rev Lett 2012;109:107602.

[51] Qiu C, Wang B, Zhang N, Zhang S, Liu J, Walker D, et al. Transparent ferroelectric crystals with ultrahigh piezoelectricity. Nature 2020;577:350–4.

[52] Zhang S, Li F, Jiang X, Kim J, Luo J, Geng X. Advantages and challenges of relaxor-$PbTiO_3$ ferroelectric crystals for electroacoustic transducers – A review. Prog Mater Sci 2015;68:1–66.

[53] Meng N, Ren X, Santagiuliana G, Ventura L, Zhang H, Wu J, et al. Ultrahigh β-phase content poly(vinylidene fluoride) with relaxor-like ferroelectricity for high energy density capacitors. Nat Commun 2019;10:4535.

[54] Zhang SJ, Luo J, Snyder DW, Shrout TR. 5 - High-performance, high-TC piezoelectric crystals. In: Ye Z–G, editor. Handbook of Advanced Dielectric. Piezoelectric and Ferroelectric Materials: Woodhead Publishing; 2008. p. 130–57.

[55] Valasek J. Piezo-Electric Activity of Rochelle Salt under Various Conditions. Phys Rev 1922;19:478–91.

[56] Trolier-McKinstry S, Zhang S, Bell AJ, Tan X. High-Performance Piezoelectric Crystals, Ceramics, and Films. Annu Rev Mat Res 2018;48:191–217.

[57] Takahashi S. Effects of impurity doping in lead zirconate-titanate ceramics. Ferroelectrics 1982;41:143–56.

[58] Horchidan N, Ciomaga CE, Frunza RC, Capiani C, Galassi C, Mitoseriu L. A comparative study of hard/soft PZT-based ceramic composites. Ceram Int 2016;42: 9125–32.

[59] Galassi C, Roncari E, Capiani C, Craciun F. Processing and characterization of high Qm ferroelectric ceramics. J Eur Ceram Soc 1999;19:1237–41.

[60] Viola G, Tian Y, Yu C, Tan Y, Koval V, Wei X, et al. Electric field-induced transformations in bismuth sodium titanate-based materials. Prog Mater Sci 2021;122: 100837.

[61] Zhou X, Xue G, Luo H, Bowen CR, Zhang D. Phase structure and properties of sodium bismuth titanate lead-free piezoelectric ceramics. Prog Mater Sci 2021; 122:100836.

[62] Wu J, Zhang H, Meng N, Koval V, Mahajan A, Gao Z, et al. Perovskite $Bi_{0.5}Na_{0.5}TiO_3$-based materials for dielectric capacitors with ultrahigh thermal stability. Mater Des 2021;198:109344.

[63] Song G, Liu Z, Zhang F, Liu F, Gu Y, Liu Z, et al. High-throughput synthesis and electrical properties of BNT–BT–KNN lead-free piezoelectric ceramics. J Mater Chem C 2020;8:3655–62.

[64] Park S-E, Shrout TR. Ultrahigh strain and piezoelectric behavior in relaxor based ferroelectric single crystals. J Appl Phys 1997;82:1804–11.

[65] Luo L, Zhao X, Luo H. Chapter 7 - Single Crystal PZN-PT, PMN-PT, PSN-PT, and PIN-PT-Based Piezoelectric Materials. In: Uchino K, editor. Advanced Piezoelectric Materials. (Second Edition): Woodhead Publishing; 2010. p. 271–318.

[66] Zhou Q, Lam KH, Zheng H, Qiu W, Shung KK. Piezoelectric single crystal ultrasonic transducers for biomedical applications. Prog Mater Sci 2014;66:87–111.

[67] Zhang S, Li F. High performance ferroelectric relaxor-PbTiO$_3$ single crystals: Status and perspective. J Appl Phys 2012;111:031301.

[68] Nunes-Pereira J, Costa P, Lanceros-Mendez S. 3.9 Piezoelectric Energy Production. In: Dincer I, editor. Comprehensive Energy Systems. Oxford: Elsevier; 2018. p. 380–415.

[69] Zhang S, Lee S-M, Kim D-H, Lee H-Y, Shrout TR. Temperature dependence of the dielectric, piezoelectric, and elastic constants for $Pb(Mg_{1/3}Nb_{2/3})$ $O_3–PbZrO_3–PbTiO_3$ piezocrystals. J Appl Phys 2007;102:114103.

[70] Echizenya K, Nakamura K, Mizuno K. PMN-PT and PIN-PMN-PT single crystals grown by continuous-feeding Bridgman method. J Cryst Growth 2020;531: 125364.

[71] Sherrell PC, Fronzi M, Shepelin NA, Corletto A, Winkler DA, Ford M, et al. A bright future for engineering piezoelectric 2D crystals. Chem Soc Rev 2022;51: 650–71.

[72] Liu Z, Wang B, Cazorla C. Strain Engineering of Two-Dimensional Piezophotocatalytic Materials for Improved Hydrogen Evolution Reaction. ACS Sustain Chem Eng 2022;10:16924–34.

[73] Wang P, Zong Y, Liu H, Wen H, Wu H-B, Xia J-B. Highly efficient photocatalytic water splitting and enhanced piezoelectric properties of 2D Janus group-III chalcogenides. J Mater Chem C 2021;9:4989–99.

[74] Hinchet R, Khan U, Falconi C, Kim S-W. Piezoelectric properties in two-dimensional materials: Simulations and experiments. Mater Today 2018;21:611–30.

[75] Lovinger AJ. Ferroelectric Polymers. Science 1983;220:1115–21.

[76] Kawai H. The Piezoelectricity of Poly (vinylidene Fluoride). Jpn J Appl Phys 1969;8:975.

[77] Yan Y, Zhou JE, Maurya D, Wang YU, Priya S. Giant piezoelectric voltage coefficient in grain-oriented modified PbTiO$_3$ material. Nat Commun 2016;7:13089.

[78] Li M, Wondergem HJ, Spijkman M-J, Asadi K, Katsouras I, Blom PWM, et al. Revisiting the δ-phase of poly(vinylidene fluoride) for solution-processed ferroelectric thin films. Nat Mater 2013;12:433–8.

[79] Ren X, Meng N, Zhang H, Wu J, Abrahams I, Yan H, et al. Giant energy storage density in PVDF with internal stress engineered polar nanostructures. Nano Energy 2020;72:104662.

[80] Ramadan KS, Sameoto D, Evoy S. A review of piezoelectric polymers as functional materials for electromechanical transducers. Smart Mater Struct 2014;23: 033001.

[81] Huang Y, Rui G, Li Q, Allahyarov E, Li R, Fukuto M, et al. Enhanced piezoelectricity from highly polarizable oriented amorphous fractions in biaxially oriented poly(vinylidene fluoride) with pure β crystals. Nat Commun 2021;12:675.

[82] Qian X, Chen X, Zhu L, Zhang QM. Fluoropolymer ferroelectrics: Multifunctional platform for polar-structured energy conversion. Science 2023;380:eadg0902.

[83] Nishiyama T, Sumihara T, Sato E, Horibe H. Effect of solvents on the crystal formation of poly(vinylidene fluoride) film prepared by a spin-coating process. Polym J 2017;49:319–25.

[84] Furukawa T. Structure and functional properties of ferroelectric polymers. Adv Colloid Interface Sci 1997;71–72:183–208.

[85] Meng N, Mao R, Tu W, Zhu X, Wilson RM, Bilotti E, et al. Processing and characterization of free standing highly oriented ferroelectric polymer films with remarkably low coercive field and high remnant polarization. Polymer 2016;100:69–76.

[86] Liu Y, Aziguli H, Zhang B, Xu W, Lu W, Bernholc J, et al. Ferroelectric polymers exhibiting behaviour reminiscent of a morphotropic phase boundary. Nature 2018;562:96–100.

[87] Manley ME, Abernathy DL, Sahul R, Parshall DE, Lynn JW, Christianson AD, et al. Giant electromechanical coupling of relaxor ferroelectrics controlled by polar nanoregion vibrations. Sci Adv 2016;2:e1501814.

[88] Xia W, Zhang Z. PVDF-based dielectric polymers and their applications in electronic materials. IET Nanodielectrics 2018;1:17–31.

[89] Ren X, Meng N, Yan H, Bilotti E, Reece MJ. Remarkably enhanced polarisability and breakdown strength in PVDF-based interactive polymer blends for advanced energy storage applications. Polymer 2019;168:246–54.

[90] Bauer F, Fousson E, Zhang QM, Lee LM. Ferroelectric copolymers and terpolymers for electrostrictors: synthesis and properties. Proceedings 11th International Symposium on Electrets2002. p. 355-8.

[91] Chu B, Zhou X, Ren K, Neese B, Lin M, Wang Q, et al. A Dielectric Polymer with High Electric Energy Density and Fast Discharge Speed. Science 2006;313: 334–6.

[92] Tsutsumi N, Okumachi K, Kinashi K, Sakai W. Re-evaluation of the origin of relaxor ferroelectricity in vinylidene fluoride terpolymers: An approach using switching current measurements. Sci Rep 2017;7:15871.

[93] Chen X, Qin H, Zhu W, Zhang B, Lu W, Bernholc J, et al. Giant Electrostriction Enabled by Defect-Induced Critical Phenomena in Relaxor Ferroelectric Polymers. Macromolecules 2023.

[94] Yang L, Li X, Allahyarov E, Taylor PL, Zhang QM, Zhu L. Novel polymer ferroelectric behavior via crystal isomorphism and the nanoconfinement effect. Polymer 2013;54:1709–28.

[95] Zhu L, Wang Q. Novel Ferroelectric Polymers for High Energy Density and Low Loss Dielectrics. Macromolecules 2012;45:2937–54.

[96] Liu Y, Zhang B, Xu W, Haibibu A, Han Z, Lu W, et al. Chirality-induced relaxor properties in ferroelectric polymers. Nat Mater 2020;19:1169–74.

[97] Chen X, Qin H, Qian X, Zhu W, Li B, Zhang B, et al. Relaxor ferroelectric polymer exhibits ultrahigh electromechanical coupling at low electric field. Science 2022;375:1418–22.

[98] Tu NDK, Park J, Na S, Kim KM, Kwon T-H, Ko H, et al. Co-solvent induced piezoelectric γ-phase nylon-11 separator for sodium metal battery. Nano Energy 2020;70:104501.

[99] Hattori T, Takahashi Y, Iijima M, Fukada E. Piezoelectric and ferroelectric properties of polyurea-5 thin films prepared by vapor deposition polymerization. J Appl Phys 1996;79:1713–21.

[100] Takahashi Y, Ukishima S, Iijima M, Fukada E. Piezoelectric properties of thin films of aromatic polyurea prepared by vapor deposition polymerization. J Appl Phys 1991;70:6983–7.

[101] Ounaies Z, Young JA, Harrison JS. An Overview of the Piezoelectric Phenomenon in Amorphous Polymers. Field Responsive Polymers: American Chemical Society; 1999. p. 88–103.

[102] Fukada E. Recent developments of piezoelectric polymers - polyurea, odd-nylon, vinylidenecyanide copolymer, and polylactic acid. 2005 12th International Symposium on Electrets2005. p. 106-12.

[103] Tasaka S, Takatoshi Toyama TT, Norihiro Inagaki NI. Ferro- and Pyroelectricity in Amorphous Polyphenylethernitrile. Jpn J Appl Phys 1994;33:5838.

[104] Park C, Ounaies Z, Wise KE, Harrison JS. In situ poling and imidization of amorphous piezoelectric polyimides. Polymer 2004;45:5417–25.

[105] Yang L, Qiu T, Shen M, He H, Huang H. Metal-organic frameworks $Co_3[Co(CN)_6]_2$: A promising candidate for dramatically reinforcing the piezoelectric activity of PVDF. Compos Sci Technol 2020;196:108232.

[106] Tian W, Qiu J, Li N, Chen D, Xu Q, Li H, et al. Efficient piezocatalytic removal of BPA and Cr(VI) with SnS$_2$/CNFs membrane by harvesting vibration energy. Nano Energy 2021;86:106036.

[107] Shi J, Zeng W, Dai Z, Wang L, Wang Q, Lin S, et al. Piezocatalytic Foam for Highly Efficient Degradation of Aqueous Organics. Small Science 2021;1:2000011.

[108] Wei Y, Zhang Y, Geng W, Su H, Long M. Efficient bifunctional piezocatalysis of Au/BiVO$_4$ for simultaneous removal of 4-chlorophenol and Cr(VI) in water. Appl Catal B 2019;259:118084.

[109] Wang P, Li X, Fan S, Chen X, Qin M, Long D, et al. Impact of oxygen vacancy occupancy on piezo-catalytic activity of BaTiO$_3$ nanobelt. Appl Catal B 2020;279:119340.

[110] Wang Y, Wen X, Jia Y, Huang M, Wang F, Zhang X, et al. Piezo-catalysis for nondestructive tooth whitening. Nat Commun 2020;11:1328.

[111] You H, Wu Z, Zhang L, Ying Y, Liu Y, Fei L, et al. Harvesting the Vibration Energy of BiFeO$_3$ Nanosheets for Hydrogen Evolution. Angew Chem Int Ed 2019;58:11779–84.

[112] Feng Y, Ling L, Wang Y, Xu Z, Cao F, Li H, et al. Engineering spherical lead zirconate titanate to explore the essence of piezo-catalysis. Nano Energy 2017;40:481–6.

[113] Chen X, Liu L, Feng Y, Wang L, Bian Z, Li H, et al. Fluid eddy induced piezo-promoted photodegradation of organic dye pollutants in wastewater on ZnO nanorod arrays/3D Ni foam. Mater Today 2017;20:501–6.

[114] Xue X, Zang W, Deng P, Wang Q, Xing L, Zhang Y, et al. Piezo-potential enhanced photocatalytic degradation of organic dye using ZnO nanowires. Nano Energy 2015;13:414–22.

[115] Starr MB, Shi J, Wang X. Piezopotential-Driven Redox Reactions at the Surface of Piezoelectric Materials. Angew Chem Int Ed 2012;51:5962–6.

[116] Mezyk SP, Rickman KA, Hirsch CM, Dail MK, Scheeler J, Foust T. 9 - Advanced Oxidation and Reduction Process Radical Generation in the Laboratory and on a Large Scale: An Overview. In: Ahuja S, editor. Monitoring Water Quality. Amsterdam: Elsevier; 2013. p. 227–48.

[117] Chauhan R, Dinesh GK, Alawa B, Chakma S. A critical analysis of sono-hybrid advanced oxidation process of ferrioxalate system for degradation of recalcitrant pollutants. Chemosphere 2021;277:130324.

[118] Qiu P, Park B, Choi J, Thokchom B, Pandit AB, Khim J. A review on heterogeneous sonocatalyst for treatment of organic pollutants in aqueous phase based on catalytic mechanism. Ultrason Sonochem 2018;45:29–49.

[119] Lan S, Yu C, Wu E, Zhu M, Dionysiou DD. Self-Powered Water Flow-Triggered Piezocatalytic Generation of Reactive Oxygen Species for Water Purification in Simulated Water Drainage. ACS ES&T Engineering 2022;2:101–9.

[120] Wang J, Liang Y, Wang Z, Huo B, Liu C, Chen X, et al. High efficiently degradation of organic pollutants via low-speed water flow activation of Cu$_2$O@MoS$_2$/PVDF modified pipeline with piezocatalysis performance. Chem Eng J 2023;458:141409.

[121] Wu J, Xu Q, Lin E, Yuan B, Qin N, Thatikonda SK, et al. Insights into the Role of Ferroelectric Polarization in Piezocatalysis of Nanocrystalline BaTiO$_3$. ACS Appl Mater Interfaces 2018;10:17842–9.

[122] Feng W, Yuan J, Gao F, Weng B, Hu W, Lei Y, et al. Piezopotential-driven simulated electrocatalytic nanosystem of ultrasmall MoC quantum dots encapsulated in ultrathin N-doped graphene vesicles for superhigh H$_2$ production from pure water. Nano Energy 2020;75:104990.

[123] Liu N, Wang R, Gao S, Zhang R, Fan F, Ma Y, et al. High-Performance Piezo-Electrocatalytic Sensing of Ascorbic Acid with Nanostructured Wurtzite Zinc Oxide. Adv Mater 2021;33:2105697.

[124] Li P, Wu J, Wu Z, Jia Y, Ma J, Chen W, et al. Strong tribocatalytic dye decomposition through utilizing triboelectric energy of barium strontium titanate nanoparticles. Nano Energy 2019;63:103832.

[125] Tang Q, Zhu M, Zhang H, Gao J, Kwok KW, Kong L-B, et al. Enhanced tribocatalytic degradation of dye pollutants through governing the charge accumulations on the surface of ferroelectric barium zirconium titanate particles. Nano Energy 2022;100:107519.

[126] Min M, Liu Y, Song C, Zhao D, Wang X, Qiao Y, et al. Photothermally Enabled Pyro-Catalysis of a BaTiO$_3$ Nanoparticle Composite Membrane at the Liquid/Air Interface. ACS Appl Mater Interfaces 2018;10:21246–53.

[127] Li X, Tong W, Shi J, Chen Y, Zhang Y, An Q. Tribocatalysis mechanisms: electron transfer and transition. J Mater Chem A 2023;11:4458–72.

[128] You H, Ma X, Wu Z, Fei L, Chen X, Yang J, et al. Piezoelectrically/pyroelectrically-driven vibration/cold-hot energy harvesting for mechano-/pyro- bi-catalytic dye decomposition of NaNbO$_3$ nanofibers. Nano Energy 2018;52:351–9.

[129] Zhang Y, Liu Y, Wang ZL. Fundamental Theory of Piezotronics. Adv Mater 2011;23:3004–13.

[130] Su R, Hsain HA, Wu M, Zhang D, Hu X, Wang Z, et al. Nano-Ferroelectric for High Efficiency Overall Water Splitting under Ultrasonic Vibration. Angew Chem Int Ed 2019;58:15076–81.

[131] Su R, Wang Z, Zhu L, Pan Y, Zhang D, Wen H, et al. Strain-Engineered Nano-Ferroelectrics for High-Efficiency Piezocatalytic Overall Water Splitting. Angew Chem Int Ed 2021;60:16019–26.

[132] Starr MB, Wang X. Fundamental Analysis of Piezocatalysis Process on the Surfaces of Strained Piezoelectric Materials. Sci Rep 2013;3:2160.

[133] Zhou Z, Zhan C, Kan E. Understanding the piezocatalytic properties of the BaTiO$_3$(001) surface via density functional theory. PCCP 2023;25:8631–40.

[134] Ai J-D, Jin C-C, Liu D-M, Zhang J-T, Zhang L-X. Strain Engineering to Boost Piezocatalytic Activity of BaTiO$_3$. ChemCatChem 2023;15:e202201316.

[135] Fu H, Cohen RE. Polarization rotation mechanism for ultrahigh electromechanical response in single-crystal piezoelectrics. Nature 2000;403:281–3.

[136] Huang Y-L, Nikonov D, Addiego C, Chopdekar RV, Prasad B, Zhang L, et al. Manipulating magnetoelectric energy landscape in multiferroics. Nat Commun 2020;11:2836.

[137] Zhao Q, Xiao H, Huangfu G, Zheng Z, Wang J, Wang F, et al. Highly-efficient piezocatalytic performance of nanocrystalline BaTi$_{0.89}$Sn$_{0.11}$O$_3$ catalyst with Tc near room temperature. Nano Energy 2021;85:106028.

[138] Gao J, Xue D, Wang Y, Wang D, Zhang L, Wu H, et al. Microstructure basis for strong piezoelectricity in Pb-free Ba(Zr$_{0.2}$Ti$_{0.8}$)O$_3$-(Ba$_{0.7}$Ca$_{0.3}$)TiO$_3$ ceramics. Appl Phys Lett 2011;99:092901.

[139] Rossetti GA, Khachaturyan AG, Akcay G, Ni Y. Ferroelectric solid solutions with morphotropic boundaries: Vanishing polarization anisotropy, adaptive, polar glass, and two-phase states. J Appl Phys 2008;103:114113.

[140] Wang K, Zhang M, Li D, Liu L, Shao Z, Li X, et al. Ternary BaCaZrTi perovskite oxide piezocatalysts dancing for efficient hydrogen peroxide generation. Nano Energy 2022;98:107251.

[141] Wada S, Suzuki S, Noma T, Suzuki T, Osada M, Kakihana M, et al. Enhanced Piezoelectric Property of Barium Titanate Single Crystals with Engineered Domain Configurations. Jpn J Appl Phys 1999;38:5505.

[142] Liu X, Tan X. Giant Strains in Non-Textured (Bi$_{1/2}$Na$_{1/2}$)TiO$_3$-Based Lead-Free Ceramics. Adv Mater 2016;28:574–8.

[143] Zuo R, Fu J, Yin GZ, Li XL, Jiang JZ. Electric field induced phase instability in typical (Na, K)(Nb, Sb)O3-LiTaO3 ceramics near orthorhombic and tetragonal phase boundary. Appl Phys Lett 2012;101:092906.

[144] Shi L, Lu C, Chen L, Zhang Q, Li Y, Zhang T, et al. Piezocatalytic performance of Na$_{0.5}$Bi$_{0.5}$TiO$_3$ nanoparticles for degradation of organic pollutants. J Alloy Compd 2022;895:162591.

[145] Zhu R, Xu Y, Bai Q, Wang Z, Guo X, Kimura H. Direct degradation of dyes by piezoelectric fibers through scavenging low frequency vibration. Chem Phys Lett 2018;702:26–31.

[146] Yu C, Tan M, Li Y, Liu C, Yin R, Meng H, et al. Ultrahigh piezocatalytic capability in eco-friendly BaTiO$_3$ nanosheets promoted by 2D morphology engineering. J Colloid Interface Sci 2021;596:288–96.

[147] Cheng T, Gao W, Gao H, Wang S, Yi Z, Wang X, et al. Piezocatalytic degradation of methylene blue, tetrabromobisphenol A and tetracycline hydrochloride using Bi$_4$Ti$_3$O$_{12}$ with different morphologies. Mater Res Bull 2021;141:111350.

[148] Tang Q, Wu J, Kim D, Franco C, Terzopoulou A, Veciana A, et al. Enhanced Piezocatalytic Performance of BaTiO3 Nanosheets with Highly Exposed 001 Facets. Adv Funct Mater 2022;32:2202180.

[149] Zhao Y, Zhao Y, Shi R, Wang B, Waterhouse GIN, Wu L-Z, et al. Tuning Oxygen Vacancies in Ultrathin TiO$_2$ Nanosheets to Boost Photocatalytic Nitrogen Fixation up to 700 nm. Adv Mater 2019;31:1806482.

[150] Lei J, Wang C, Feng X, Ma L, Liu X, Luo Y, et al. Sulfur-regulated defect engineering for enhanced ultrasonic piezocatalytic therapy of bacteria-infected bone defects. Chem Eng J 2022;435:134624.

[151] Li H, Li J, Ai Z, Jia F, Zhang L. Oxygen Vacancy-Mediated Photocatalysis of BiOCl: Reactivity, Selectivity, and Perspectives. Angew Chem Int Ed 2018;57: 122–38.

[152] Zhang L, Shen Q, Zhan R, Zheng S, Sheng J, Yang H. Oxygen-vacancy-mediated photocatalytic degradation of tetracycline under weak visible-light irradiation over hierarchical $Bi_2MoO_6@Bi_2O_3$ core–shell fibers. Cat Sci Technol 2022;12:1685–96.

[153] Liu D-M, Zhang J-T, Jin C-C, Chen B-B, Hu J, Zhu R, et al. Insight into oxygen-vacancy regulation on piezocatalytic activity of $(Bi_{1/2}Na_{1/2})TiO_3$ crystallites: Experiments and first-principles calculations. Nano Energy 2022;95:106975.

[154] Zheng Y, Wu X, Zhang Y, Li Y, Shao W, Fu J, et al. Highly efficient harvesting of vibration energy for complex wastewater purification using $Bi_5Ti_3FeO_{15}$ with controlled oxygen vacancies. Chem Eng J 2023;453:139919.

[155] Wang C, Chen F, Hu C, Ma T, Zhang Y, Huang H. Efficient piezocatalytic H2O2 production of atomic-level thickness $Bi_4Ti_3O_{12}$ nanosheets with surface oxygen vacancy. Chem Eng J 2022;431:133930.

[156] Kang Z, Lin E, Qin N, Wu J, Yuan B, Bao D. Effect of oxygen vacancies and crystal symmetry on piezocatalytic properties of Bi_2WO_6 ferroelectric nanosheets for wastewater decontamination. Environ Sci Nano 2021;8:1376–88.

[157] Miao Y, Tian W, Han J, Li N, Chen D, Xu Q, et al. Oxygen vacancy-induced hydroxyl dipole reorientation in hydroxyapatite for enhanced piezocatalytic activity. Nano Energy 2022;100:107473.

[158] Kang Z, Lin E, Qin N, Wu J, Bao D. Bismuth Vacancy-Mediated Quantum Dot Precipitation to Trigger Efficient Piezocatalytic Activity of Bi_2WO_6 Nanosheets. ACS Appl Mater Interfaces 2022;14:11375–87.

[159] Walker J, Simons H, Alikin DO, Turygin AP, Shur VY, Kholkin AL, et al. Dual strain mechanisms in a lead-free morphotropic phase boundary ferroelectric. Sci Rep 2016;6:19630.

[160] Orudzhev FF, Alikhanov NM, Ramazanov SM, Sobola DS, Murtazali RK, Ismailov EH, et al. Morphotropic Phase Boundary Enhanced Photocatalysis in Sm Doped BiFeO(3). Molecules (Basel, Switzerland). 2022;27.

[161] Mandal P, Manjón-Sanz A, Corkett AJ, Comyn TP, Dawson K, Stevenson T, et al. Morphotropic Phase Boundary in the Pb-Free $(1–x)BiTi_{3/8}Fe_{2/8}Mg_{3/8}O_3–xCaTiO_3$ System: Tetragonal Polarization and Enhanced Electromechanical Properties. Adv Mater 2015;27:2883–9.

[162] Sun X-x, Li R, Yang Z, Zhang N, Wu C, Li J, et al. Modulating polarization rotation to stimulate the high piezocatalytic activity of (K, Na)NbO₃ lead-free piezoelectric materials. Appl Catal B 2022.

[163] Maria Joseph Raj NP, Alluri NR, Khandelwal G, Kim S-J. The morphotropic phase boundary based BCST ferroelectric system for water remediation through Bi-catalytic activity. J Alloy Compd 2021.

[164] Zhang A, Liu Z, Xie B, Lu J, Guo K, Ke S, et al. Vibration catalysis of eco-friendly $Na_{0.5}K_{0.5}NbO_3$-based piezoelectric: An efficient phase boundary catalyst. Appl Catal B 2020.

[165] Zhu M, Li S, Zhang H, Gao J, Kwok KW, Jia Y, et al. Diffused phase transition boosted dye degradation with Ba $(Zr_xTi_{1−x})O_3$ solid solutions through piezoelectric effect. Nano Energy 2021;89:106474.

[166] Zhang Y, Phuong PTT, Roake E, Khanbareh H, Wang Y, Dunn S, et al. Thermal Energy Harvesting Using Pyroelectric-Electrochemical Coupling in Ferroelectric Materials. Joule 2020;4:301–9.

[167] Zhang Y, Thuy Phuong PT, Hoang Duy NP, Roake E, Khanbareh H, Hopkins M, et al. Polarisation tuneable piezo-catalytic activity of Nb-doped PZT with low Curie temperature for efficient CO₂ reduction and H₂ generation. Nanoscale Advances 2021;3:1362–74.

[168] Thuy Phuong PT, Zhang Y, Gathercole N, Khanbareh H, Hoang Duy NP, Zhou X, et al. Demonstration of Enhanced Piezo-Catalysis for Hydrogen Generation and Water Treatment at the Ferroelectric Curie Temperature. iScience. 2020;23:101095.

[169] Zhou X, Shen B, Lyubartsev A, Zhai J, Hedin N. Semiconducting piezoelectric heterostructures for piezo- and piezophotocatalysis. Nano Energy 2022;96: 107141.

[170] Cheng Y, Chen J, Wang P, Liu W, Che H, Gao X, et al. Interfacial engineering boosting the piezocatalytic performance of Z-scheme heterojunction for carbamazepine degradation: Mechanism, degradation pathway and DFT calculation. Appl Catal B 2022;317:121793.

[171] Dai J, Shao N, Zhang S, Zhao Z, Long Y, Zhao S, et al. Enhanced Piezocatalytic Activity of $Sr_{0.5}Ba_{0.5}Nb_2O_6$ Nanostructures by Engineering Surface Oxygen Vacancies and Self-Generated Heterojunctions. ACS Appl Mater Interfaces 2021;13:7259–67.

[172] Yang G, Chen Q, Wang W, Wu S, Gao B, Xu Y, et al. Cocatalyst Engineering in Piezocatalysis: A Promising Strategy for Boosting Hydrogen Evolution. ACS Appl Mater Interfaces 2021;13:15305–14.

[173] Xu W, Li K, Shen L, Liu X, Chen Y, Feng J, et al. Piezodeposition of Metal Cocatalysts for Promoted Piezocatalytic Generation of Reactive Oxygen Species and Hydrogen in Water. ChemCatChem 2022;14:e202200312.

[174] Singh G, Sharma M, Vaish R. Flexible Ag@LiNbO₃/PVDF Composite Film for Piezocatalytic Dye/Pharmaceutical Degradation and Bacterial Disinfection. ACS Appl Mater Interfaces 2021;13:22914–25.

[175] Bagchi B, Hoque NA, Janowicz N, Das S, Tiwari MK. Re-usable self-poled piezoelectric/piezocatalytic films with exceptional energy harvesting and water remediation capability. Nano Energy 2020;78:105339.

[176] Qian W, Zhao K, Zhang D, Bowen CR, Wang Y, Yang Y. Piezoelectric Material-Polymer Composite Porous Foam for Efficient Dye Degradation via the Piezo-Catalytic Effect. ACS Appl Mater Interfaces 2019;11:27862–9.

[177] Demirbas A. Agricultural based activated carbons for the removal of dyes from aqueous solutions: A review. J Hazard Mater 2009;167:1–9.

[178] Wardman P. Reduction Potentials of One-Electron Couples Involving Free Radicals in Aqueous Solution. J Phys Chem Ref Data 1989;18:1637–755.

[179] Bard AJ, Parsons R, Jordan J. Standard potentials in aqueous solution /. New York: M. Dekker; 1985.

[180] Liu DM, Jin CC, Shan FK, He JJ, Wang F. Synthesizing BaTiO₃ Nanostructures to Explore Morphological Influence, Kinetics, and Mechanism of Piezocatalytic Dye Degradation. ACS Appl Mater Interfaces 2020;12:17443–51.

[181] Bossl F, Tudela I. Piezocatalysis: Can catalysts really dance? Curr Opin Green Sustain Chem 2021;32:8.

[182] Yuan BW, Wu J, Qin N, Lin EZ, Bao DH. Enhanced Piezocatalytic Performance of (Ba, Sr)TiO3 Nanowires to Degrade Organic Pollutants. ACS Appl Nano Mater 2018;1:5119–27.

[183] Yein WT, Wang Q, Li Y, Wu XH. Piezoelectric potential induced the improved micro-pollutant dye degradation of Co doped MoS2 ultrathin nanosheets in dark. Catal Commun 2019;125:61–5.

[184] Wang SS, Wu Z, Chen J, Ma JP, Ying JS, Cui SC, et al. Lead-free sodium niobate nanowires with strong piezo-catalysis for dye wastewater degradation. Ceram Int 2019;45:11703–8.

[185] Biswas A, Saha S, Jana NR. ZnSnO3 Nanoparticle-Based Piezocatalysts for Ultrasound-Assisted Degradation of Organic Pollutants. ACS Appl Nano Mater 2019; 2:1120–8.

[186] Ning XE, Hao AZ, Cao YL, Hu JD, Xie J, Jia DZ. Effective promoting piezocatalytic property of zinc oxide for degradation of organic pollutants and insight into piezocatalytic mechanism. J Colloid Interface Sci 2020;577:290–9.

[187] Li ZY, Zhang QL, Wang LK, Yang JY, Wu Y, He YM. Novel application of Ag/PbBiO2I nanocomposite in piezocatalytic degradation of rhodamine B via harvesting ultrasonic vibration energy. Ultrason Sonochem 2021;78:5.

[188] Zheng S, Li XJ, Zhang JY, Wang JF, Zhao CR, Hu X, et al. One-step preparation of MoOX/ZnS/ZnO composite and its excellent performance in piezocatalytic degradation of Rhodamine B under ultrasonic vibration. J Environ Sci 2023;125:1–13.

[189] Meng F, Ma W, Wang Y, Zhu Z, Chen Z, Lu G. A tribo-positive Fe@MoS₂ piezocatalyst for the durable degradation of tetracycline: degradation mechanism and toxicity assessment. Environ Sci Nano 2020;7:1704–18.

[190] Feng J, Sun L, Liu X, Zhu J, Tian S, Wu R, et al. Coupling effect of piezomaterial and DSA catalyst for degradation of metronidazole: Finding of induction electrocatalysis from remnant piezoelectric filed. J Catal 2020;381:530–9.

[191] Huo B, Meng F, Yang J, Wang Y, Qi J, Ma W, et al. High efficiently piezocatalysis degradation of tetracycline by few-layered MoS$_2$/GDY: Mechanism and toxicity evaluation. Chem Eng J 2022;436:135173.

[192] Koppenol WH. The centennial of the Fenton reaction. Free Radic Biol Med 1993;15:645–51.

[193] Eisenhauer HR. Oxidation of Phenolic Wastes. Journal (Water Pollution Control Federation) 1964;36:1116–28.

[194] Yu Y, Lu L, Yang Q, Zupanic A, Xu Q, Jiang L. Using MoS$_2$ Nanomaterials to Generate or Remove Reactive Oxygen Species: A Review. ACS Applied Nano Materials 2021;4:7523–37.

[195] Lv W, Kong L, Lan S, Feng J, Xiong Y, Tian S. Enhancement effect in the piezoelectric degradation of organic pollutants by piezo-Fenton process. J Chem Technol Biotechnol 2017;92:152–6.

[196] Wei Y, Zhang Y, Miao J, Geng W, Long M. In-situ utilization of piezo-generated hydrogen peroxide for efficient p-chlorophenol degradation by Fe loading bismuth vanadate. Appl Surf Sci 2021;543:148791.

[197] Chai M, Tong W, Wang Z, Chen Z, An Y, Zhang Y. Piezoelectric-Fenton degradation and mechanism study of Fe$_2$O$_3$/PVDF-HFP porous film drove by flowing water. J Hazard Mater 2022;430:128446.

[198] Lan S, Jing B, Yu C, Yan D, Li Z, Ao Z, et al. Protrudent Iron Single-Atom Accelerated Interfacial Piezoelectric Polarization for Self-Powered Water Motion Triggered Fenton-Like Reaction. Small 2022;18:2105279.

[199] Ranjan A, Hsiao K-Y, Lin C-Y, Tseng Y-H, Lu M-Y. Enhanced Piezocatalytic Activity in Bi$_{1/2}$Na$_{1/2}$TiO$_3$ for Water Splitting by Oxygen Vacancy Engineering. ACS Appl Mater Interfaces 2022;14:35635–44.

[200] Hong K-S, Xu H, Konishi H, Li X. Direct Water Splitting Through Vibrating Piezoelectric Microfibers in Water. J Phys Chem Lett 2010;1:997–1002.

[201] Li Y, Li L, Liu F, Wang B, Gao F, Liu C, et al. Robust route to H$_2$O$_2$ and H$_2$ via intermediate water splitting enabled by capitalizing on minimum vanadium-doped piezocatalysts. Nano Res 2022;15:7986–93.

[202] He J, Gao F, Wang H, Liu F, Lin J, Wang B, et al. C-Doped KNbO$_3$ single crystals for enhanced piezocatalytic intermediate water splitting. Environ Sci Nano 2022;9:1952–60.

[203] Zhang Y, Khanbareh H, Dunn S, Bowen CR, Gong H, Duy NPH, et al. High Efficiency Water Splitting using Ultrasound Coupled to a BaTiO$_3$ Nanofluid. Adv Sci 2022;9:2105248.

[204] Su Y, Zhang L, Wang W, Li X, Zhang Y, Shao D. Enhanced H$_2$ evolution based on ultrasound-assisted piezo-catalysis of modified MoS2. J Mater Chem A 2018;6:11909–15.

[205] Xu X, Xiao L, Wu Z, Jia Y, Ye X, Wang F, et al. Harvesting vibration energy to piezo-catalytically generate hydrogen through Bi$_2$WO$_6$ layered-perovskite. Nano Energy 2020;78:105351.

[206] Sun Y, Li X, Vijayakumar A, Liu H, Wang C, Zhang S, et al. Hydrogen Generation and Degradation of Organic Dyes by New Piezocatalytic 0.7BiFeO$_3$–0.3BaTiO$_3$ Nanoparticles with Proper Band Alignment. ACS Appl Mater Interfaces 2021;13:11050–7.

[207] Ma X, Gao Y, Yang B, Lou X, Huang J, Ma L, et al. Enhanced charge separation in La$_2$NiO$_4$ nanoplates by coupled piezocatalysis and photocatalysis for efficient H$_2$ evolution. Nanoscale 2022;14:7083–95.

[208] Das S, Pérez-Ramírez J, Gong J, Dewangan N, Hidajat K, Gates BC, et al. Core–shell structured catalysts for thermocatalytic, photocatalytic, and electrocatalytic conversion of CO$_2$. Chem Soc Rev 2020;49:2937–3004.

[209] Nitopi S, Bertheussen E, Scott SB, Liu X, Engstfeld AK, Horch S, et al. Progress and Perspectives of Electrochemical CO$_2$ Reduction on Copper in Aqueous Electrolyte. Chem Rev 2019;119:7610–72.

[210] Phuong PTT, Vo D-V-N, Duy NPH, Pearce H, Tsikriteas ZM, Roake E, et al. Piezoelectric catalysis for efficient reduction of CO$_2$ using lead-free ferroelectric particulates. Nano Energy 2022;95:107032.

[211] Ren Z, Chen F, Zhao Q, Zhao G, Li H, Sun W, et al. Efficient CO$_2$ reduction to reveal the piezocatalytic mechanism: From displacement current to active sites. Appl Catal B 2023;320:122007.

[212] Zhou Y, Wang H, Liu X, Qiao S, Shao D, Zhou J, et al. Direct piezocatalytic conversion of methane into alcohols over hydroxyapatite. Nano Energy 2021;79:105449.

[213] Nosaka Y, Nosaka AY. Generation and Detection of Reactive Oxygen Species in Photocatalysis. Chem Rev 2017;117:11302–36.

[214] Sena Laura A, Chandel NS. Physiological Roles of Mitochondrial Reactive Oxygen Species. Mol Cell 2012;48:158–67.

[215] Forman HJ, Maiorino M, Ursini F. Signaling Functions of Reactive Oxygen Species. Biochemistry 2010;49:835–42.

[216] Nathan C, Cunningham-Bussel A. Beyond oxidative stress: an immunologist's guide to reactive oxygen species. Nat Rev Immunol 2013;13:349–61.

[217] Panieri E, Santoro MM. ROS homeostasis and metabolism: a dangerous liason in cancer cells. Cell Death Dis 2016;7:e2253 -e.

[218] Matés JM, Sánchez-Jiménez FM. Role of reactive oxygen species in apoptosis: implications for cancer therapy. Int J Biochem Cell Biol 2000;32:157–70.

[219] Yang B, Chen Y, Shi J. Reactive Oxygen Species (ROS)-Based Nanomedicine. Chem Rev 2019;119:4881–985.

[220] Dolmans DEJGJ, Fukumura D, Jain RK. Photodynamic therapy for cancer. Nat Rev Cancer 2003;3:380–7.

[221] Gu T, Wang Y, Lu Y, Cheng L, Feng L, Zhang H, et al. Platinum Nanoparticles to Enable Electrodynamic Therapy for Effective Cancer Treatment. Adv Mater 2019;31:1806803.

[222] Lu K, He C, Guo N, Chan C, Ni K, Lan G, et al. Low-dose X-ray radiotherapy–radiodynamic therapy via nanoscale metal–organic frameworks enhances checkpoint blockade immunotherapy. Nat Biomed Eng 2018;2:600–10.

[223] Qian X, Zheng Y, Chen Y. Micro/Nanoparticle-Augmented Sonodynamic Therapy (SDT): Breaking the Depth Shallow of Photoactivation. Adv Mater 2016;28:8097–129.

[224] Zhang C, Bu W, Ni D, Zhang S, Li Q, Yao Z, et al. Synthesis of Iron Nanometallic Glasses and Their Application in Cancer Therapy by a Localized Fenton Reaction. Angew Chem Int Ed 2016;55:2101–6.

[225] Rosenthal I, Sostaric JZ, Riesz P. Sonodynamic therapy—a review of the synergistic effects of drugs and ultrasound. Ultrason Sonochem 2004;11:349–63.

[226] Canavese G, Ancona A, Racca L, Canta M, Dumontel B, Barbaresco F, et al. Nanoparticle-assisted ultrasound: A special focus on sonodynamic therapy against cancer. Chem Eng J 2018;340:155–72.

[227] Zhu P, Chen Y, Shi J. Piezocatalytic Tumor Therapy by Ultrasound-Triggered and BaTiO$_3$-Mediated Piezoelectricity. Adv Mater 2020;32:2001976.

[228] Li Z, Zhang T, Fan F, Gao F, Ji H, Yang L. Piezoelectric Materials as Sonodynamic Sensitizers to Safely Ablate Tumors: A Case Study Using Black Phosphorus. J Phys Chem Lett 2020;11:1228–38.

[229] Ma K, Qi G, Wang B, Yu T, Zhang Y, Li H, et al. Ultrasound-activated Au/ZnO-based Trojan nanogenerators for combined targeted electro-stimulation and enhanced catalytic therapy of tumor. Nano Energy 2021;87:106208.

[230] Zhao P, Jiang Y, Tang Z, Li Y, Sun B, Wu Y, et al. Constructing Electron Levers in Perovskite Nanocrystals to Regulate the Local Electron Density for Intensive Chemodynamic Therapy. Angew Chem Int Ed 2021;60:8905–12.

[231] Wang M, Wang B, Huang F, Lin Z. Enabling PIEZOpotential in PIEZOelectric Semiconductors for Enhanced Catalytic Activities. Angew Chem Int Ed 2019;58:7526–36.

[232] Wang J, Sui L, Huang J, Miao L, Nie Y, Wang K, et al. MoS2-based nanocomposites for cancer diagnosis and therapy. Bioact Mater 2021;6:4209–42.

[233] Zhou X, Shen B, Zhai J, Hedin N. Reactive Oxygenated Species Generated on Iodide-Doped BiVO4/BaTiO3 Heterostructures with Ag/Cu Nanoparticles by Coupled Piezophototronic Effect and Plasmonic Excitation. Adv Funct Mater 2021;31:2009594.

[234] Wang S, Chen C, Wang J, Li C-B-W, Zhou J, Liu Y-X, et al. Synergetic Chemo-Piezodynamic Therapy of Osteosarcoma Enabled by Defect-Driven Lead-Free Piezoelectrics. Adv Funct Mater 2022;32:2208128.

[235] Babuponnusami A, Muthukumar K. A review on Fenton and improvements to the Fenton process for wastewater treatment. J Environ Chem Eng 2014;2:557–72.

[236] Tang Z, Liu Y, He M, Bu W. Chemodynamic Therapy: Tumour Microenvironment-Mediated Fenton and Fenton-like Reactions. Angew Chem Int Ed 2019;58:946–56.

[237] Dong Y, Dong S, Liu B, Yu C, Liu J, Yang D, et al. 2D Piezoelectric Bi_2MoO_6 Nanoribbons for GSH-Enhanced Sonodynamic Therapy. Adv Mater 2021;33: 2106838.

[238] Xu Q, Gao X, Wen M, Liu Y, Li Y, Wei C, et al. Biocomputation with $MnTiO_3$ Piezoelectric Enzymes for Programed Catalysis of Tumor Death. ACS Appl Mater Interfaces 2022;14:28199–210.

[239] Macfarlane GT, Macfarlane S. Bacteria, Colonic Fermentation, and Gastrointestinal Health. J AOAC Int 2012;95:50–60.

[240] Macpherson AJ, Harris NL. Interactions between commensal intestinal bacteria and the immune system. Nat Rev Immunol 2004;4:478–85.

[241] Cunha BA. Antibiotic Side Effects. Med Clin N Am 2001;85:149–85.

[242] Aslam B, Wang W, Arshad MI, Khurshid M, Muzammil S, Rasool MH, et al. Antibiotic resistance: a rundown of a global crisis. Infection Drug Resistance 2018; 11:1645–58.

[243] Fang FC. Antimicrobial reactive oxygen and nitrogen species: concepts and controversies. Nat Rev Microbiol 2004;2:820–32.

[244] Wu M, Zhang Z, Liu Z, Zhang J, Zhang Y, Ding Y, et al. Piezoelectric nanocomposites for sonodynamic bacterial elimination and wound healing. Nano Today 2021;37:101104.

[245] Liu X, Shen L, Xu W, Kang W, Yang D, Li J, et al. Low frequency hydromechanics-driven generation of superoxide radicals via optimized piezotronic effect for water disinfection. Nano Energy 2021;88:106290.

[246] Scheltens P, Blennow K, Breteler MMB, de Strooper B, Frisoni GB, Salloway S, et al. Alzheimer's disease. Lancet 2016;388:505–17.

[247] Reinke AA, Gestwicki JE. Structure–activity Relationships of Amyloid Beta-aggregation Inhibitors Based on Curcumin: Influence of Linker Length and Flexibility. Chem Biol Drug Des 2007;70:206–15.

[248] Finder VH, Glockshuber R. Amyloid-β Aggregation. Neurodegener Dis 2007;4:13–27.

[249] Son G, Lee BI, Chung YJ, Park CB. Light-triggered dissociation of self-assembled β-amyloid aggregates into small, nontoxic fragments by ruthenium (II) complex. Acta Biomater 2018;67:147–55.

[250] Jang J, Kim K, Yoon J, Park CB. Piezoelectric materials for ultrasound-driven dissociation of Alzheimer's β-amyloid aggregate structure. Biomaterials 2020; 255:120165.

[251] Gomes C, Silva AC, Marques AC, Sousa Lobo J, Amaral MH. Biotechnology Applied to Cosmetics and Aesthetic Medicines. Cosmetics 2020.

[252] Kebaili I, Elsaeedy HI, Boukhris I, Farhat LB, Ahmed SB, Alrowaili ZA, et al. Poling direction-driven tuning of piezoelectric properties of ferroelectric materials: an experimental study. J Aust Ceram Soc 2022;58:1111–5.